DESIGN AND IMPLEMENTATION OF ESTIMATORS AND CONTROLLERS FOR A DFIG-BASED WIND ENERGY CONVERSION SYSTEMS

A Thesis

Submitted in Partial Fulfillment of the Requirement

for the Award of the degree of

Doctor of Philosophy

By

Prosenjit Mondal

School of Energy Science and Engineering
Indian Institute of Technology Guwahati
Guwahati - 781039, Assam, India
January 2021

Dedicated to

Almighty

for everything

&

My dear parents and wife

Sulekha Mondal, Shyamal Mondal and Sangeeta Bhanja Chaudhuri

for their love and support

&

My close relatives

for their love and support

Certificate

This is to certify that the thesis entitled "**Design and Implementation of Estimators and Controllers for a DFIG-based Wind Energy Conversion Systems**", submitted by **Prosenjit Mondal** (registration no.-136151001), a research scholar in the *School of Energy Science and Engineering, Indian Institute of Technology Guwahati*, for the award of the degree of **Doctor of Philosophy**, is a record of an original research work carried out by him under my supervision and guidance. The thesis has fulfilled all requirements as per the regulations of the institute and in my opinion has reached the standard needed for submission. The results embodied in this thesis have not been submitted to any other University or Institute for the award of any degree or diploma.

Dated:
Guwahati.

Dr. Praveen Tripathy
Associate Professor
Dept. of Electronics and Electrical Engg.
Indian Institute of Technology Guwahati
Guwahati - 781 039, Assam, India.

Dated:
Guwahati.

Dr. Ujjwal K. Saha
Professor
Dept. of Mechanical Engg.
Indian Institute of Technology Guwahati
Guwahati - 781 039, Assam, India.

Acknowledgments

First and foremost, I feel it as a great privilege in expressing my deepest and most sincere gratitude to my supervisors Dr. Praveen Tripathy and Prof. Ujjwal K. Saha, for their excellent guidance throughout my study. I would particularly like to thank them for their help in patiently and carefully correcting all my manuscripts. I want to express my heartfelt thanks to Dr. Praveen Tripathy for allowing me to use the Power System Lab with all needful facilities to carry out the research work.

I am also very thankful to doctoral committee members for sparing their precious time to evaluate my work progress. I want to thank Dr. Sanjib Das (Senior Technical Officer) and Mr. Ridib Bharali (Junior Technical Superintendent) of the EEE department to help me with different essential software and necessary logistics related to my research.

My deepest thanks go to B.Tech teacher Mr. Kalyan Kumar Chakrabarty, without his guidance, I may not be here where I am today.

I want to thank my childhood friends Borun da and Tarun, B.Tech friends Supriya and Satwik and M.E junior Sapu and M.E senior Kaushik da for their constant encouragement during my studies.

My deepest gratitude goes to my parents, wife and sister for their continuous love and support throughout my studies. The opportunities they have given me and their unlimited sacrifices are the reasons where I am and what I have accomplished. My special gratitude goes to my close relatives chotto mashi and mesho, boro mesho, chhoto mama, mejo mama, boro mama, and mejo mashi, who were always there for us in our difficult times. Without them, my family and I may not have survived. My special thanks go to my brother tutu da who has always been good to me, and never judged me. In the year 2020 he passed away, I will always remember him as a good person. I am also very thankful to my father-in-law and mother-in-law for their loving support. Finally, I want to thank my sister-in-law (Laloo) and brother-in-law (Ani) for their moral support during my research work.

Prosenjit Mondal

Abstract

The world energy demand is growing steadily and to meet this growing demand, it is required to have renewable energy sources for sustainable grid or micro-grid. There are many renewable sources like the ocean wave, geothermal, biomass, solar, wind, etc. Among these, solar and wind are the most widely used renewable energy sources. They are partly fulfilling the huge energy demands of modern societies by the sustainable generation of energy. Presently, the energy generation from wind is gaining momentum worldwide due to the invention of new technologies related to the offshore wind farm installation.

Till the mid-1990s, squirrel cage induction generator (SCIG)-based fixed speed wind energy conversion systems (WECS) were the most significant contributor of renewable energy generation from wind. Presently, it is observed that most of the WECSs are variable speed constant frequency (VSCF) type, which is more efficient than the fixed speed ones. These VSCF-based WECSs convert the wind energy into electrical energy utilizing either the double-fed induction generator (DFIG) or the permanent magnet synchronous generator (PMSG). Among these, DFIG operates with a low-rated power converter (typically 30% of the DFIG rating) which makes it cost-effective and highly efficient. Further, decoupled control of active and reactive power can be achieved for DFIG-based WECS.

The effective operation of a typical doubly-fed induction generator (DFIG)-based wind energy conversion system (WECS) requires efficient control of the two power electronic converters connected back-to-back. Out of these two converters, one converter is tied to the grid or the stator of the DFIG and is called active front-end converter or grid side converter (GSC) or stator side converter (SSC), and another one is tied to the rotor of the

DFIG and is called rotor side converter (RSC). The present thesis mainly focuses on the design of controllers and observers for the DFIG.

The efficient control of the GSC depends upon the accurate information on the phase and frequency of the grid voltage, which can be estimated through a phase-lock-loop (PLL) system. Hence, a modified synchronous reference frame (SRF)-based PLL technique is proposed to estimate the phase and frequency of the grid.

The estimated phase from the proposed PLL is utilized to convert the three-phase sinusoidal variables in the stationary reference frame (abc) of the grid (voltage and current) to two-phase stationary DC variables in the synchronously rotating reference frame (dq). The dynamic model of the GSC in dq-reference frame is utilized here to develop the controllers for the GSC. Two current control algorithms are proposed to control the active and reactive grid currents of the GSC, and one voltage control algorithm is proposed to control the DC bus voltage of the GSC. One of the current controllers is based on adaptive multiple-input multiple-output (MIMO) control, and the other current controller is based on first-order sliding mode control (FOSMC). The developed voltage controller is based on an extended state observer (ESO) augmented with an adaptive control technique.

Efficient control of the RSC depends upon the accurate information on the rotor speed and rotor position/angle, which can be measured directly by a rotary encoder. However, the failure-prone nature of these encoders makes the system unreliable; hence, reliable solutions in the form of rotor speed and position observers are proposed in this thesis. Two observers are developed using the $\alpha\beta$ dynamic model of the DFIG. The stator current and rotor flux are used as the states for both the observer models. The first observer is based on the first-order sliding mode observer (FOSMO), and the second observer is based on second-order sliding mode observer (SOSMO). The performance of these observers is also validated in real-time with close loop terminal voltage control of a standalone DFIG system.

Contents

List of Acronyms

DFIG	Double Fed Induction Generator
DAC	Digital To Analog
DPC	Direct Power Control
DSP	Digital Signal Processor
DSC	Digital Signal Controller
DFT	Discrete Fourier Transform
EPLL	Enhanced Phase Lock Loop
ESO	Extended State Observer
EKF	Extended Kalman Filter
FFNS	Fundamental Frequency Negative Sequence
FFPS	Fundamental Frequency Positive Sequence
FOSMO	First Order Sliding Mode Observer
GSC	Gris Side Converter
GWEC	Global Wind Energy Council
HOSMO	Higher Order Sliding Mode Observer
IGBT	Insulated Gate Bipolar Transistor
LF	Loop Filter
LPF	Low Pass Filter
MCCF	Multiple Complex Coefficient Filter
MIMO	Multiple Input Multiple Output
MNRE	Ministry of New and Renewable Energy
MPPT	Maximum Power Point Tracking

MRAS	Model Reference Adaptive System
MRF	Multiple Reference Frame
MSOGI	Multiple Second Order Generalized Integrator
MVC	Minimum Variance Controller
OSG	Orthogonal Signal Generator
PD	Phase Detector
PLL	Phase Lock Loop
PMSG	Permanent Magnet Synchronous Generator
PWM	Pulse Width Modulation
RLS	Recursive Least square
RSC	Rotor Side Converter
SCIG	Squirrel Cage Induction Generator
SMC	Sliding Mode Control
SMO	Sliding Mode Observer
SOSMO	Second Order Sliding Mode Observer
SRF	Synchronous Reference Frame
SSLKF	Steady-state Linear Kalman Filter
ST	Self Tuning
UPF	Unity Power Factor
VCO	Voltage Controlled Oscillator
VSCF	Variable Speed Constant Frequency
WECS	Wind Energy Conversion System

List of Symbols

Symbol	Definition	Units
C	Capacitance of the DC bus	F
f_g	Frequency of the grid voltage	Hz
f_s	Frequency of the stator voltage	Hz
f_{sl}	Slip frequency	Hz
i_a, i_b, i_c	Three-phase grid currents	A
i_{ar}, i_{br}, i_{cr}	Three-phase rotor currents	A
i_{as}, i_{bs}, i_{cs}	Three-phase stator currents	A
i_d, i_q	Grid currents in SRF (dq)	A
i_d^*, i_q^*	Reference grid currents in SRF (dq)	A
$i_{dr}, i_{qr},$	d and q axis rotor currents	A
$i_{dr}^*, i_{qr}^*,$	Reference d and q axis rotor currents	A
I_{os}	Total DC side current	V
I_{or}	DC load current	A
$i_\alpha, i_\beta,$	Grid currents in stationary reference frame ($\alpha\beta$)	A
$i_{\alpha r}, i_{\beta r},$	Rotor currents in stationary reference frame ($\alpha\beta$)	A
$i_{\alpha s}, i_{\beta s},$	Stator currents in stationary reference frame ($\alpha\beta$)	A
L_f	Inductance of the grid filter	H
L_{ls}	Leakage inductance of the stator	H
L_{lr}	Leakage inductance of the rotor	H
L_m	Mutual inductance	H
L_r	Rotor inductance	H

L_s	Stator inductance	H
P_g^*	Desired active power exchange between the grid and GSC	W
P_g	Active power exchange between the grid and GSC	W
P_l	Load power for the load connected across the DC bus	W
$\hat{P}_l$	Estimated load power	W
P_r^*	Desired active power exchange between the grid and the rotor	W
P_{wtg}^*	Reference power for the turbine controller	W
Q_s^*	Reactive power set point of the stator	VAr
Q_g^*	Desired reactive power exchange between the grid and the GSC	Var
Q_g	Reactive power exchange between the grid and GSC	W
R_{dc}	DC load resistance connected across the DC bus	Ω
r_f	Resistance of the grid filter	Ω
R_r	Rotor resistance	Ω
R_s	Stator resistance	Ω
T_g^*	Generator torque set point	Nm
V_{dc}^*	DC bus voltage reference	V
V_{dc}	DC bus voltage	V
v_{af}, v_{bf}, v_{cf}	Three-phase front-end converter outputs	V
v_{ag}, v_{bg}, v_{cg}	Three-phase grid voltages	V
v_{ar}, v_{br}, v_{cr}	Three-phase rotor voltages	V
v_{as}, v_{bs}, v_{cs}	Three-phase stator voltages	V
v_{dg}, v_{qg}	Grid voltages in SRF (dq)	V
v_{df}, v_{qf}	Converter outputs in SRF (dq)	V
$\left\|\vec{v}_g\right\|$	Grid voltage space vector	V
$v_{dr}^*, v_{qr}^*,$	Reference rotor voltages is in SRF (dq)	V
$v_{\alpha f}, v_{\beta f},$	Converter outputs in stationary reference frame ($\alpha\beta$)	V
$v_{\alpha g}, v_{\beta g},$	Grid voltages in stationary reference frame ($\alpha\beta$)	V

$v_{\alpha r}, v_{\beta r},$	Rotor voltages in stationary reference frame ($\alpha\beta$)	V
$v_{\alpha s}, v_{\beta s},$	Stator voltages in stationary reference frame ($\alpha\beta$)	V
$\lvert\vec{v}_s\rvert$	Amplitude of the stator voltage	V
$\lvert\vec{v}_s\rvert^*$	Reference amplitude of the stator voltage	V
β^*	Reference pitch angle	rad
θ_g	Phase angle of the grid voltage	rad
θ_g^e	Estimated phase angle of the grid voltage	rad
θ_r	Rotor position or angle	rad
$\hat{\theta}_r$	Estimated rotor position	rad
θ_s^*	Reference phase angle of the stator voltage	rad
$\hat{\theta}_{sl}$	Estimated slip angle	rad
$\psi_{\alpha r}, \psi_{\beta r}$	Rotor Fluxes in stationary reference frame ($\alpha\beta$)	Wb
ω_c	Cut-off frequency of the LPF	rad/s
ω_g	Angular frequency of the grid voltage	rad/s
ω_g^e	Estimated angular frequency of the grid voltage	rad/s
ω_r	Rotational speed of the rotor	rad/s
ω_s^*	Reference angular frequency of the stator voltage	rad/s
$\hat{\omega}_r$	Estimated rotational speed of the rotor	rad/s
ω_{sl}	Slip speed	rad/s
$\hat{\omega}_{sl}$	Estimated slip speed	rad/s
ω_m^*	Reference mechanical rotor speed	rad/s

List of Figures

List of Tables

1

Introduction

Contents

1.1 Motivation

The world energy demand is growing steadily and to meet this growing demand it is required to have renewable energy sources for sustainable grid or micro-grid. From the beginning of the 21^{st} century, the emphasis of energy research shifts towards renewable sources for having a sustainable means of energy production. There are many renewable sources like the ocean wave, geothermal, biomass, solar, wind, etc. Among these, wind and solar [1–4] are the most widely used renewable energy sources, which are partly fulfilling the huge energy demands of modern societies by sustainable means. Presently, energy generation from wind is gaining momentum all over the world, and it will grow further due to the invention of new technologies related to the offshore wind farm installation. Speedy growth in terms of the new installation of wind farms is observed since 2010. According to the Global Wind Energy Council (GWEC) report of 2019, a total of 591 GW of wind energy plant has been installed around the world up to 2018. In the year of 2018, 51.3 GW of new wind energy plant is installed. Since 2014, the annual installation has touched 50 GW mark each year [3]. According to the report published in January 2020 from the Ministry of New and Renewable Energy (MNRE) India, India has a total installed capacity of 37.5 GW, which places India in the fourth position for wind energy generation [4]. This report also publishes that the goal is to enhance India's installed capacity of wind energy generation to 60 GW within 2022 [4].

Till the mid-1990s, squirrel cage induction generator (SCIG)-based fixed speed wind energy conversion systems (WECS) were the most significant contributor of renewable energy generation from wind. Presently, it is observed that most of the WECSs are variable speed constant frequency (VSCF) type, which is more efficient than the fixed speed ones. These VSCF-based WECSs convert the wind energy into electrical energy utilizing either the double-fed induction generator (DFIG) or the permanent magnet synchronous generator (PMSG). Among these, DFIG operates with a low-rated power converter which makes it cost-effective, and highly efficient.

Further, decoupled control of active and reactive power can be achieved for DFIG-based WECS. These salient features motivate this present work to develop robust and efficient control strategies for smoother operation of DFIG-based WECS. An overview of a DFIG-based WECS is presented in the next section.

1.2 Configuration of a WECS with DFIG

The schematic diagram of a typical DFIG-based WECS is shown in Figure 1.1. The shaft of the wind turbine is connected with the generator shaft utilizing a gearbox unit. The crucial electrical subsystems of a typical DFIG-based WECS consists of two back-to-back, bidirectional three-phase power converters and a DFIG. The DFIG has two main parts- stator, and rotor; the three-phase stator terminals are directly connected to the grid. The three-phase rotor terminals are connected to a three-phase converter called the rotor side converter (RSC). The DC side of the RSC is connected with another three-phase converter called the grid side converter (GSC) or the stator side converter (SSC). One DC link capacitor is placed between the connection of the two converters. The three-phase terminals of the GSC are connected with the grid utilizing a three-phase grid filter. These converters are bidirectional in nature, and they ensure the bidirectional energy transfer between the grid and the DFIG rotor. The control structure of a DFIG-based WECS is discussed in the following paragraph.

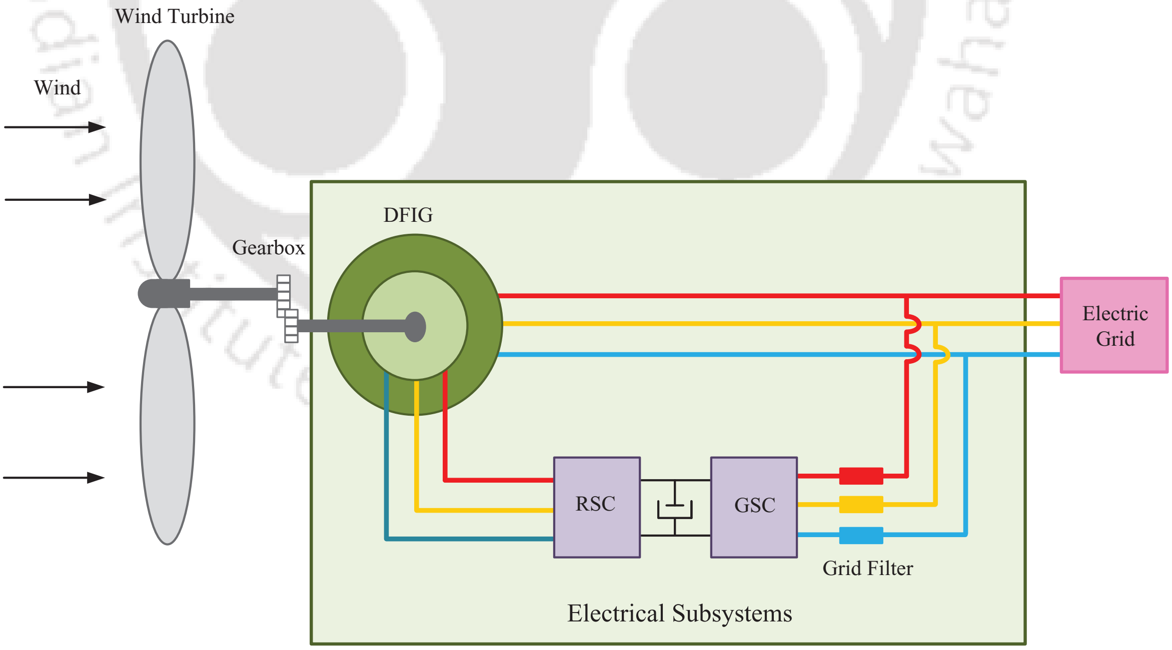

Figure 1.1: Schematic diagram of a DFIG-based wind energy conversion system (WECS)

In Figure 1.2, the control structure of a typical DFIG-based WECS is presented. Since mechanical dynamics are much slower than the electrical dynamics of a WECS, a hierarchical control structure

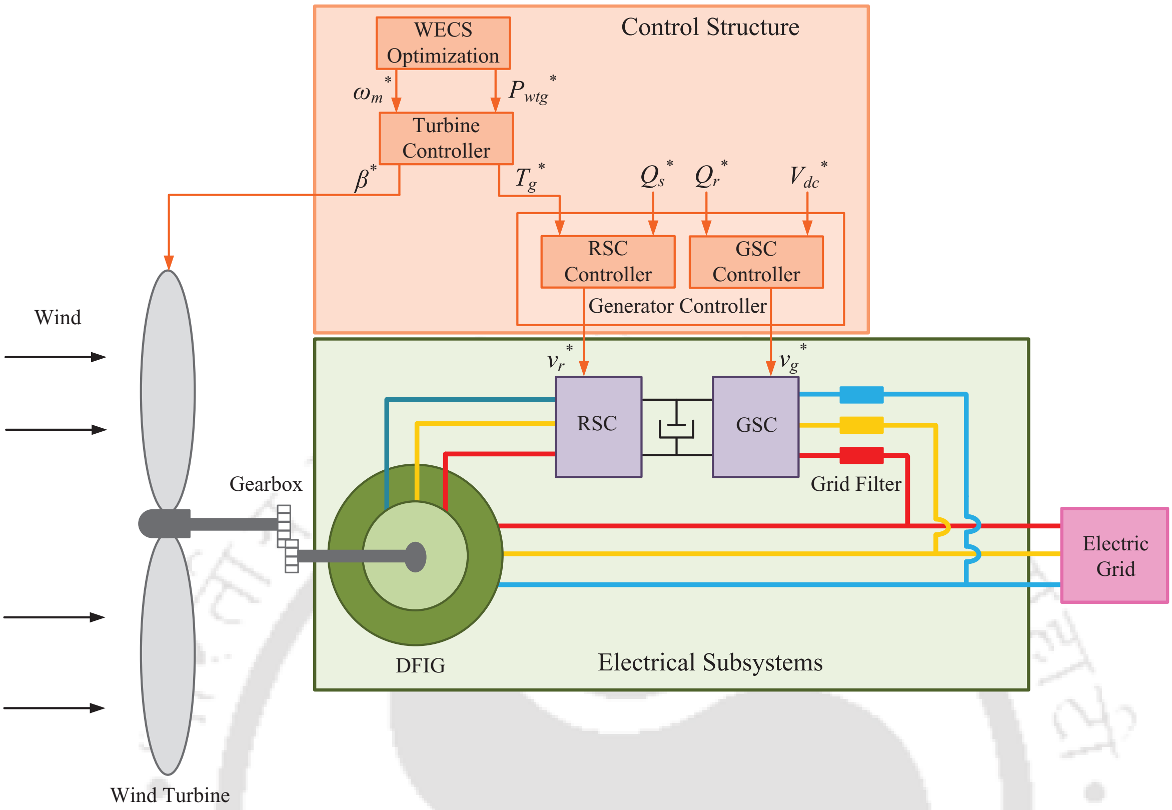

Figure 1.2: Control system hierarchy of a DFIG-based WECS

can be implemented in the case of a DFIG-based WECS (Figure 1.2) [5]. Three control levels are generally used, such as WECS optimization level, turbine control level, and generator control level. WECS optimization level drives the WECS to track the optimal operating trajectory by implementing a maximum power point tracking (MPPT) algorithm. This level computes the reference rotor speed ω_m^* and reference power P_{wtg}^* for the turbine controller. The turbine controller controls the turbine speed and mechanical power input to the generator by manipulating the pitch angle set-point β^* of the turbine blade and the generated torque set-point T_g^*. The generator controller consists of two controllers, namely RSC and GSC controllers. Essentially, the RSC controller is used to control the supply of active power and regulate the reactive power Q_s^* exchange between the grid and the stator of the DFIG. The primary task of the GSC controller is to maintain the desired value of the DC bus voltage V_{dc}^* and to ensure the desired flow of active power P_r^* between the grid and the rotor. Another task of the GSC controller is to regulate the reactive power Q_r^* exchange between the grid and the GSC. This thesis work intends to improve the generator controller by improving the RSC and GSC controllers. It also includes the development and implementation of the robust observers for better control of the RSC and GSC/SSC controllers. The thesis mainly focuses on the standalone DFIG-based WECSs, which are extensively used to extract wind energy for small scale applications. An overview of standalone DFIG-based WECS is presented in the following section.

1.3 Overview on standalone DFIG-based WECS

Remote areas of India like Ladakh, parts of Sikkim and Arunachal Pradesh, and other several remote areas of different north-east states of India are not connected with the electric grid. A similar type of scenario can also be observed for other remote areas of the world. Hence, an off-grid solution like standalone DFIG-based WECS may play a major role in the form of a sustainable means to mitigate the energy demand of the remote places of the world.

The standalone configuration differs a little bit from the grid-connected configuration for the DFIG-based WECS. Single DFIG-based WECS is not reliable to supply stable and steady power to the load. Figure 1.3 shows a typical standalone system with DFIG, solar and a battery energy storage. In standalone mode, the DFIG stator is connected with a three-phase load, and the GSC is connected with the stator through a passive filter. A filtering capacitor can be placed in the stator to reduce the high-frequency harmonics generated due to the RSC and GSC operation. In standalone mode, the control task of the GSC remains the same as the grid-connected mode; however, there is a change in the control task of the RSC in standalone mode. The primary control task of the RSC in standalone mode is to maintain the desired voltage and frequency at the stator terminal under the variable speeds of the wind turbine. The control of the RSC and GSC involves complex subsystems; thus, there is a need to develop better controllers and observers for standalone DFIG-based WECS. The present thesis is mainly dedicated towards the design and implementation of robust controllers and observers for RSC and GSC converters for a standalone DFIG-based WECS.

1.4 Literature review

The generator controller consists of GSC and RSC controllers (Figure 1.2). The phase-lock-loop (PLL) system is one of the important subsystem, which plays a significant role in the performance of

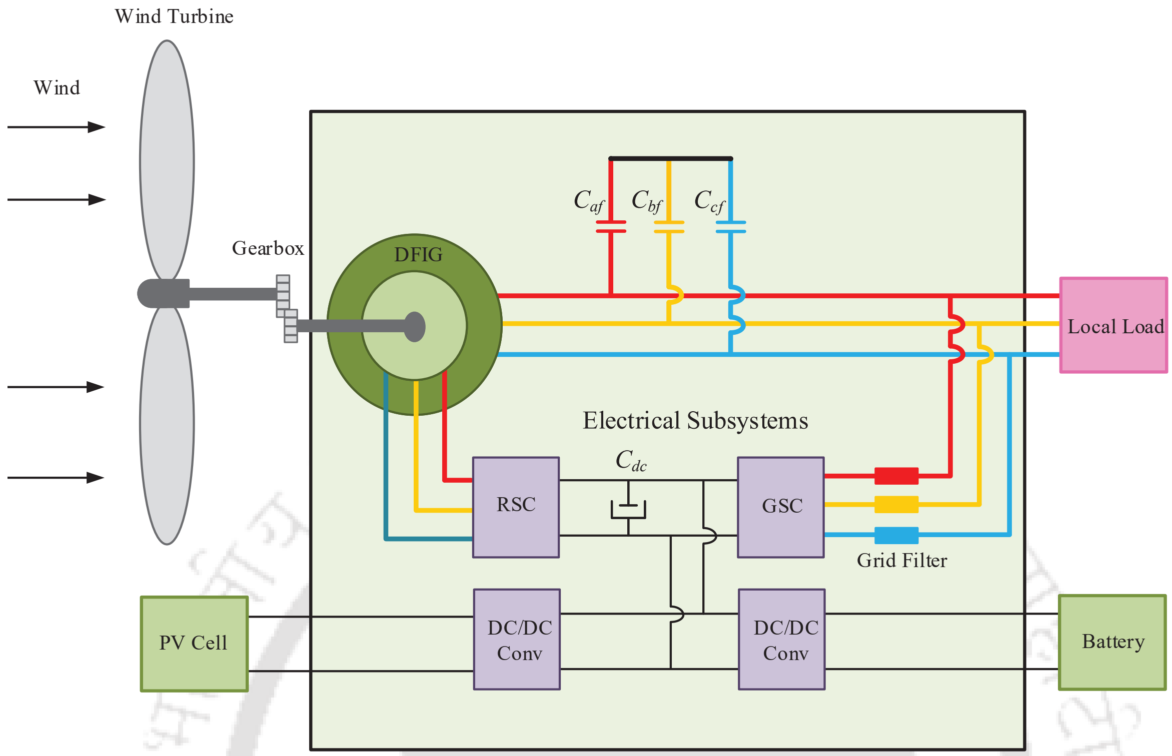

Figure 1.3: Schematic diagram of a typical standalone system with DFIG, solar and a battery energy storage

a GSC controller [6]. Moreover, the RSC controller's performance depends on the accuracy of the measurement of the rotor speed [6]. The following subsections present the literature related to the PLL, GSC and RSC controllers.

1.4.1 Literature survey on GSC controller

The GSC control system typically consists of two cascaded control loops and a PLL system. The outer loop controls the DC link voltage, whereas the inner loop regulates the grid currents. Usually, vector control techniques are applied to control the active and reactive component of the three-phase grid current to regulate the active and reactive power exchange with the grid/stator [6, 7]. The estimated phase from the PLL is utilized to convert the three-phase sinusoidal variables in the stationary reference frame (*abc*) of the grid (voltage and current) to two-phase stationary DC variables in the synchronously rotating reference frame (*dq*). In this process, the output voltage of the front-end converter is synchronized with the grid automatically by the PLL [8–11]. Thus PLL plays a critical role in controlling the front-end converter and synchronizing it with the grid/stator [12, 13]. The detailed literature review on PLL systems and the control loops are presented below.

1.4.1.1 Literature survey on PLL systems

There are various strategies associated with the design and implementation of a PLL. A PLL typically consists of three fundamental building blocks, i.e., a voltage-controlled oscillator (VCO), a loop filter (LF: generally is a PI controller), and a phase detector (PD). It is observed from the available literature, that the LF and VCO are not considered much for further study. Various studies on the improvement of PD technique are widely available in the literature. One of the most popular PD technique is the synchronous reference frame (SRF) transformation technique [14–17]. The SRF-PLL works fine when the grid-voltages are balanced, stable, and free from harmonics. However, with the presence of harmonics, unbalance, and grid disturbances, the performance of SRF-PLL degrades sharply, i.e., there is an error in the estimated phase and frequency of the grid voltage, which significantly affects the control of power converters [18]. Some improvements in terms of disturbance rejection capability can be achieved by reducing the bandwidth of the LF [19] but at the cost of poor dynamic response.

Different types of enhanced filter-based algorithms such as multiple reference frame (MRF), multiple second-order generalized integrator (MSOGI), multiple complex coefficient filter (MCCF), and delayed signal cancellation (DSC) based methods are suggested by different researchers [13, 19–23] for improving the robustness and accuracy of the estimated phase and frequency by the PLL. In [19], a systematic approach is proposed to design several enhanced filter-based SRF-PLLs. The paper presents LPF, MRF, MSOGI, and MCCF based PLLs and discusses a step by step procedure to design the controller (LF) parameters. The small-signal model is similar for the MRF, MSOGI, and MCCF based PLLs, and the same design approach can be employed for the LF design. The current controller based on reduced order generalized integrator (ROGI) has been proposed in [21], which can be compared with the traditional SOGI technique with a lesser computational complexity. However, the realization of this technique is not easy. MRF theory-based PLL is designed in [13, 20] and it is capable of reducing the harmonics but are computationally very expensive as compared to the conventional SRF-PLL. In [22], a complex vector filtering based method (CVFM) is proposed to get rid of the harmonics and all other grid abnormalities during the calculation of phase angle and frequency. However, this method utilizes a complex theory and has higher computational complexity. MCCF-based PLL technique [23] is presented for the estimation of the grid phase angle and frequency. It does not require any rotating frame transformations to extract the fundamental frequency positive sequence (FFPS), and fundamental frequency negative sequence (FFNS). However, it is not easy to implement and have computational complexity similar to that of the MRF method [19]. In-loop DSC based PLL is presented in [24, 25], which works fine and has good disturbance rejection capability at the cost of slow dynamic performance [10]. SOGI based PLL is designed for a single-phase system in [26], which can also be used with the three-phase system. From the viewpoint of control, the two PLL systems- MRF and MSOGI are very similar, and their computational complexity is comparable to each other [19]. An orthogonal signal generator (OSG) based SOGI-PLL is proposed in [27] for a single-phase system to reject disturbance in phase angle and frequency estimation due to the offset in the input voltage, which is similar to the work proposed in [26]. In [28], an adaptive approach is proposed to compensate for the effect of phase jump in grid-voltage. This technique is constructed based on adaptive regulation of the gain of the frequency observation loop for reducing the transients in frequency during startup and phase jump. This strategy can be used with enhanced-PLL (EPLL) or normal SRF-PLL or with SOGI based PLL technique. However, the focus of the work in [28] only concentrates on the startup of PLL and phase jump. In general, the startup problem of PLL will not greatly influence the operation of the grid-tied converter, and it can be appropriately countered by implementing the right control sequence for the incoming power converter.

Steady-state linear Kalman filter (SSLKF) based PLL is implemented in [29–31]. SSLKF and Discrete Fourier transformation (DFT) based PLL technique is implemented and compared [31], which can work in flexible supply frequency, in general, between 360 Hz to 900 Hz. These algorithms are sophisticated but very complex to realize, and the computational complexity is more than the other well-known algorithms [10].

1.4.1.2 Literature survey on cascaded control loops of GSC/SSC

The GSC controller consists typically of two cascade control loops. The inner control loop is the current control loop that regulates the active and reactive component of the grid currents, whereas the outer control loop regulates the DC bus voltage. The outer loop generates the reference signal (the active component of the grid current) for the inner current control loop. The active component of the current decides the amount of active power exchange with the grid, whereas the reactive component of the current decides the amount of reactive power exchange with the grid. Thus, the control objective of a GSC controller is to maintain constant DC link voltage across the DC bus capacitor with a user-defined power factor [7, 32, 33].

A variety of control techniques to control the grid current is presented in the literature to achieve the aforementioned control objectives. The prevalent technique is the utilization of linear PI regulators for controlling the active and reactive current components [7, 32, 34]. However, this technique suffers from the slow dynamic response. Deadbeat control is used in [35] to control the grid currents, and a swift dynamic performance can be realized. However, this method suffers from parametric uncertainties associated with the plant parameter. In addition to that, large-signal disturbances affect the stability of the system due to the presence of nonlinearities in the power converters.

Various nonlinear control techniques are proposed to realize the control objectives for these power converters, such as model predictive control [36–38], nonlinear adaptive control [39], model-reference adaptive control [40], passivity-based control [41], input-output linearization [42], fuzzy logic based control [43, 44], artificial neural network (ANN) based control [45, 46], sliding-mode control (SMC) [47–50] and second-order sliding mode (SOSM) control [51–53].

Among these, SMC and adaptive control techniques are more effective in handling the nonlinearities of the plant and uncertainties associated with the plant parameters. The crucial asset of SMC is that it has switching property that occurs at infinitely high frequency to remove fluctuation from sliding manifold. However, from a real-world perspective, the practically available device cannot switch at very high frequency. Hence, for practical purposes, the SMC is constrained to work at lower frequencies, which leads to chattering problems [54, 55]. Different methods have been presented to decrease the chattering problem such as the implementation of the saturation function as an alternative to the signum function, or the use of low pass filter (LPF) at the output [56, 57].

SMC-based techniques require a priori idea about the bounds on the uncertain or time-varying parameters. The SMC control law does not change for the changes in the plant parameters. Adaptive control changes its control law itself to control the plant subjected to uncertain or time-varying parameters.

Different control techniques to control the DC bus voltage are available in the literature. The most common technique is the use of a linear PI regulator to regulate the DC link voltage. However, this technique suffers from slow dynamic performance, and an additional increase in bandwidth affects the disturbance rejection capability. In [51], an extended state observer (ESO) augmented H_∞ controller is proposed to tackle this problem, where the DC side load resistance is estimated by the ESO technique. However, experimental validation is not provided for the same. A second-order sliding mode (SOSM) controller augmented with an ESO is designed in [52] to control the DC bus voltage. It can be observed from [51], and [52] that, fast and seamless tracking of the reference DC bus voltage is possible with these ESO-based techniques.

1.4.2 Literature survey on RSC controller

The RSC controller has a similar structure like the GSC controller for a DFIG-based WECS system. Vector control techniques are typically utilized to fulfil the control objectives of the RSC controller. The objective of the RSC controller in a grid-connected mode is to control active and reactive power supplied by the stator of the DFIG. In standalone mode, the objective of the RSC is to maintain a constant voltage and frequency at the stator terminal under varying load and wind speed variations. The three-phase machine (DFIG) variables like rotor current are transformed to two-phase DC variables for implementing the vector control techniques. The transformation uses the information of the rotor position/angle (θ_r) and the grid-voltage phase-angle (θ_g) for a grid-connected system or the stator voltage phase angle (θ_s) for a standalone system. Thus, the accurate information of the rotor speed and rotor angle is the most crucial information for the working of the RSC controller. The rotor angle can be calibrated by the rotary encoder; however, encoders come with hardware complexity; they are prone to failure, and are costly. These issues make encoders less reliable for the RSC controller implementation. Hence, an encoder/sensor-less operation is preferred for a DFIG-based WECS. A rigorous investigation has been conducted on the speed sensorless operation of DFIG-based WECS in [58] to enhance the reliability issue related to the speed and position information.

A literature survey reveals that essentially there are two categories of speed sensorless control technique employed for the DFIG-based WECS. The first one is the saliency-based techniques, and the other one is the model-based techniques. The saliency-based methods are mostly centered on signal injection technique [59–61]. However, saliency-based methods are sensitive to grid impedance.

Different model-based approaches for the speed estimation of DFIG systems are widely found in literature, such as flux observers, model reference adaptive system (MRAS), extended Kalman filters (EKF), and sliding mode observers (SMO) [62–68].

The simple flux-based observer is proposed in [62], where slip speed is calculated by implementing an inverse tangent function on stator fluxes and rotor currents. However, the estimated states may be sensitive towards input disturbances and parametric uncertainties. MRAS-based observers are quite common for sensorless control technique [63–65]. This technique uses one reference model and one adjustable model for calculating the same signal to drive the adaptive mechanism. Generally, either the stator or rotor flux or the rotor or stator current is considered as the regulating signal [64]. However, these techniques require an accurate estimate of the machine parameters. To mitigate this, many researchers have proposed different techniques augmented with the MRAS observers [69, 70]. However, augmenting these techniques further increases the complexity. In [69], adaptive tuning of the stator inductance is presented to compensate the effect of parametric uncertainties on the rotor current based MRAS observer. Recursive least square (RLS) augmented minimum variance controller (MVC) based speed estimation technique is proposed in [70]. The small-signal model of the MVC-based estimator has a similar structure as the MRAS-based observer, where the PI controller of the MRAS observer is replaced by RLS augmented MVC controller. EKF based speed estimators are designed for the DFIG system in [66]. However, these techniques are very sophisticated and computationally complex than the other observers. In addition to that, the work [66] does not include the hardware verification of this technique on the DFIG-based test system.

The speed estimation algorithm based on sliding mode observer (SMO) is robust to parametric uncertainties, easy to realize, and less sensitive towards the change in load. In [68], SMO is applied to estimate the stator currents. The inverse tangent function is applied to determine the rotor position. However, this technique may be affected by input noise due to the implementation of the inverse tangent function. In addition to that, it does not provide a systematic design procedure to find sliding gains. Sensorless direct power control (DPC) of DFIG based on SMO is presented in [71]. The stator flux is used as the tuning signal for the observer. The error of the stator flux components is directly computed and passed through the sign function, and the rotor position is estimated by implementing an inverse tangent function. However, the design procedure of the sliding gains is not provided. Moreover, the paper does not include a hardware verification of the observer. A higher-order SMO (HSMO) is designed in [72] to estimate the rotor speed. However, a systematic design procedure, dynamic performance analysis during step change, and hardware verification are not provided.

A recent study regarding slip-speed and slip-angle/position estimation for sensorless control of the rotor-tied DFIG system is presented in [73, 74]. The estimator is designed based on the PLL-augmented SMO. Stator current and the back electromotive force are considered as the state variables for this PLL-based SMO. In [74], a comparison is made between the PLL-augmented higher-order and second-order SMO techniques for the estimation of slip-speed and position of a rotor-tied DFIG-based WECS. However, these techniques are proposed for the rotor-tied DFIG systems, and this topology is different from the stator-tied DFIG systems.

Different other control strategies for the RSC controller have been proposed to fulfil the control objectives, for instances, direct torque control [75, 76], direct power control [77–79], and decoupled $P - Q$ control [80, 81]. However, the successful operation of all these strategies depends on the accurate measurement or estimation of the rotor speed and angle.

1.5 Scope and objectives

Based on the literature survey discussed in the previous section, the present thesis work focuses on developing efficient, robust, reliable, and cost-effective solutions for the generator control of a standalone DFIG-based WECS. The important subsystems like the PLL, rotor speed observer are developed here to make the RSC and GSC controllers more robust and cost-effective. The thesis objectives are summarized as follows.

- Literature review on PLL systems reveals that several techniques have been proposed to estimate phase angle and magnitude of the grid-voltage. Among these, there are several enhanced filter-based algorithms which provide high performance under different grid abnormalities. However, these methods have high computational complexity. Hence, there is a need for a reliable, simple, yet robust PLL to estimate the grid voltage's frequency and phase angle accurately in the presence of different grid abnormalities.

- It has been observed from the literature that several control strategies have been proposed to fulfil the control objective of the GSC/SSC controller. However, due to the nonlinearities and parameter uncertainties associated with the GSC, the GSC controller must be insensitive towards any parametric variations, stable against large-signal disturbances, and work seamlessly under different operating points while fulfilling the various performance criteria like fast convergence, high accuracy and low overshoot. Hence a robust, efficient, and cost-effective solution is required to fulfil the control objective of the GSC.

- From the literature survey on different RSC controllers, it can be observed that the successful operation of the RSC controller depends on the accuracy of the measured or estimated rotor speed and angle. Thus, a reliable, robust, and cost-effective solution is required for estimating the rotor speed and position. Furthermore, the speed estimation scheme needs to be robust to any parametric variations of the machine, and it must work accurately for different operating points while satisfying the various performance criteria.

- Finally, a speed sensor-less voltage control scheme using the developed speed observer is required to implement for controlling the stator voltage and frequency of the standalone DFIG system. This sensorless scheme must regulate the desired stator voltage magnitude under a load change at the DFIG stator terminal and a speed change of the rotor.

1.6 Thesis organization

Rest of the thesis is organized as follows:

- Chapter 2 presents the work on the PLL system. Here, a robust PLL is developed using two in-loop notch filters and one low pass filter (LPF). The LPF, along with notch filter, has good filtering capability but has a poor transient performance. Hence, the proposed algorithm tries to improve the performance by including the derivative gain in the loop filter. The PLL algorithm is implemented in hardware test system developed in the laboratory. The performance of the proposed algorithm is comparable and involves less-complexity than some of the widely used methods such as MRF-PLL.

- Chapter 3 presents the design and development of the adaptive multiple-input multiple-output (MIMO) controller to control the active and reactive grid currents for the front-end converter. In addition to that, an extended state observer (ESO) augmented adaptive control law is derived for the DC bus voltage control. Lyapunov stability criteria are used to derive both the control laws while ensuring stability and performance. Further, the control algorithms are implemented on a hardware prototype to validate their performance.

- Chapter 4 presents a smooth, robust controller in the form of a first-order sliding mode controller (FOSMC) to control the active and reactive components of the grid currents for the front-end converter. Lyapunov stability criteria are used to derive the sliding gains for the FOSMC, which makes the control law stable. Further, the control algorithm is implemented on a hardware test-bed to validate its performance.

- Chapter 5 presents the design and development of an efficient, robust observer in the form of a first-order sliding mode observer (FOSMO) to estimate the rotor speed and position of the DFIG. Lyapunov stability criteria are utilized to design the sliding gains for the developed observer. The observer is implemented in a hardware test setup, and the dynamic performance is evaluated in different test conditions. To explore the efficacy of the FOSMO algorithm, a sensorless voltage control scheme is implemented in hardware test-bed for the standalone DFIG-based WECS.

- In Chapter 6, a second-order sliding mode observer (SOSMO) is developed for estimating the rotor speed and tested in the hardware test-bed. In reality, the performance of the two observers is comparable; however, the SOSMO tries to mitigate the phenomena of chattering due to low-speed sampling.
- Finally, Chapter 7, draws the conclusions of the work done in this thesis, and suggest some future works.

2

Development of a simple yet robust technique for the improvement of phase-lock-loop (PLL) system

Contents

2.1 Introduction

Phase-lock-loop (PLL) system is an important subsystem of a front-end converter control system. The accuracy of the control system depends upon the accuracy of the PLL system. Literature survey reveals that, the SRF-based PLL technique is the most popular technique to estimate the phase and frequency of the grid voltage. Figure 2.1 demonstrates the elementary structure of a conventional SRF-PLL.

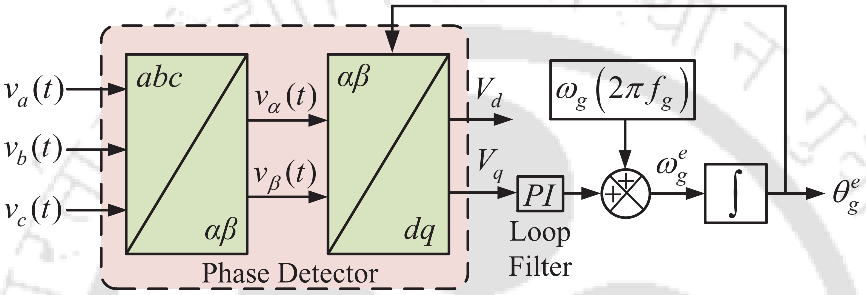

Figure 2.1: Schematic diagram of the conventional SRF-PLL

In this scheme, the measured grid voltages i.e., $v_a(t)$, $v_b(t)$, and $v_c(t)$ are transformed from *abc* to *αβ* (Clark transformation) and then from *αβ* to *dq* (Park transformation). For a balanced three-phase voltage, this *abc* to *dq* transform will produce a DC value of v_d and v_q, provided the *dq* reference frame is rotating at synchronous speed, i.e., the tracking of frequency and phase of the grid voltage is achieved. Now, by reducing the value of v_q to zero, with the help of the controller (loop-filter (LF)), it is possible to align the *d*- axis with the grid voltage space vector $|\vec{v}_g|$. Thus, it is possible to track the frequency and phase of the grid voltage using this scheme.

It is observed that the conventional SRF-PLL fails to provide the required accuracy due to the increasing number of nonlinear loads and the integration of renewable energy sources into the grid. To overcome this situation, a variety of enhanced filtering based PLLs have been reported in the literature, but the enhanced filtering capability comes with its own complexity, as, they are computationally more complex [10, 19].

This chapter discusses the development of a simple, computationally less involved yet robust solution to the above problem by implementing in-loop low pass filter (LPF) and notch filters. The LPF, along with notch filter has good filtering capability but has poor transient performance; thus, the proposed algorithm tries to improve the performance by including the derivative gain in the loop filter. It is observed from experimental results that the performance of the proposed method is comparable to some of the widely used methods such as MRF-PLL with less computational complexity.

2.2 Small signal analogy of the proposed PLL

The proposed PLL is a modified version of the conventional SRF-PLL. Figures 2.2 and 2.3 represents the modified structure of LPF-based SRF-PLL and schematic of the small-signal model, respectively. Two notch filters have been added to filter out the two lower-order harmonics. Loop filter has been rearranged as PID controller instead of PI type. This in-loop LPF, along with notch filters is minimally affected by grid disturbances while tracking the phase and frequency of the three-phase grid. To understand the working of the proposed PLL, a small signal analogy is presented in the next paragraph.

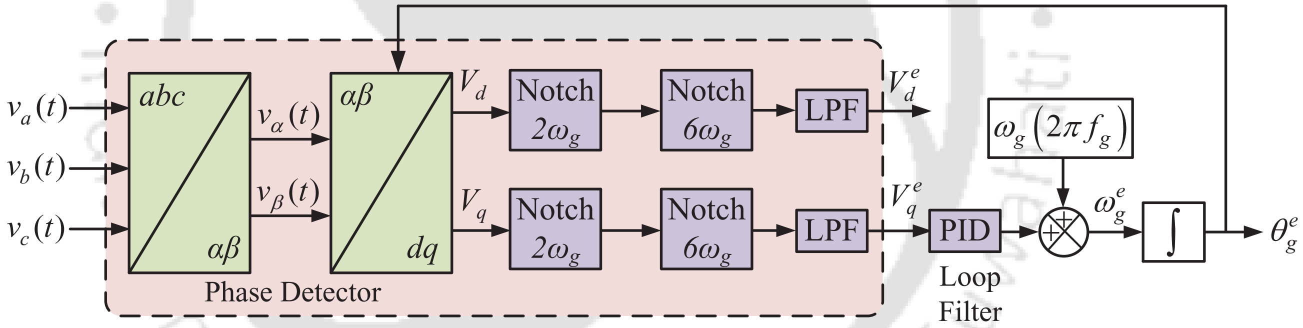

Figure 2.2: Overall structure of the proposed PLL

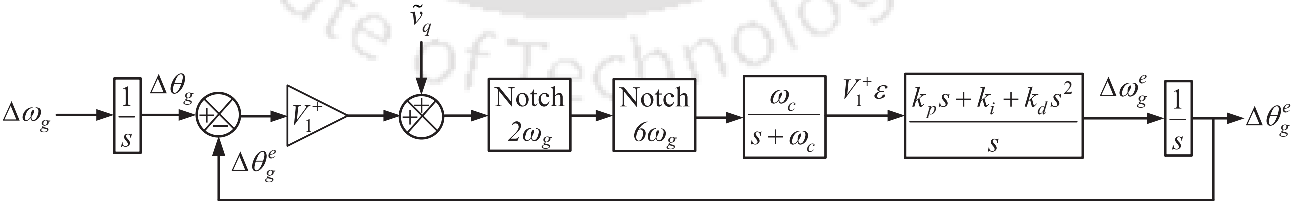

Figure 2.3: Schematic of the small signal model for the proposed PLL

The small signal analysis has been done by assuming the pseudo-lock state where the estimated phase and frequency variables are believed to be exactly equal to the true values [19]. Here, θ_g^e is the estimated phase and $\omega_g^e = 2\pi f_g^e$ is the estimated angular frequency and ω_g is the grid's nominal angular frequency, v_d^e and v_q^e are the d and q axis voltages in the transformed domain (here subscript g refers to grid variable and superscript e refers to estimated quantity). The value of grid frequency considered for the study $\left(f_g\right)$ is 50 Hz. The three-phase grid voltages $(v_a(t), v_b(t), v_c(t))$ are the input to the PLL system.

According to symmetrical component theory, any unbalanced set of three-phase quantities (without DC components) can be transformed into two balanced sets, namely positive and negative sequences [82]. Hence, harmonically distorted and unbalanced three-phase voltages can be expressed as (2.1):

$$\begin{aligned}
v_a(t) &= \sum_{n=1}^{\infty}\left[V_n^+ \sin\left(n\omega_g t\right) + V_n^- \sin\left(n\omega_g t\right)\right] \\
v_b(t) &= \sum_{n=1}^{\infty}\left[V_n^+ \sin\left(n\omega_g t - \tfrac{2\pi}{3}\right) + V_n^- \sin\left(n\omega_g t + \tfrac{2\pi}{3}\right)\right] \\
v_c(t) &= \sum_{n=1}^{\infty}\left[V_n^+ \sin\left(n\omega_g t + \tfrac{2\pi}{3}\right) + V_n^- \sin\left(n\omega_g t - \tfrac{2\pi}{3}\right)\right]
\end{aligned} \tag{2.1}$$

The expression for the voltages in $\alpha\beta$ domain can be written as:

$$\begin{bmatrix} v_\alpha(t) \\ v_\beta(t) \end{bmatrix} = \left[K_{\alpha\beta}\right] \begin{bmatrix} v_a(t) \\ v_b(t) \\ v_c(t) \end{bmatrix} = \begin{bmatrix} v_\alpha^+(t) \\ v_\beta^+(t) \end{bmatrix} + \begin{bmatrix} v_\alpha^-(t) \\ v_\beta^-(t) \end{bmatrix} \tag{2.2}$$

where $\left[K_{\alpha\beta}\right]$ is expressed as:

$$\left[K_{\alpha\beta}\right] = \frac{2}{3}\begin{bmatrix} 1 & -\frac{1}{2} & -\frac{1}{2} \\ 0 & \frac{\sqrt{3}}{2} & -\frac{\sqrt{3}}{2} \end{bmatrix}.$$

The expression for the positive and negative sequences $\alpha\beta$ quantity are expressed as

$$\begin{bmatrix} v_\alpha^+(t) \\ v_\beta^+(t) \end{bmatrix} = \begin{bmatrix} \sum\limits_{n=1}^{\infty} v_{\alpha,n}^+(t) \\ \sum\limits_{n=1}^{\infty} v_{\beta,n}^+(t) \end{bmatrix} = \begin{bmatrix} \sum\limits_{n=1}^{\infty} V_n^+ \sin\left(n\omega_g t\right) \\ \sum\limits_{n=1}^{\infty} V_n^+ \sin\left(n\omega_g t - \frac{\pi}{2}\right) \end{bmatrix} \tag{2.3}$$

$$\begin{bmatrix} v_\alpha^-(t) \\ v_\beta^-(t) \end{bmatrix} = \begin{bmatrix} \sum\limits_{n=1}^{\infty} v_{\alpha,n}^-(t) \\ \sum\limits_{n=1}^{\infty} v_{\beta,n}^-(t) \end{bmatrix} = \begin{bmatrix} \sum\limits_{n=1}^{\infty} V_n^- \sin\left(n\omega_g t\right) \\ -\sum\limits_{n=1}^{\infty} V_n^- \sin\left(n\omega_g t - \frac{\pi}{2}\right) \end{bmatrix}. \tag{2.4}$$

To convert $\alpha\beta$ quantity into stationary dq quantity, Parks transformation is applied:

$$\begin{bmatrix} v_d(t) \\ v_q(t) \end{bmatrix} = \left[K_{dq}\right] \begin{bmatrix} v_\alpha(t) \\ v_\beta(t) \end{bmatrix} = \begin{bmatrix} v_d^+(t) \\ v_q^+(t) \end{bmatrix} + \begin{bmatrix} v_d^-(t) \\ v_q^-(t) \end{bmatrix}. \tag{2.5}$$

where $\left[K_{dq}\right]$ is expressed as

$$\left[K_{dq}\right] = \begin{bmatrix} \cos(\theta_g^e) & \sin(\theta_g^e) \\ -\sin(\theta_g^e) & \cos(\theta_g^e) \end{bmatrix}.$$

and θ_g^e is expressed as $\theta_g^e = \left(\omega_g^e t - \frac{\pi}{2}\right)$ (Figure 2.4). The d-axis of the synchronously rotating reference frame is aligned with the voltage vector $\left|\vec{v}_g\right|$ which lags by $\frac{\pi}{2}$ from the phase-a axis at time instant $t = 0$ (Figure 2.4(a)). The expression for the positive and negative sequence d and q-axis voltages are

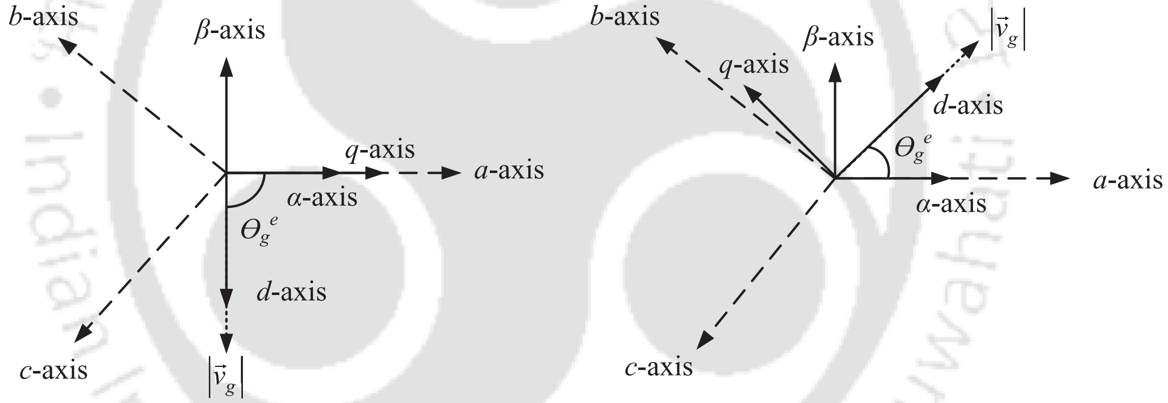

(a) (b)

Figure 2.4: Reference frame position during transformation; (a) Reference frame position at time $t = 0$ and (b) Reference frame position at any time instant t

$$\begin{bmatrix} v_d^+(t) \\ v_q^+(t) \end{bmatrix} = \begin{bmatrix} \sum\limits_{n=1}^{\infty} v_{d,n}^+(t) \\ \sum\limits_{n=1}^{\infty} v_{q,n}^+(t) \end{bmatrix} = \begin{bmatrix} \sum\limits_{n=1}^{\infty} V_n^+ \cos\left(n\omega_g - \omega_g^e\right) t \\ \sum\limits_{n=1}^{\infty} V_n^+ \sin\left(n\omega_g - \omega_g^e\right) t \end{bmatrix} \tag{2.6}$$

$$\begin{bmatrix} v_d^-(t) \\ v_q^-(t) \end{bmatrix} = \begin{bmatrix} \sum\limits_{n=1}^{\infty} v_{d,n}^-(t) \\ \sum\limits_{n=1}^{\infty} v_{q,n}^-(t) \end{bmatrix} = \begin{bmatrix} \sum\limits_{n=1}^{\infty} V_n^- \cos\left(n\omega_g + \omega_g^e\right) t \\ -\sum\limits_{n=1}^{\infty} V_n^- \sin\left(n\omega_g + \omega_g^e\right) t \end{bmatrix}. \tag{2.7}$$

Assuming a pseudo-locked condition $\left(\omega_g^e \approx \omega_g\right)$ the expression for dq- axis voltages can be written as

$$\begin{bmatrix} v_d(t) \\ v_q(t) \end{bmatrix} \approx \begin{bmatrix} \bar{v}_d \\ \bar{v}_q \end{bmatrix} + \begin{bmatrix} \tilde{v}_d(t) \\ \tilde{v}_q(t) \end{bmatrix} \tag{2.8}$$

The first term of the equation (2.8) is the stationary DC term and the last term is the disturbance input to the system. The DC term is the fundamental frequency positive sequence quantity and can be expressed as

$$\begin{bmatrix} \bar{v}_d \\ \bar{v}_q \end{bmatrix} = \begin{bmatrix} v_{d,1}^{+} \\ v_{q,1}^{+} \end{bmatrix} = \begin{bmatrix} V_1^+ \cos\left(\omega_g - \omega_g^e\right) t \\ V_1^+ \sin\left(\omega_g - \omega_g^e\right) t \end{bmatrix} = \begin{bmatrix} V_1^+ \cos\left(\theta_g - \theta_g^e\right) \\ V_1^+ \sin\left(\theta_g - \theta_g^e\right) \end{bmatrix} \approx \begin{bmatrix} V_1^+ \\ 0 \end{bmatrix} \tag{2.9}$$

The disturbance term can be written as

$$\begin{bmatrix} \tilde{v}_d(t) \\ \tilde{v}_q(t) \end{bmatrix} = \begin{bmatrix} \sum\limits_{n=2}^{\infty} V_n^+ \cos\left(n\omega_g - \omega_g^e\right) t \\ \sum\limits_{n=2}^{\infty} V_n^+ \sin\left(n\omega_g - \omega_g^e\right) t \end{bmatrix} + \begin{bmatrix} \sum\limits_{n=1}^{\infty} V_n^- \cos\left(n\omega_g + \omega_g^e\right) t \\ -\sum\limits_{n=1}^{\infty} V_n^- \sin\left(n\omega_g + \omega_g^e\right) t \end{bmatrix} \tag{2.10}$$

Furthermore, θ_g and θ_g^e can be expressed as

$$\begin{aligned} \theta_g &= \int \omega_g dt = \int \left(\omega'_g dt + \Delta\omega_g\right) dt = \theta'_g + \Delta\theta_g \\ \theta_g^e &= \int \omega_g^e dt = \int \left(\omega'^e_g dt + \Delta\omega_g^e\right) dt = \theta'^e_g + \Delta\theta_g^e. \end{aligned} \tag{2.11}$$

The value of θ_g and θ_g^e are replaced in (2.9) from (2.11). The DC term may be expressed as

$$\begin{bmatrix} \bar{v}_d \\ \bar{v}_q \end{bmatrix} = \begin{bmatrix} V_1^+ \cos\left(\Delta\theta_g - \Delta\theta_g^e\right) \\ V_1^+ \sin\left(\Delta\theta_g - \Delta\theta_g^e\right) \end{bmatrix} \approx \begin{bmatrix} V_1^+ \\ V_1^+ \varepsilon \end{bmatrix} \tag{2.12}$$

It has been clearly seen from (2.12) that $\bar{v}_d$ gives the estimate of the peak value of grid voltage and $\bar{v}_q$ gives the information about the error in phase detection. From (2.10), it can be observed that, under the pseudo-phase lock condition $\left(\omega_g^e \approx \omega_g\right)$, the fundamental negative sequence voltage of the input appears as the disturbance input to the small-signal model, and the frequency of the disturbance is twice of the fundamental wave. All other harmonics, which are basically non-triplen (neglecting even harmonics) odd harmonics, i.e., fifth, seventh, eleventh, thirteenth, etc. appear as even components such as sixth, twelfth, etc. to the small-signal model (Figure 2.3). Hence, $\tilde{v}_q$ is the disturbance input to the small-signal model which consists of mainly second, sixth, twelfth harmonic components [10, 12, 13, 18–20]. The two most dominant lower order harmonics are fifth and seventh; hence, two notch frequencies $\left(n = 2\omega_g, 6\omega_g\right)$ have been chosen to design the two in-loop notch filters. Further, to improve the filtering capability of the PLL technique, a low pass filter (LPF) is designed. The s-domain representation of the first-order LPF [83] can be expressed as

$$LPF = \frac{\omega_c}{s + \omega_c} \tag{2.13}$$

where ω_c is the cut-off frequency of the LPF. The generalized expression for the notch filters can be represented as

$$NF_n = \frac{s^2 + (n\omega_g)^2}{s^2 + 2n\zeta\omega_g s + (n\omega_g)^2} \tag{2.14}$$

where ω_g is the fundamental frequency of the grid.

To extract the information of the amplitude and phase of the grid voltage, the $v_d(t)$ and $v_q(t)$ is passed through the notch filters and LPF blocks. Further, to minimize the error in phase angle detection $V_1^+\varepsilon$ is fed to the LF block (PID controller) for further filtering, so that the phase information can be extracted exactly. The rated grid frequency ω_g is then added to the LF output to minimize the control effort at the beginning of the lock-on operation to the phase angle of the grid [10]. Then, the estimated frequency ω_g^e is integrated to find the phase angle θ_g^e.

In the light of the above analysis, the signals coming out from the PD block (Figure 2.2) can be expressed in s-domain as

$$\begin{aligned} v_d^e(s) &= \frac{\omega_c}{s + \omega_c}\frac{s^2 + (n\omega_g)^2}{s^2 + 2n\zeta\omega_g s + (n\omega_g)^2}\left(V_1^+ + \tilde{v}_d(s)\right) \\ v_q^e(s) &= \frac{\omega_c}{s + \omega_c}\frac{s^2 + (n\omega_g)^2}{s^2 + 2n\zeta\omega_g s + (n\omega_g)^2}\left(V_1^+\varepsilon(s) + \tilde{v}_q(s)\right). \end{aligned} \tag{2.15}$$

In this work, a PID type loop filter is proposed and implemented. The advantage of such modification is that the sluggish response of the system due to LPF and notch filters can be mitigated by carefully choosing the value of k_p, k_i and k_d while not affecting the filtering capability of the PLL system.

2.3 Parameter selection procedure

The choice of different parameters depend upon two critical performance objectives, one is transient response and another one is disturbance rejection capability. The high bandwidth of the control loop enhances the dynamic performance but at the same time, it affects the disturbance rejection capability. Therefore, the cut-off frequency of the LPF and the three gains for the PID type loop filter have to be chosen carefully considering this trade-off. The notch frequency selection is quite straight forward and depends on the nominal grid frequency. The cut-off frequency (ω_c) for the LPF is chosen as 50 Hz in *dq*-domain, which corresponds to the nominal grid frequency in time domain. The choice of cut-off frequency of the LPF is chosen using the small signal analysis. Since, the lowest possible disturbance signal has the frequency twice the nominal grid frequency in *dq*- domain, thus half of its is taken as the cutoff frequency for the LPF. The magnitude response of the three cascaded filters block is represented in Figure 2.5.

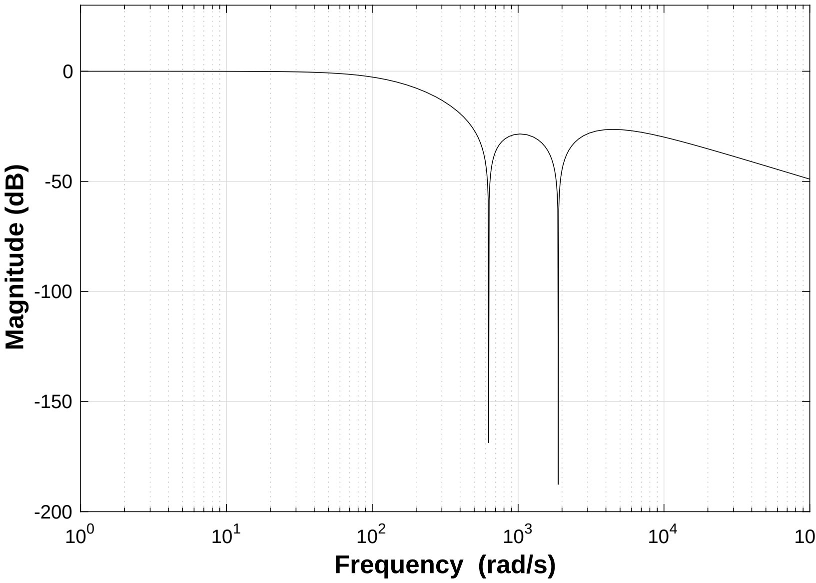

Figure 2.5: Magnitude response of the three cascaded filter blocks

The order of the plant together with the PID type loop filter, two second-order notch filters, and one first-order LPF is seven, which is very high. Therefore, calculating the PID parameters is not straight forward. Hence, the parameters for the PID type loop filter has been chosen initially by

Ziegler-Nichols tuning method [84, 85]. Afterwards, detailed experimentation has been done to find the suitable gains for the PID type loop filter, so that a balance between disturbance rejection and dynamic performance for the proposed PLL can be maintained.

A forward path gain of 326.3 gives a sustained oscillating output for the small-signal model (Figure 2.6). Therefore, according to the Ziegler-Nichols tuning rule, the value of k_u = 326.3, and the proportional gain k_p=0.6k_u, which translates into k_p= 196 (approximately). The time period for the oscillating waveform is t_u=0.04 sec approximately. Therefore, the integral time constant T_i=0.5t_u sec, which translates into the integral time constant T_i= 0.02 sec. and the derivative time constant T_d=0.125t_u sec., hence T_d= 0.005 sec. If the PID type loop filter is transformed from the ideal to parallel form, then the value of integral gain k_i and derivative gain k_d will be 9800 and 0.98, respectively. Finally, a proportional gain of 212, an integral gain of 7730 and a derivative gain of 1.4 have been chosen after trial runs, which meets the desired performance criteria for the system.

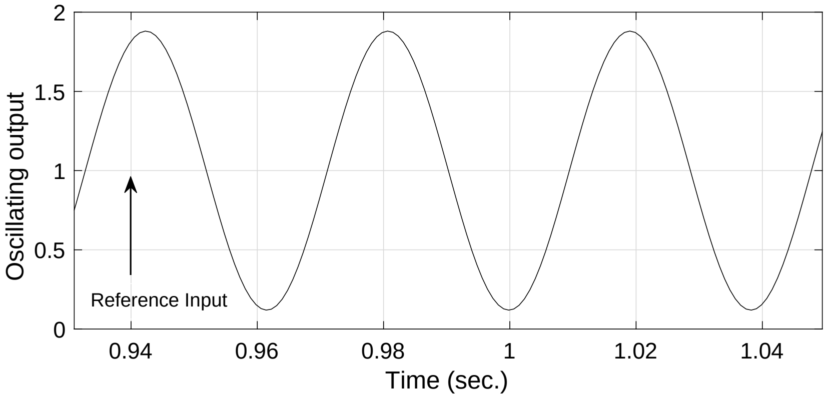

Figure 2.6: Oscillating output of the system with forward path gain of 326.3

2.4 Proposed PLL performance under different scenario

The proposed PLL configuration is compared with the LPF-based SRF-PLL and MRF-PLL under different emulated grid abnormalities, like a step change in frequency, sudden phase jump and input voltage with injected harmonics. The design of the LPF and the PI controller for both of the PLLs (LPF-based and MRF) is done as per the technique presented in [19]. The results under different emulated grid disturbances are shown in Figures 2.7, 2.8, 2.9 and 2.10 respectively. The algorithms are implemented on a digital signal controller (DSC) -TMS320F28335. The main clock frequency of the DSC is 150 MHz. The sampling frequency of 5 kHz is used here for executing the algorithms.

2.4.1 Step change in frequency of emulated grid voltage

The response of three different techniques under a frequency step change of 10 Hz is recorded and shown in Figure 2.7. For observing the waveform, a digital to analogue converter LTC2645 (PWM-DAC) has been used. A step change in the frequency of the test signal from 50 Hz to 60 Hz has been applied (Figure 2.7). It is observed from Figure 2.7(c), that the maximum frequency deviation for the proposed-PLL is very close to the MRF-PLL (Figure 2.7(b)). It is also observed from Figure 2.7, that the settling time (error within 2%) for the proposed-PLL is close to two cycles, whereas, for LPF-based SRF-PLL, the settling time is three cycles approximately, and for the MRF-PLL it is very close to the response of the proposed-PLL technique. The phase angle and the corresponding emulated grid signals are also shown for the three PLL techniques in Figure 2.7.

2.4.2 60° phase jump of the emulated grid voltage

A sudden phase jump of 60° is applied to the input voltage signal and the performance of various algorithms are shown in Figure 2.8. It can be observed from Figure 2.8 that the maximum deviation in frequency (12 Hz) and phase (20°) is less for the LPF-based technique than the proposed and MRF-PLL technique; however, the settling time is more for LPF-based technique. It can be clearly seen that the response of the proposed method (Figure 2.8(c)) is very close to the MRF-PLL (Figure 2.8(b)) in terms of overshoot and settling time. The maximum deviation in frequency is 19 Hz for both the MRF and the proposed technique, whereas the maximum phase deviation is 25° for the MRF-PLL and 24° for the proposed-PLL.

2.4.3 Responses in the presence of voltage harmonics in emulated grid voltage

The response of the proposed PLL with the presence of injected harmonics in the emulated grid voltage is shown in Figure 2.9(c). The harmonic contents which are added to the fundamental are fifth (10% of fundamental) and seventh (5% of the fundamental). From the frequency response shown in Figure 2.9, it can be observed that LPF-based PLL and MRF-PLL technique have more sustained

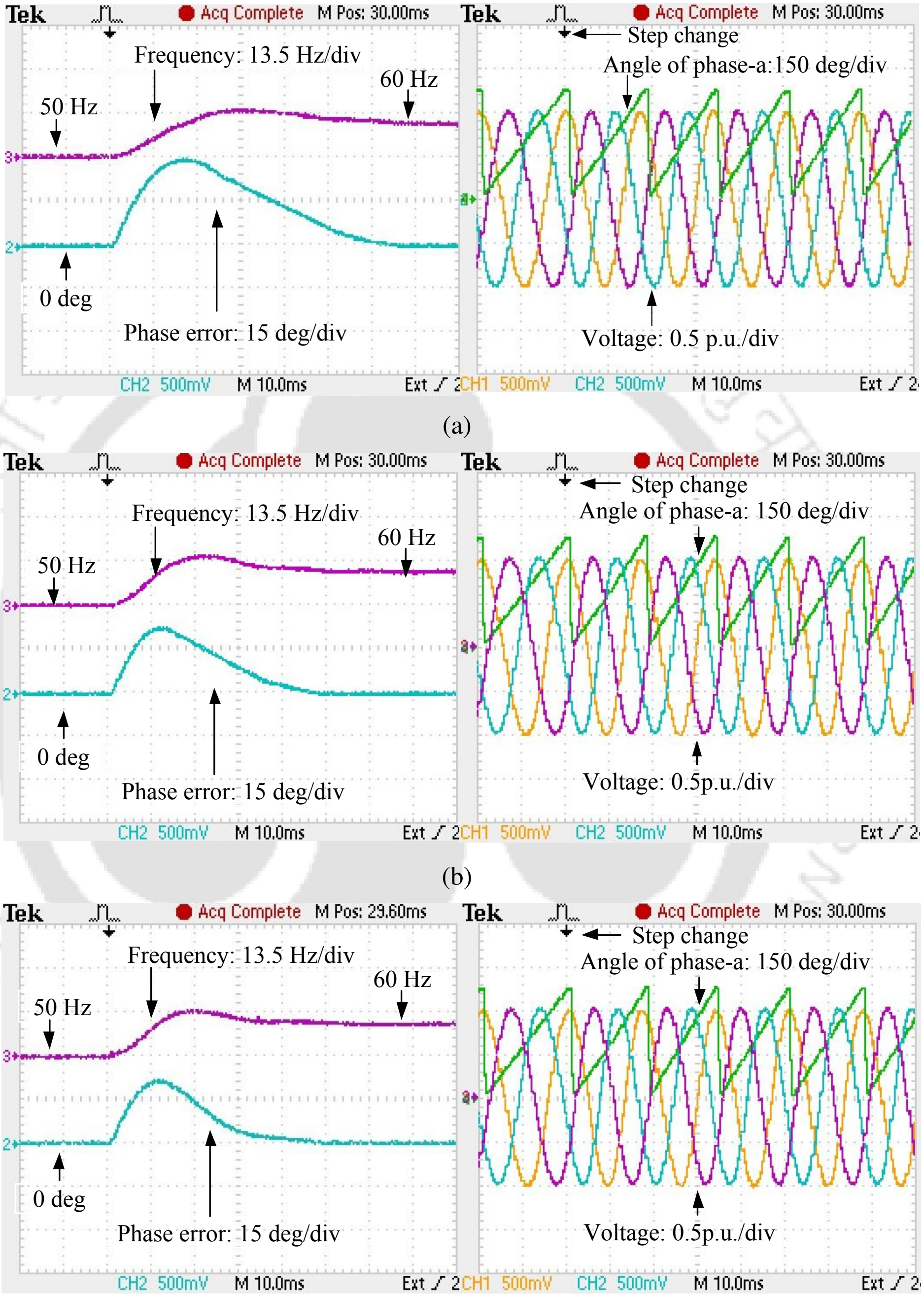

(a)

(b)

(c)

Figure 2.7: Frequency and phase response under step change in frequency of 10 *Hz*; (a) LPF-based SRF-PLL. (b) MRF-PLL. (c) Proposed PLL.

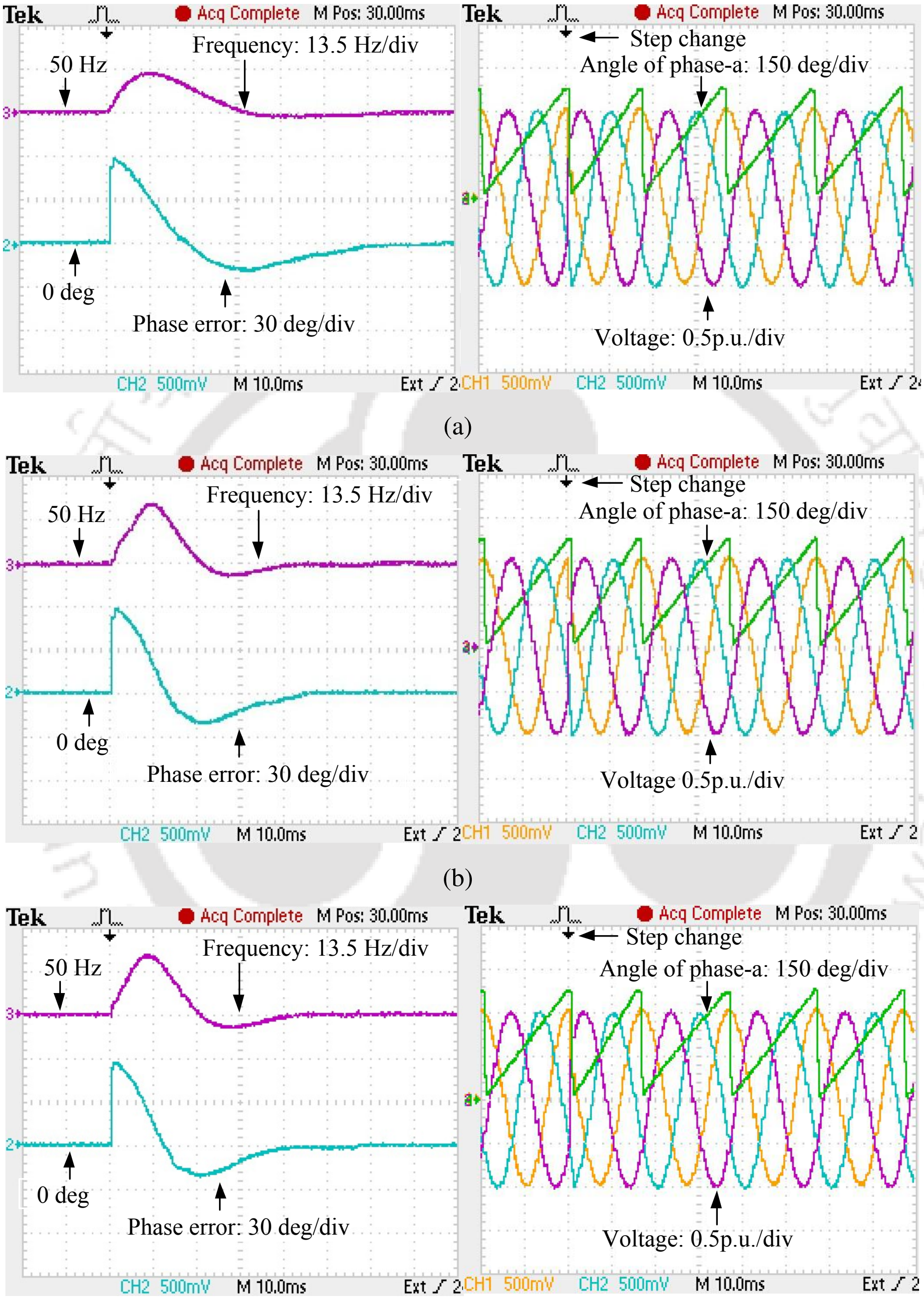

(a)

(b)

(c)

Figure 2.8: Frequency and phase response under step change of 60° in phase (a) LPF-based SRF-PLL. (b) MRF-PLL. (c) Proposed PLL.

oscillation (Figure 2.9(a) and 2.9(b)), whereas the proposed-PLL (Figure 2.9(c)) has no oscillation in its frequency and phase responses. The steady-state peak to peak frequency deviation is 0.8 Hz for the LPF-based PLL technique and 0.7 Hz for the MRF-PLL technique, whereas the phase deviation is observed as 0.4° for the LPF-based PLL technique and 0.3° for the MRF-PLL technique.

2.4.4 Responses under unbalance condition

The unbalance condition is emulated by reducing the Phase-b voltage to 70% of Phase-a voltage, and Phase-c kept as 80% of the Phase-a voltage while keeping phase-a same as before (Figure 2.10). From Figure 2.10 it can be seen that under such condition of emulated voltages, the proposed technique is giving the same response as the MRF-PLL technique. Both the techniques are immune to the unbalance because of the cancellation of the second harmonic effectively, whereas LPF-based SRF-PLL has sustained steady-state oscillation in both the frequency and phase responses (Figure 2.10(a)). The steady-state peak to peak frequency and phase deviations are 1.2 Hz and 1° respectively for the LPF-based technique. The quantitative performance analysis of the three PLL under different abnormalities is shown in (Table-2.1).

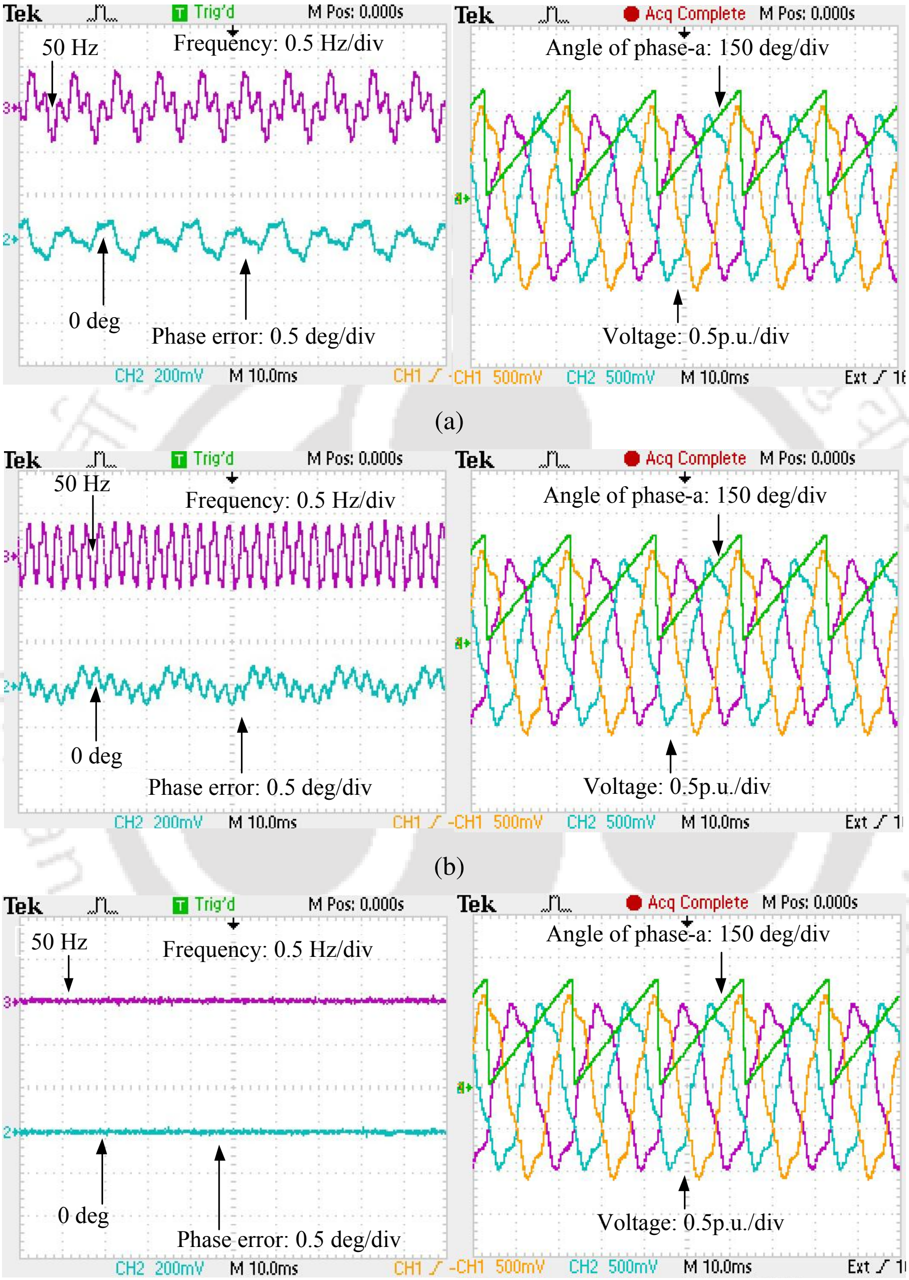

(a)

(b)

(c)

Figure 2.9: Frequency and phase response under harmonic distortion (a) LPF-based SRF-PLL. (b) MRF-PLL. (c) Proposed PLL.

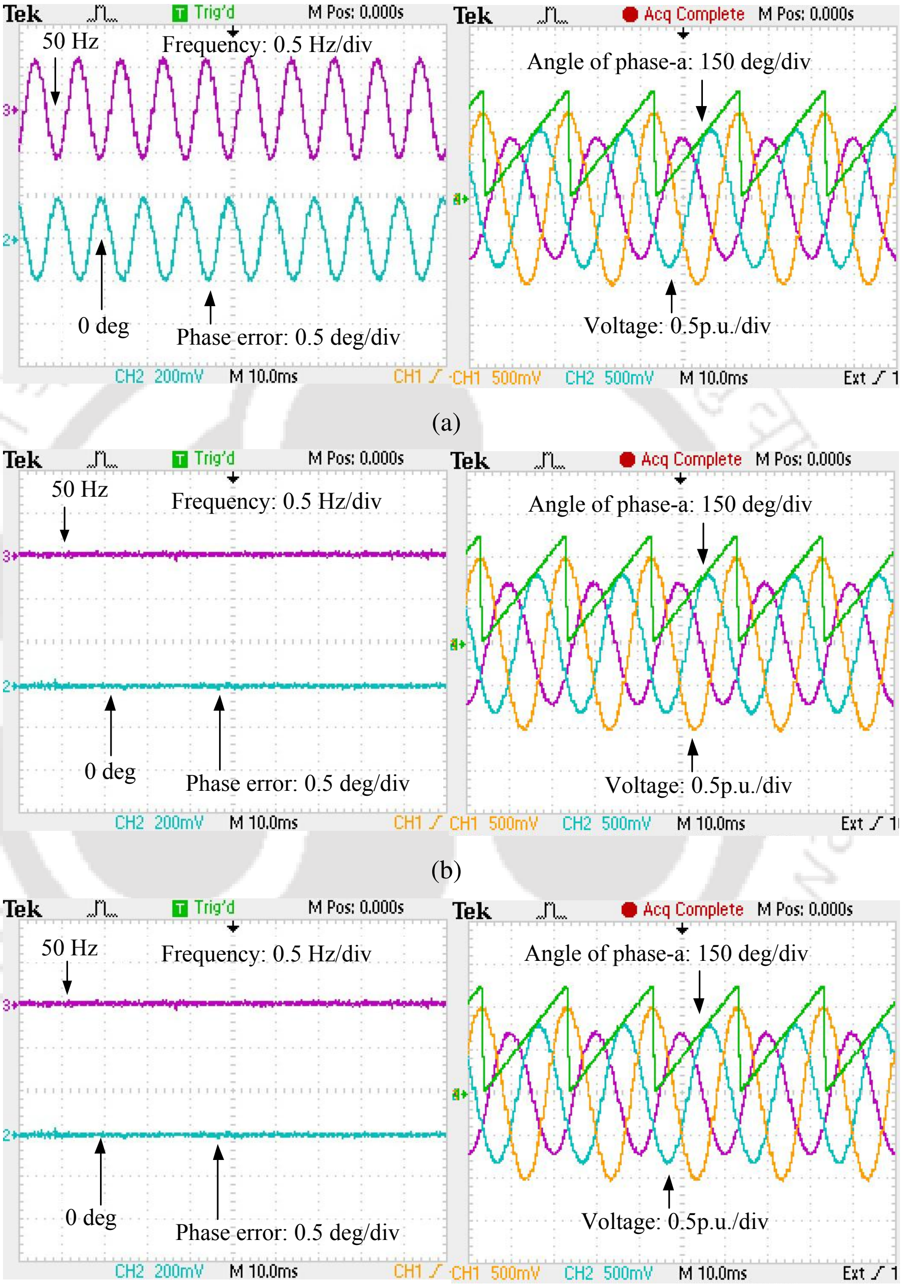

(a)

(b)

(c)

Figure 2.10: Frequency and phase response under unbalance (a) LPF-based SRF-PLL. (b) MRF-PLL. (c) Proposed PLL.

Table 2.1: Comparison of experimental results for different PLLs

Test Condition	LPF-based SRF-PLL	MRF-PLL	Proposed -PLL
Frequency jump (10 Hz):			
Settling time (within 2%):	3 cycles (approx)	2 cycles (approx)	2 cycles (approx)
Max frequency deviation:	3 Hz (approx)	3.5 Hz (approx)	3.3 Hz (approx)
Max Phase deviation:	29° (approx)	22° (approx)	22° (approx)
Phase jump (60°):			
Settling time (within 2%):	3 cycles (approx)	2 cycles (approx)	2 cycles (approx)
Max frequency deviation:	12 Hz (approx)	19 Hz (approx)	19 Hz (approx)
Max Phase deviation:	20° (approx)	25° (approx)	24° (approx)
Harmonic injection:			
Steady state peak-peak frequency deviation:	0.8 Hz (approx)	0.7 Hz (approx)	0 Hz (approx)
Max Phase deviation:	0.4° (approx)	0.3° (approx)	0° (approx)
Imbalance Condition:			
Steady state peak-peak frequency deviation:	1.2 Hz (approx)	0 Hz (approx)	0 Hz (approx)
Max Phase deviation:	1° (approx)	0° (approx)	0° (approx)
Complexity:			
Add/subtract:	12	24	13
Multi/div/scale:	19	41	21
Integration/differentiation :	2	2	3
Trigonometric :	2	8	2

2.5 Summary

A PLL technique is proposed here, which has been used for estimating the phase and frequency of the grid voltage. The proposed PLL plays a critical role in the *dq* transformation for implementing the grid side converter (GSC) control. The proposed technique uses a PID type loop filter along with two in-loop notch filters and a low pass filter (LPF). The in-loop filters nullify the effect of dominant lower order harmonics, and the dynamic performance of the proposed technique is improved by implementing a PID type loop filter. A comparative analysis of the proposed method with LPF-based SRF-PLL and MRF-PLL has been done for various disturbances such as step change in frequency, phase jump of grid voltage, and presence of harmonics and unbalance in the grid voltage on a digital signal controller (DSC) TMS320F28335. From the comparative analysis, it is observed that the proposed method exhibits similar comparable performance to the MRF-PLL technique and superior performance than the LPF-based SRF-PLL technique. The proposed technique is found to be computationally less complicated as compared to the MRF-PLL and other enhanced filter based PLL techniques. It is observed from the experimental results that the proposed-PLL can provide a reasonable estimate of the grid phase angle in real-time, and hence, it is suitable for close loop control of GSC.

3

Development of an adaptive voltage and current control strategies for the three-phase GSC/SSC

Contents

3.1 Introduction

In this chapter, a new control strategy to control the grid side converter (GSC) is proposed. The proposed control strategy is an extended state observer (ESO) based adaptive control, consists of two cascaded control loops. The adaptive-MIMO controller is employed in the inner control loop, which is used to regulate the active and reactive component of the grid currents. The outer-loop consists of an adaptive controller augmented with an ESO to regulate the DC bus voltage. The designed adaptive current controller neither requires a priori information about the system parameters, nor it requires any expensive algorithm to estimate the plant parameters accurately like self-tuning (ST) regulators. It only requires the structure of the model. The uncertainties in the plant model are modelling uncertainty, i.e., uncertainty associated with the structure of the model, and the parametric uncertainty, i.e., uncertainty associated with the parameters of the model. This work attempt to address the parametric uncertainty associated with the plant model, assuming the exact structure of the plant model is known to the designer. Utilizing the Lyapunov stability criteria, a systematic design procedure is provided to derive the current controller. In addition to that, stability analysis is also provided for the designed current controller.

The DC link voltage control strategy is based on the extended state observer (ESO), which includes external load disturbance as an extended state of the system. The design of the voltage controller is similar to the current controller with slight modification. Here, ESO is used to contemplates the disturbances as a new state of the system. The disturbances are like parametric uncertainty, unmodeled dynamics, and load variation. Due to such an encouraging attribute, ESO is capable of estimating both the common disturbance and the system states [86–88]. The performance of the ESO based voltage controller is found to be quite encouraging, and a finite time convergence of the control variable is achieved. For its implementations, it does require the value of the DC link capacitor. The proposed voltage and current control algorithms are implemented on a hardware prototype to check their performances in real-time. The hardware consists of a 150 MHz, TMS320F28335 digital signal controller (DSC) kit along with a Semikron make three-phase, four-leg insulated gate bipolar transistor (IGBT) based pulse width modulated (PWM) converter. The proposed current controller is

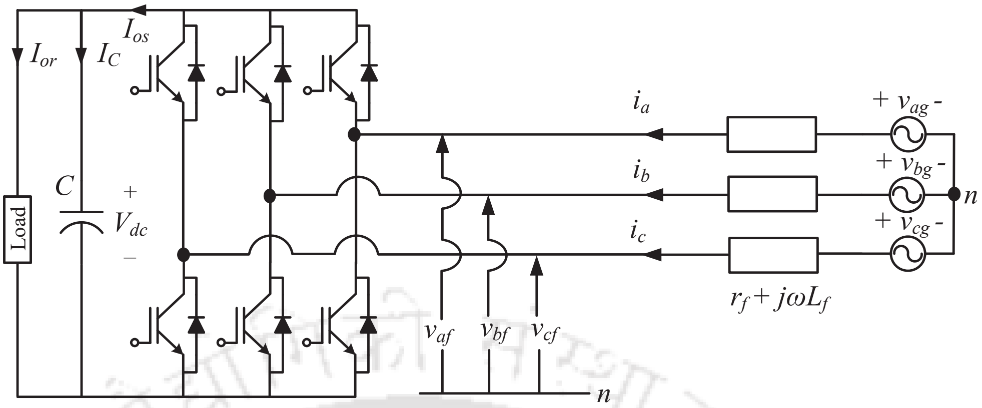

Figure 3.1: Schematic representation of the grid side converter (GSC)

formulated in dq-domain, and control pulses are generated by means of SINPWM to drive the power converter.

3.2 Dynamic Model of GSC/SSC

This section describes the structure and the model used for the design of controllers for GSC. The schematic diagram of the converter system is represented in Figure 3.1. It consists of six IGBT power electronic switches and the AC side of the converter is connected to the three-phase grid by means of a grid filter. The grid filter comprises of an inductor (L_f) and a small parasitic (r_f) resistance associated with it. One electrolytic capacitor (C) is placed in the DC side of the converter to filter out the ripples in the DC link voltage, and it also acts as a temporary energy storage element. A variable resistive load is connected parallel to the DC link capacitor to emulate the effect of a rotor side converter in wind energy conversion system (WECS).

A balanced three-phase (abc) alternating variables of a three-phase system can be transformed into two-phase ($\alpha\beta$) alternating variables using Clarke's transformation. These two-phase alternating variables can be represented as stationary variables (dq) using a synchronously rotating reference frame (SRF) by applying Park's transformation. The speed of the reference frame is the same as the speed of the grid angular frequency of ω_g. Hence, the Clarke's along with the Park's transformation has been used to transform the three-phase sinusoidal quantity into stationary DC quantity, thus simplifying the control problem into a set-point tracking problem. The accuracy of Park's transformation depends upon the accuracy of the estimated grid phase angle θ_g, and grid frequency ω_g. Therefore to estimate the grid phase and frequency, the proposed phase-locked-loop (PLL) technique discussed in Chapter 2 is used. It can be observed that under phase-locked condition, the algorithm estimates true grid phase angle $\theta_g^e = \theta_g$ and true grid frequency $\omega_g^e = \omega_g$.

The three-phase dynamical equation [6] of the GSC is represented as

$$\begin{aligned} v_{ag} &= r_f i_a + L_f \frac{di_a}{dt} + v_{af} \\ v_{bg} &= r_f i_b + L_f \frac{di_b}{dt} + v_{bf} \\ v_{cg} &= r_f i_c + L_f \frac{di_c}{dt} + v_{cf} \end{aligned} \tag{3.1}$$

where v_{ag}, v_{bg} and v_{cg} are the three-phase grid voltages, v_{af}, v_{bf} and v_{cf} are the converter outputs and i_a, i_b and i_c are the three-phase grid currents.

Applying Clarke's transformation to (3.1) the dynamic equation of the GSC in $\alpha\beta$-domain can be written as

$$\begin{aligned} v_{\alpha g} &= r_f i_\alpha + L_f \frac{di_\alpha}{dt} + v_{\alpha f} \\ v_{\beta g} &= r_f i_\beta + L_f \frac{di_\beta}{dt} + v_{\beta f} \end{aligned} \tag{3.2}$$

where $v_{\alpha g}$ and $v_{\beta g}$ are the grid voltages in $\alpha\beta$-domain, $v_{\alpha f}$ and $v_{\beta f}$ are the converter outputs in $\alpha\beta$-domain and i_α and i_β are the grid currents in $\alpha\beta$ domain.

Applying Park's transformation to (3.2) the dynamic equation of the GSC in dq-domain can be written as

$$\begin{aligned} v_{dg} &= r_f i_d + L_f \frac{di_d}{dt} + v_{df} - \omega_g L_f i_q \\ v_{qg} &= r_f i_q + L_f \frac{di_q}{dt} + v_{qf} + \omega_g L_f i_d \end{aligned} \tag{3.3}$$

The dynamic equation (3.3) can be rewritten as

$$\begin{aligned} L_f \frac{d}{dt}(i_d) &= -r_f i_d + \omega_g L_f i_q + v_{dg} - u_d \frac{V_{dc}}{2} \\ L_f \frac{d}{dt}\left(i_q\right) &= -r_f i_q - \omega_g L_f i_d + v_{qg} - u_q \frac{V_{dc}}{2} \end{aligned} \tag{3.4}$$

where $u_d = 2v_{df}/V_{dc}$, $u_q = 2v_{qf}/V_{dc}$ are the modulation index or control input to the converter switches. To restrict the control input within the linear modulation range, the maximum value of $\|u_{dq}\|$ is chosen as '1'. In dq domain, the grid side voltages are represented by v_{dg} and v_{qg} and the grid currents are represented as i_d and i_q.

The DC bus voltage dynamics of the GSC is represented as

$$C\frac{d}{dt}(V_{dc}) = I_{os} - I_{or} \tag{3.5}$$

where the DC bus voltage is represented as V_{dc} and DC load current is represented as I_{or} and the total DC side current is represented as I_{os}.

The phase angle information of the grid is estimated by the proposed PLL discussed in the previous chapter (Chapter 2). Since the d-axis of the rotating reference frame is aligned with the grid voltage vector (Figure 3.2), the value of $v_{dg} = |\vec{v}_g|$ and the value of $v_{qg} = 0$. Using this information, (3.4) can be rewritten as

$$\begin{aligned} \frac{d}{dt}(i_d) &= -\frac{r_f}{L_f}i_d + \omega_g i_q + \frac{v_{dg}}{L_f} - u_d\frac{V_{dc}}{2L_f} \\ \frac{d}{dt}\left(i_q\right) &= -\frac{r_f}{L_f}i_q - \omega_g i_d - u_q\frac{V_{dc}}{2L_f}. \end{aligned} \tag{3.6}$$

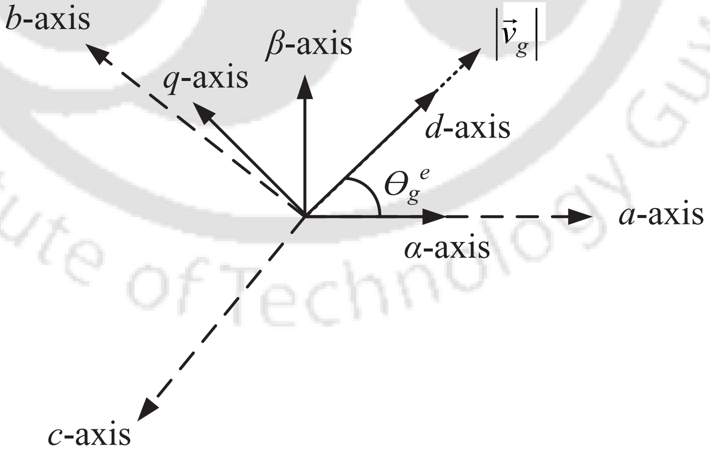

Figure 3.2: Reference frame and the voltage vector position

The active and reactive power equation for the converter circuit can be represented as

$$\begin{aligned} P_g &= \frac{3}{2}v_{dg}i_d \\ Q_g &= \frac{3}{2}v_{dg}i_q \end{aligned} \tag{3.7}$$

From (3.7), it is observed that active and reactive power can be controlled by controlling i_d and i_q, respectively. Neglecting the converter switching and parasitic resistance of the filter, the power balance equation can be written as

$$\begin{aligned} V_{dc}I_{os} &= \frac{3}{2}v_{dg}i_d \\ v_{dg} &= u_d\frac{V_{dc}}{2} \end{aligned} \tag{3.8}$$

From (3.8), the expression for the total DC bus current (I_{os}) can be written as: $I_{os} = 3/4(u_d i_d)$. Plugging the value of I_{os} into (3.5), the DC bus dynamics can be represented as

$$C\frac{d}{dt}(V_{dc}) = \frac{3}{4}u_d i_d - I_{or} \tag{3.9}$$

Replacing u_d from (3.9), the expression for the DC bus dynamics can further be represented as

$$C\frac{d}{dt}(V_{dc}) = \frac{3}{2}\frac{v_{dg}}{V_{dc}}i_d - I_{or} = \frac{1}{V_{dc}}\left(\frac{3}{2}v_{dg}i_d - V_{dc}I_{or}\right) = \frac{1}{V_{dc}}\left(P_g - P_l\right) \tag{3.10}$$

where $P_l = V_{dc}I_{or}$ is called the load power.

The above mathematical model of the system is designed based on various assumptions such as, neglecting the switching losses, neglecting the parasitic resistance of grid filter, uncertainty in the value of grid filter inductance, and some other unmodeled dynamics. This results into the parametric uncertainty of the model and hence motivates to use the adaptive controller to control GSC.

3.3 Formulation of the controllers

GSC control consists of two cascade control loops (Figure 3.3). The outer loop consists of a voltage controller which generates the reference input current i_d^* for the inner loop (d-axis) current controller, which is required for maintaining a desired DC-link voltage. The reference i_q^* (q-axis) current decides the desired reactive power exchanged with the grid. The designed voltage and current controllers need to be effective towards the parametric uncertainty and external load disturbances. To achieve the above objectives, the current controller is designed to handle parametric uncertainties, whereas the voltage controller is designed to mitigate the effect of external load disturbances. For implementing the current control, an adaptive-MIMO controller is designed to ensure stability in the sense of Lyapunov and guarantees finite time set-point tracking. For implementing the voltage controller, an adaptive controller of a similar structure is used along with an extended state observer (ESO). The ESO estimates the load disturbances and the information is fed into the voltage control architecture. This significantly improves the dynamic performance of the proposed voltage control strategy. The schematic of the implemented controllers is shown in Figure 3.3, and the details about the controllers are presented in subsequent subsections.

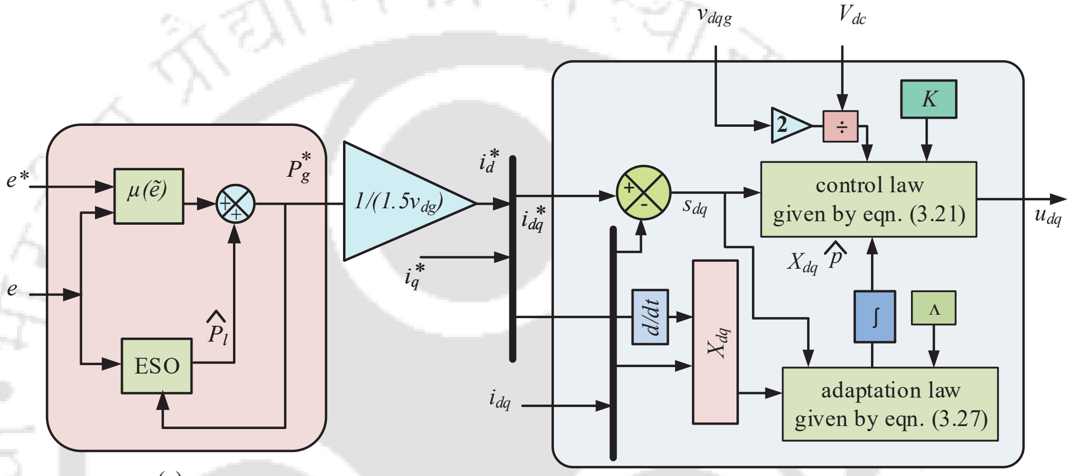

(a)

(b)

Figure 3.3: Schematic diagram of the proposed controller: (a) Schematic of the proposed voltage controller; (b) Schematic of the proposed current controller

3.3.1 Formulation of the proposed current controller

The current dynamics of grid side converter is given in (3.6), and the control task is to track the reference currents i.e., $i_d \rightarrow i_d^*$ and $i_q \rightarrow i_q^*$. A new variable s_{dq} is defined as

$$s_{dq} = \begin{bmatrix} s_d \\ s_q \end{bmatrix} = \begin{bmatrix} i_d^* - i_d \\ i_q^* - i_q \end{bmatrix} = \begin{bmatrix} \tilde{i}_d \\ \tilde{i}_q \end{bmatrix}. \tag{3.11}$$

From (3.11), it can be seen that s_{dq} is the current tracking errors in dq-domain.

The first derivative of s_{dq} contains the final control input u_{dq}, where $u_{dq} = \begin{bmatrix} u_d & u_q \end{bmatrix}^T$. If $s_{dq} \rightarrow 0$ $\Rightarrow \tilde{i}_{dq} \rightarrow 0$, where, $\tilde{i}_{dq} = \begin{bmatrix} \tilde{i}_d & \tilde{i}_q \end{bmatrix}^T$. From (3.6), the expression for u_d and u_q can be written in companion form as

$$\begin{aligned} u_d &= -\frac{2L_f}{V_{dc}}\frac{d}{dt}\left(i_d\right) - \frac{2r_f}{V_{dc}}i_d + \frac{2\omega_g L_f}{V_{dc}}i_q + \frac{2v_{dg}}{V_{dc}} \\ u_q &= -\frac{2L_f}{V_{dc}}\frac{d}{dt}\left(i_q\right) - \frac{2r_f}{V_{dc}}i_q - \frac{2\omega_g L_f}{V_{dc}}i_d. \end{aligned} \tag{3.12}$$

The objective here is to find a suitable u_{dq} which makes the tracking errors $s_{dq} = 0$ within finite time, under the parametric uncertainty of grid filter.

The Lyapunov function subjected to the dynamics (3.12) is chosen as

$$V = \frac{1}{2}s_{dq}^T P s_{dq} \tag{3.13}$$

where, P is a diagonal matrix and defined as $\frac{2L_f}{V_{dc}}I$ and I is the identity matrix.

The time derivative of the Lyapunov function is

$$\dot{V} = s_{dq}^T P \dot{s}_{dq} \tag{3.14}$$

where, $P\dot{s}_{dq}$ can be written as

$$P\dot{s}_{dq} = \begin{bmatrix} \frac{2L_f}{V_{dc}} & 0 \\ 0 & \frac{2L_f}{V_{dc}} \end{bmatrix} \begin{bmatrix} \dot{s}_d \\ \dot{s}_q \end{bmatrix} \tag{3.15}$$

Plugging (3.6), into (3.15), the expression (3.15) can further be elaborated as

$$\frac{2L_f}{V_{dc}}\dot{s}_{dq} = \frac{2L_f}{V_{dc}}\frac{di_{dq}^*}{dt} + \frac{2r_f}{V_{dc}}i_{dq} + \frac{2\omega_g L_f}{V_{dc}}\begin{bmatrix} 0 & -1 \\ 1 & 0 \end{bmatrix}\begin{bmatrix} i_d \\ i_q \end{bmatrix} - \frac{2v_{dqg}}{V_{dc}} + u_{dq} \tag{3.16}$$

where, $\frac{di_{dq}^*}{dt} = \begin{bmatrix} \frac{di_d^*}{dt} & \frac{di_q^*}{dt} \end{bmatrix}^T$, $i_{dq} = \begin{bmatrix} i_d & i_q \end{bmatrix}^T$, $v_{dqg} = \begin{bmatrix} v_{dg} & 0 \end{bmatrix}^T$.

From the left hand side of the (3.16), it can be observed that except the control input u_{dq} and the constant term $2v_{dqg}/V_{dc}$, the other terms can be written as a product of unknown constant with the known states, and can be represented as

$$\frac{2L_f}{V_{dc}}\dot{s}_{dq} = u_{dq} - X_{dq}p - \frac{2v_{dqg}}{V_{dc}} \tag{3.17}$$

where, $p = \begin{bmatrix} \frac{2L_f}{V_{dc}} & \frac{2r_f}{V_{dc}} & \frac{2\omega_g L_f}{V_{dc}} \end{bmatrix}^T$ is the vector of unknown constants and the state is given by $X_{dq} =$

$\begin{bmatrix} X_d & X_q \end{bmatrix}^T$, where $X_d = \begin{bmatrix} -\frac{di_d^*}{dt} & -i_d & i_q \end{bmatrix}$, $X_q = \begin{bmatrix} -\frac{di_q^*}{dt} & -i_q & -i_d \end{bmatrix}$, respectively.

For designing a stable controller in the sense of Lyapunov, $\dot{V}$ needs to be negative semidefinite. To make $\dot{V} \leq 0$, the control law given by (3.18) may be used

$$u_{dq} = X_{dq}p - Ks_{dq} + \frac{2v_{dqg}}{V_{dc}} \tag{3.18}$$

where K is the gain matrix and given by

$$K = \begin{bmatrix} K_{11} & 0 \\ 0 & K_{22} \end{bmatrix}$$

Plugging the value of u_{dq}, from (3.18) into (3.17), the expression for $P\dot{s}_{dq}$ can be obtained as

$$P\dot{s}_{dq} = X_{dq}p - Ks_{dq} + \frac{2v_{dqg}}{V_{dc}} - X_{dq}p - \frac{2v_{dqg}}{V_{dc}} = -Ks_{dq} \tag{3.19}$$

Replacing (3.19), into (3.14), $\dot{V}$ can be expressed as

$$\dot{V} = -s_{dq}^T Ks_{dq} \leq 0. \tag{3.20}$$

However, considering the parametric uncertainties of the grid filter, the above control law given in (3.18) will not serve the purpose. Furthermore, the above control law (3.18) requires the exact value of the parameters, but for designing an adaptive controller only an estimate of p, i.e., $\hat{p}$ is available. Taking this into consideration, the control law given in (3.18) is modified as

$$u_{dq} = X_{dq}\hat{p} - Ks_{dq} + \frac{2v_{dqg}}{V_{dc}} \tag{3.21}$$

Plugging (3.21) into (3.17), the expression for $P\dot{s}_{dq}$ and $\dot{V}$ is again calculated as

$$P\dot{s}_{dq} = X_{dq}\hat{p} - Ks_{dq} + \frac{2v_{dqg}}{V_{dc}} - X_{dq}p - \frac{2v_{dqg}}{V_{dc}} = -Ks_{dq} + X_{dq}\left(\hat{p} - p\right) = -Ks_{dq} + X_{dq}\tilde{p} \tag{3.22}$$

$$\dot{V} = s_{dq}^T P\dot{s}_{dq} = -s_{dq}^T Ks_{dq} + s_{dq}^T X_{dq}\tilde{p} \tag{3.23}$$

where, $\tilde{p} = \hat{p} - p$ is called the parameter estimation error. In (3.23), the second term $\left(s_{dq}X_{dq}\tilde{p}\right)$ is unknown, hence, $\dot{V}$ is not guaranteed to be negative semidefinite.

For cancellation of the second term in (3.23), a quadratic term in parameter estimation error is added with the original Lyapunov function (3.13). The new Lyapunov function is chosen as

$$V = \frac{1}{2}s_{dq}^T P s_{dq} + \frac{1}{2}\tilde{p}^T \Lambda^{-1} \tilde{p} \tag{3.24}$$

where, Λ^{-1} is considered as positive definite diagonal matrix here. The time derivative of the new Lyapunov function is calculated as

$$\dot{V} = -s_{dq}^T K s_{dq} + s_{dq}^T X_{dq} \tilde{p} + \dot{\hat{p}}^T \Lambda^{-1} \tilde{p} \tag{3.25}$$

For a stable controller, the equation given by (3.26) should satisfy which ensures that $\dot{V}$ given by (3.25) is negative semidefinite.

$$s_{dq}^T X_{dq} \tilde{p} \; + \; \dot{\hat{p}}^T \Lambda^{-1} \tilde{p} = 0 \tag{3.26}$$

From (3.26), the parameter adaptation law (3.27) is obtained as

$$\dot{\hat{p}} = -\Lambda X_{dq}^T s_{dq} \tag{3.27}$$

Thus, an adaptive stabilizing controller is designed by using the control law defined by (3.21) and adaptation law defined by (3.27). The schematic diagram of the implemented current controller is shown in Figure 3.3(b). To implement the current controller, the control law given by (3.21) is used, and the parameter adaptation law given by (3.27) is used. The parameter adaptation law feeds the control law to fulfil the desired control objective.

3.3.1.1 Stability analysis of current controller

According to Barbalat's Lemma, if a function $f(t)$ is differentiable and has a finite limit as $t \to \infty$, and if $\dot{f}(t)$ is uniformly continuous, then $\dot{f}(t) \to 0$ as $t \to \infty$ [89].

From the finite difference theorem, it can be seen that if the derivative $\dot{f}(t)$ of a differentiable function $f(t)$ is bounded then the $f(t)$ is uniformly continuous. Considering this fact, the corollary follows from Barbalat's Lemma can be described as: If $f(t)$ is differentiable and has a finite limit as

$t \to \infty$, and $\ddot{f}(t)$ exists and bounded, then $\dot{f}(t) \to 0$ as $t \to \infty$ [89].

Now to show global stability, X_{dq} and $\hat{p}$ should remain bounded, and for the convergence of tracking error (s_{dq}), it is sufficient to show $\dot{V} \to 0$ as time $t \to \infty$ in order to show $s_{dq} \to 0$ as time $t \to \infty$.

The chosen Lyapunov function (V) given by (3.24) is positive semidefinite, hence V is lower bounded. From (3.25) and (3.26) it can be observed that $\dot{V}$ is negative semidefinite, which implies that s_{dq} and $\tilde{p}$ remain bounded ($s_{dq}, \tilde{p} \in L^{\infty}$). Moreover, this in turn implies that X_{dq} and $\hat{p}$ are also bounded ($X_{dq}, \hat{p} \in L^{\infty}$).

The expression for $\ddot{V}$ is given as

$$\ddot{V} = -2 s_{dq}^{T} K \dot{s}_{dq} \tag{3.28}$$

Now, it is required to show $\ddot{V}$ is bounded to show $\dot{V}$ is uniformly continuous. For that, $\dot{s}_{dq}$ is required to be bounded as it has been already shown that s_{dq} is bounded. Now, plugging u_{dq} from (3.21) into (3.17), the expression for the error dynamics can be expressed as

$$\frac{2L_f}{V_{dc}} \dot{s}_{dq} = X_{dq}\tilde{p} - K s_{dq} \tag{3.29}$$

Everything on the right hand side of (3.29) is bounded and the term $2L_f/V_{dc}$ is also finite which implies that $\dot{s}_{dq}$ is bounded. Therefore, $\ddot{V}$ is bounded and since $\ddot{V}$ is bounded, $\dot{V}$ is uniformly continuous. Thus, the corollary follows from the Barbalat's Lemma indicates that $\dot{V} \to 0$ as time $t \to \infty$ which implies that the error $s_{dq} \to 0$ as time $t \to \infty$. Hence, the proposed controller force the tracking error to zero ($s_{dq} \to 0$ as time $t \to \infty$) and at the same time the global stability is assured by the proposed controller as X_{dq} and $\hat{p}$ remain bounded ($X_{dq}, \hat{p} \in L^{\infty}$).

Remark 1: It should be pointed out that this methodology does not estimate the parameters exactly; instead, it produces values that drive the controller for the successful completion of the control task. If the desired trajectory is so enriching, that without the correct estimate, the control objective cannot be achieved then by definition, it will estimate the parameter precisely. Therefore adaptation happens on a need-to-know basis and it is called the sufficient richness [90]. Further, discussion on this is beyond the scope of the present work.

Remark 2: For implementing the control law, the information about the time derivatives of the desired currents i^*_{dq} is required. In steady-state, the derivatives are zero, and during the transient, it will give sudden jumps. For countering this, the time derivatives of desired currents are multiplied by a small gain at the order of 10^{-3} so that sudden jumps can be limited.

3.3.2 Formulation of the proposed voltage controller

The objective of the voltage controller is to regulate the DC bus voltage at the desired level under the load uncertainties while fulfilling different performance criteria. For regulating the DC bus voltage, an adaptive controller has been designed. While designing the voltage controller, the load connected across the DC bus is modelled as an extended state. The design procedure of the voltage regulator is similar to that of the current controller, as discussed in the previous subsection. The schematic diagram of the voltage controller augmented with the ESO is given in Figure 3.3(a) and the details about the design procedure of the voltage controller and the observer are described below.

A new variable e is defined which is expressed as $e = V^2_{dc}/2$. Using this notation, the DC bus dynamics described by (3.10) is expressed as follows

$$C\dot{e} = P^*_g - P_l(t) \tag{3.30}$$

where, P^*_g is the desired active power exchange between the grid and converter to maintain the DC link voltage. The desired active power is further converted to equivalent d-axis reference current (i^*_d), and is fed to the current controller. The reference current i^*_d is related to the active power reference, by the relation $i^*_d = P^*_g/(1.5v_{dg})$ (Figure 3.3). Here, the load power $P_l(t)$ is assumed as the time dependent disturbance input to the system.

The tracking error is defined as $\tilde{e} = e^* - e$, where, $e^* = V^{*2}_{dc}/2$. For the dynamics described by (3.30), the Lyapunov function is constructed as

$$V_1 = \frac{1}{2}C\tilde{e}^2 + \frac{1}{2}\tilde{C}\gamma^{-1}\tilde{C} \tag{3.31}$$

where, the parameter error $\tilde{C}$ is defined as $\tilde{C} = \hat{C} - C$, and $\frac{1}{2}\tilde{C}\gamma^{-1}\tilde{C}$ is the quadratic term associated with the parameter estimation error, and γ is assumed to be a positive constant. Based upon this, a control law is proposed, which is given as

$$P_g^* = \dot{e}^*\hat{C} + P_l(t) + K_3\tilde{e} \tag{3.32}$$

where K_3 is the scalar gain. The expression for the $\dot{V}_1$ is given as

$$\dot{V}_1 = -K_3\tilde{e}^2 - \tilde{e}\dot{e}^*\tilde{C} + \dot{\hat{C}}\gamma^{-1}\tilde{C} \tag{3.33}$$

Defining the dynamics associated with the estimation of C, as $\dot{\hat{C}} = \gamma\dot{e}^*\tilde{e}$, the derivative of the Lyapunov function can be written as

$$\dot{V}_1 = -K_3\tilde{e}^2 \leq 0 \tag{3.34}$$

It can be shown from Barbalat's Lemma, that the error $\tilde{e} \to 0$ as $t \to \infty$, and $\hat{C}$ and e remain bounded ($\hat{C}, e \in L^\infty$) which ensures stable operation.

The objective of the control law defined by (3.32) is to regulate the DC bus voltage under the load uncertainty $P_l(t)$. Furthermore, the load disturbance input $P_l(t)$ is a time-dependent input to the system, which can be declared as an external disturbance. For precise control of DC bus voltage by the proposed control law (3.32) an accurate estimate of $P_l(t)$ is required. Hence, an ESO is designed to estimate the load disturbance, which models the external load disturbance ($P_l(t)$) as the new state of the system. Using the linear ESO formulation, as given in [52], the dynamics (3.30) can further be represented as

$$\begin{aligned} C\dot{\hat{e}} &= P_g^* - \hat{P}_l(t) + \alpha_1(e - \hat{e}) \\ \dot{\hat{P}}_l(t) &= -\alpha_2(e - \hat{e}) \end{aligned} \tag{3.35}$$

where, α_1 and α_2 has to satisfy the condition of Hurwitz stability, for the polynomial expression given by $\chi^2 + \frac{\alpha_1}{C}\chi + \frac{\alpha_2}{C}$.

The observation error is denoted by $\varepsilon_e = e - \hat{e}$ and $\varepsilon_{P_l} = P_l(t) - \hat{P}_l(t)$, and the error dynamics can be represented as

$$\begin{aligned} C\dot{\varepsilon}_e &= -\alpha_1\varepsilon_e - \varepsilon_{P_l} \\ \dot{\varepsilon}_{P_l} &= \alpha_2\varepsilon_e + h(t) \end{aligned} \tag{3.36}$$

where, $h(t) = \dot{P}_l(t)$ is the rate of change in the load.

From (3.36) the extended state system can be expressed as

$$\dot{\varepsilon} = A\varepsilon + \varphi \tag{3.37}$$

where, $A = \begin{bmatrix} -\frac{\alpha_1}{C} & -\frac{1}{C} \\ \alpha_2 & 0 \end{bmatrix}$, $\varepsilon = \begin{bmatrix} \varepsilon_e & \varepsilon_{P_l} \end{bmatrix}^T$ and $\varphi = \begin{bmatrix} 0 & h(t) \end{bmatrix}^T$.

Lemma 1 [88]: For any bounded function $f(t)$, $\exists$ a scalar δ such that the observed states of the system defined in (3.37) are bounded, $||\varepsilon|| \geq \delta \; \forall t \geq T \geq 0$.

The proof of the *Lemma 1* can be found in [52].

Based on the estimation ($\hat{P}_l$), the controller expression is given as

$$P_g^* = \mu(\tilde{e}) + \hat{P}_l(t) \tag{3.38}$$

where, $\mu(\tilde{e}) = K_3\tilde{e} + \dot{e}^*\hat{C}$.

This leads to the following expression of regulation error dynamics

$$C\dot{\tilde{e}} = -K_3\tilde{e} - \dot{e}^*\tilde{C} + \varepsilon_{P_l}. \tag{3.39}$$

To implement the voltage controller, the control law given by (3.38) is used where the term for the external load disturbance ($\hat{P}_l(t)$) is estimated by the ESO. The ESO is implemented using the expression given by (3.35).

Remark 3: In general, for both the current and voltage controllers the tracking error not only tends to zero asymptotically, instead, it converges within finite time, determined by the gain matrices K, Λ and gains K_3, γ. These gains are limited by different factors such as noise to signal ratio (in measurement), high-frequency unmodeled dynamics.

3.4 Parameters selection procedure

To ensure the stability of the system, both K_{ii} and Λ_{ii} must be positive. The choice of Λ_{ii} depends on how quickly the controller adapts to the change in the parameters of the system, but for a practical system, it cannot be set to a large value due to the presence of measurement noise in the sensed signal. The high value of K_{ii} increases the bandwidth, so the response is much faster, but it affects the disturbance rejection capabilities of the controller and also increases the peak overshoot. Hence, an optimal value is decided based on the simulation done in Matlab. The environment for the simulation study is given in the table below (Table- 3.1). Three desired control criteria like settling time, maximum overshoot and the steady-state RMS error is plotted (Figures 3.4, 3.5 and 3.6), when d- axis reference current i_d^* is changed from 5 A to 8 A. The plots are taken for different combination of K_{ii} and Λ_{ii}, where K_{ii} varies from 0.05 to 0.19 with an increment of 0.02 and Λ_{ii} varies from $1/400$ to $1/1000$. The study has been done for three different values of the inductor, which proves that the proposed controller is adaptive to any parametric change. It can be seen from Figures 3.4, 3.5 and 3.6 that 0.07 to 0.11 is the optimal value for K_{ii} whereas, for Λ_{ii} the controller introduces disturbances for all the inductors at values close to $1/200$. Λ_{ii} can be as low as $1/1200$ and this value is working with all combinations of K_{ii}. In addition to that, the designed controller is working fine for the range below and above 50% of the input ac voltage (230 V phase-neutral). It is to be noted that, similar phenomena are observed when a step-change is employed in q- axis reference current (i_q^*), though plots are provided only for the d-axis current.

As the voltage and current controller form a cascade control structure, the gain of the outer loop controller are kept typically ten times lower than the K_{ii}. The choice of adaptive gain γ is likewise.

According to the Hurwitz stability criterion, the parameters (α_1 and α_2) of ESO should be positive. In general, a larger ESO bandwidth will produce more accurate estimation, but it will be more sensitive towards the noise.

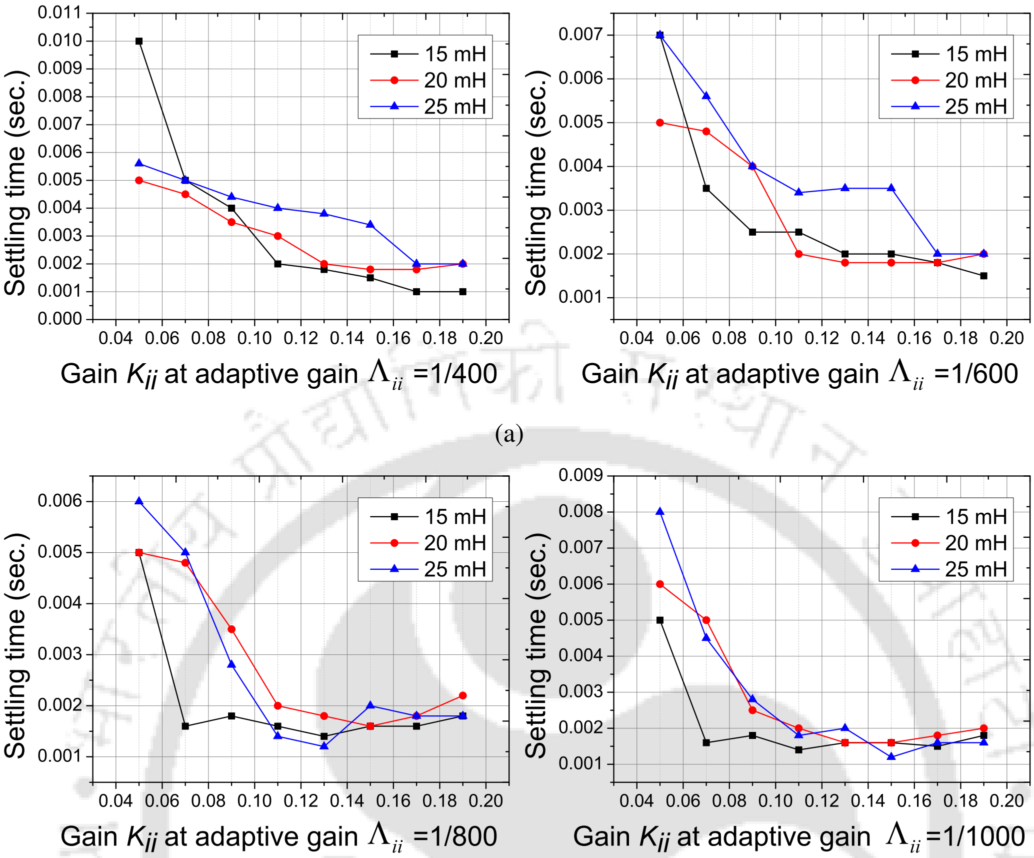

(a)

(b)

Figure 3.4: Plots of settling time with respect to controller gains (K_{ii}) for different values of filter parameters for step-change in i_d at different Λ_{ii}

3.5 Simulation results and discussion

The proposed current and voltage control algorithm is simulated in Matlab, and the results of the simulation experiments are provided below. The nominal value of the grid filter is chosen as L_f = 15 mH and r_f = 0.5 Ω and the DC load resistance is chosen as R_{dc} = 200 Ω. The results of the simulation experiments are provided below.

3.5.1 Performance evaluation of the proposed current controller

The dynamic performances of the proposed adaptive MIMO current controller are evaluated by employing step-changes in d and q-axis reference currents. During the performance evaluation of current controller, the voltage controller is deactivated.

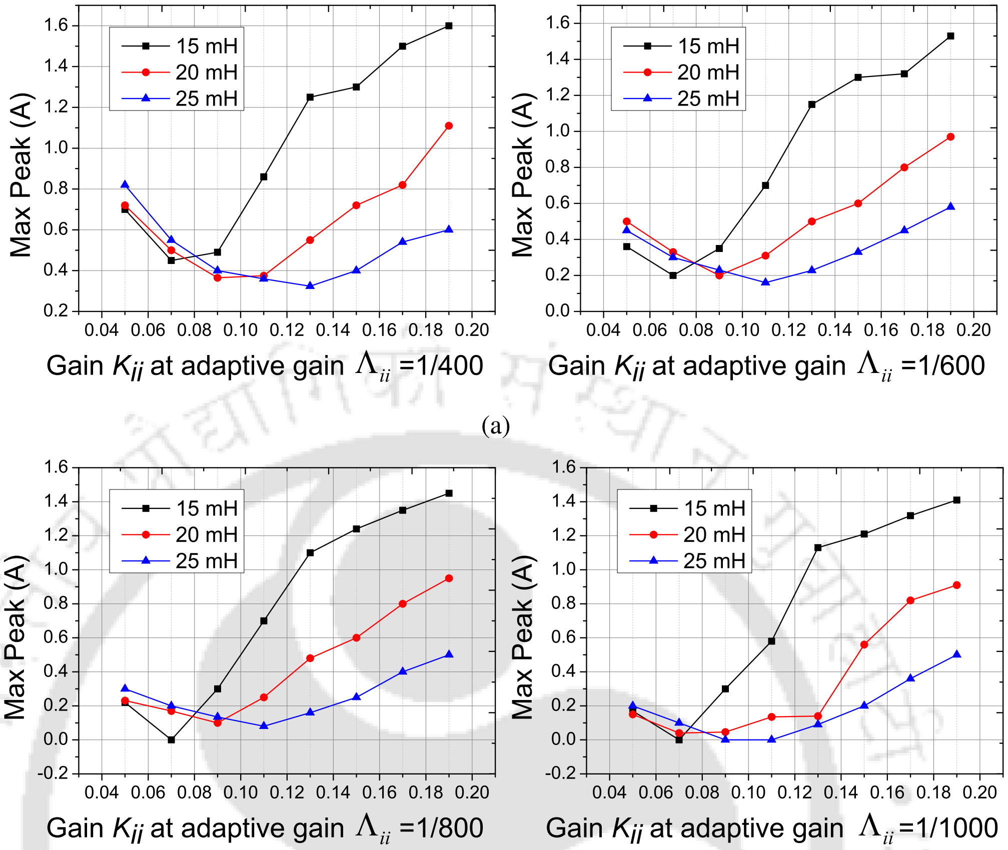

(a)

(b)

Figure 3.5: Plots of maximum peak with respect to controller gains (K_{ii}) for different values of filter parameters for step-change in i_d at different Λ_{ii}

3.5.1.1 First case: step-change in reference *d*-axis current

For this test, the q-axis current (i_q^*) is fixed at 0 A and a step-change of 5 A (from 6 A to 11 A) is employed to the d-axis reference current (i_d^*) at 5 s. It can be observed from Figure 3.7(a) that the

Table 3.1: System parameters for simulation study

Parameters	Values
Discrete power Gui	1 microsecond
Algorithm sampling rate	5 kHz
Converter switching frequency	5 kHz
Phase-neutral voltage in rms	230 V
Source frequency ω_g	50 Hz
Filter inductance L_f	15 mH, 20 mH, 25 mH
Voltage Reference (DC) V_{dc}	700 V
DC load resistance (R_L)	200 Ω

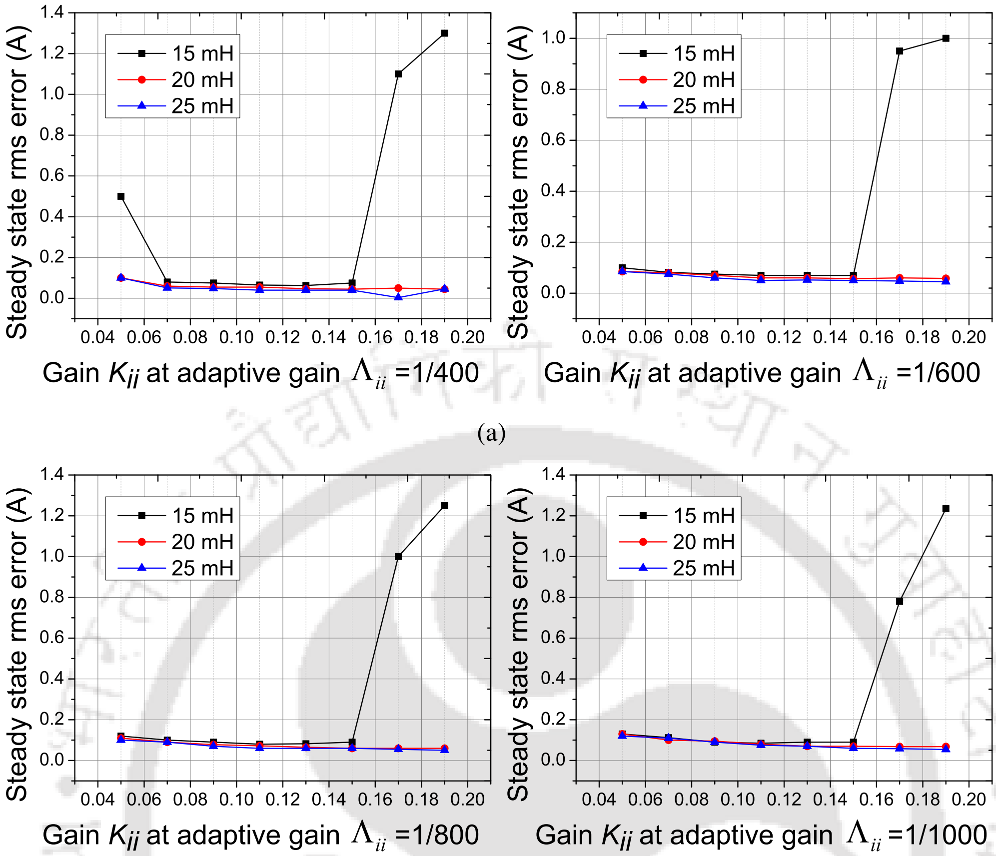

(a)

(b)

Figure 3.6: Plots of steady state rms error with respect to controller gains (K_{ii}) for different values of filter parameters for step-change in i_d at different Λ_{ii}

measured current tracks the reference current within 5 ms. Since $i_q^* = 0$, the phase-a voltage v_a and phase-a current i_a are in same phase (Figure 3.7(b)). Since i_d^* is changed, a change is also observed at 5 s for the DC bus voltage (V_{dc}) (Figure 3.7(c)).

3.5.1.2 Second case: step change in reference q-axis current

For this test, the d-axis current (i_d^*) is fixed at 11 A and a step change of 5 A (from 0 A to -5 A) is employed to the q-axis reference current (i_q^*) at 7 s. It can be observed from Figure 3.8(a) that the measured current tracks the reference current within 5 ms. Since i_q^*= -5 A, the phase-a voltage v_a and phase-a current i_a has phase difference (Figure 3.8(b). Since i_d^* is kept at constant value, the DC bus voltage (Figure 3.8(c)) remains unchanged during the transition in i_q^*.

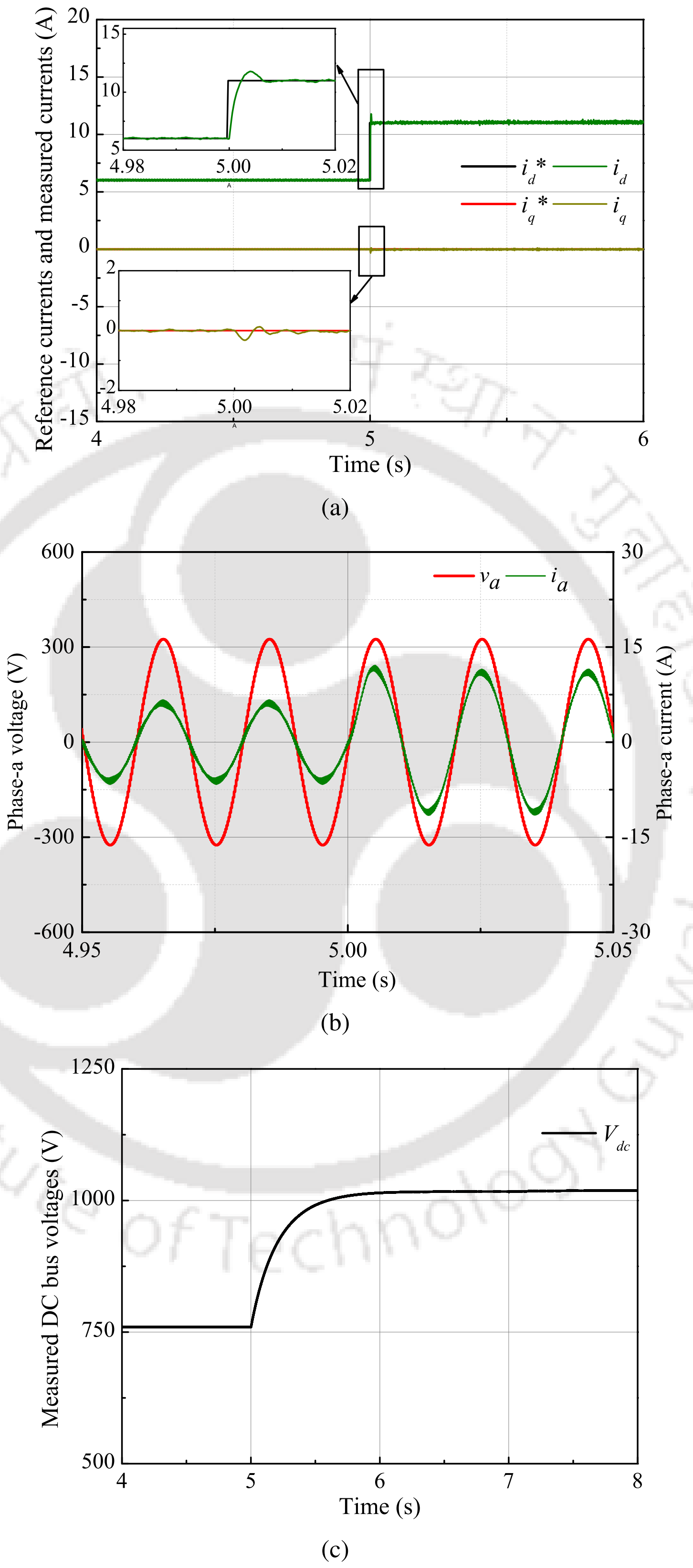

Figure 3.7: Simulation result regarding the performance of the proposed adaptive current controller under the step change in i_d^* from 6 A to 11 A; (a) Plots dq- axis currents; (b) Plots of phase-a voltage and current; (c) Plot of DC bus voltage.

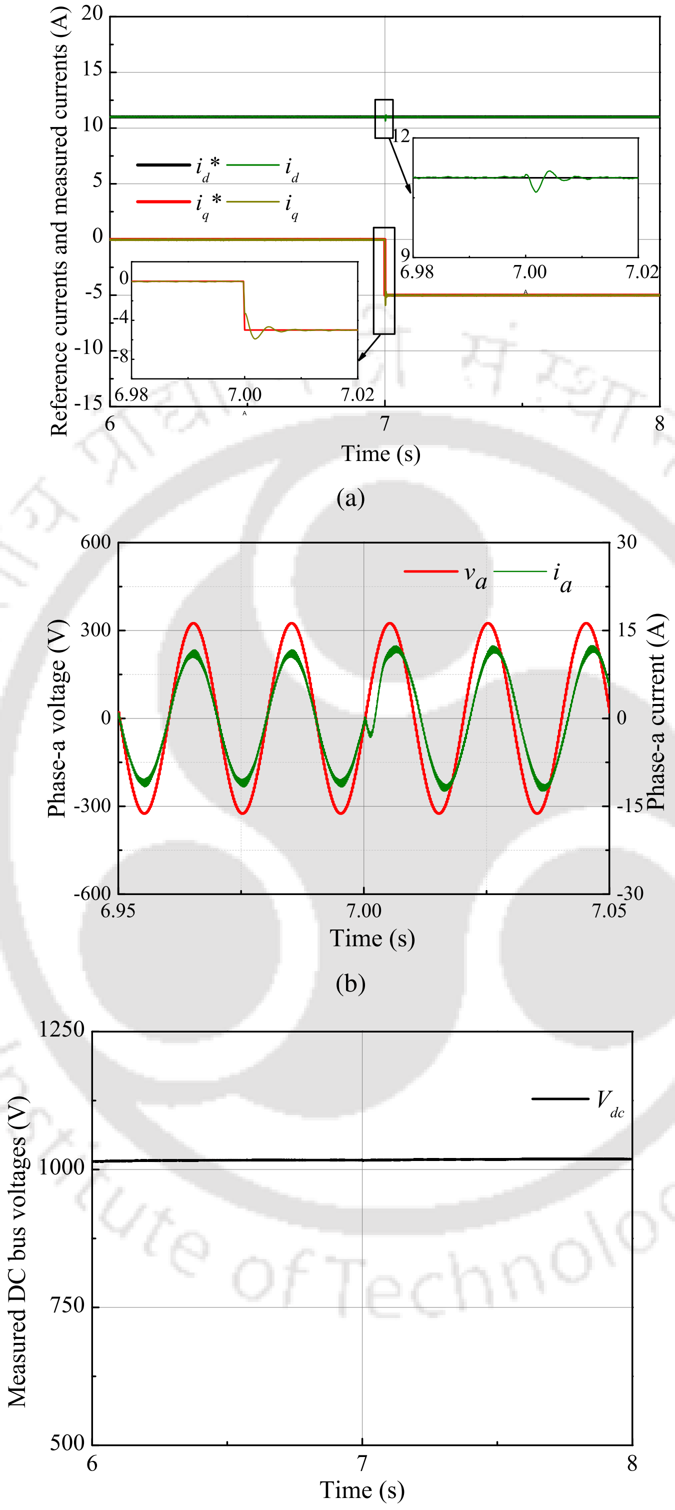

(a)

(b)

(c)

Figure 3.8: Simulation result regarding the performance of the proposed adaptive current controller under the step change in i_q^* from 0 A to -5 A; (a) Plots *dq*- axis currents; (b) Plots of phase-a voltage and current; (c) Plot of DC bus voltage.

3.5.2 Performance evaluation of the proposed ESO-based voltage controller

The proposed current controller performs excellently under the step changes while fulfilling different performance criteria like fast convergence, low overshoot, and least perturbation. For testing the proposed voltage controller, the proposed current controller is utilized in the inner control loop. During the test of the proposed ESO-based voltage controller, a step change in load resistance is employed across the DC link capacitor, and the dynamic performance of the proposed voltage control strategy is shown in Figure 3.9. During this test, the performance of the proposed voltage controller is evaluated by changing the load resistance suddenly across the DC bus (from 100 Ω to 200 Ω) at 4 s. The DC bus voltage and the DC load current is plotted and shown in Figure 3.9(c). Figure 3.9(a) represents the corresponding d and q-axis currents and Figure 3.9(b) represents the corresponding phase-a voltage and current. From Figure 3.9(c), it can be observed that the DC bus voltage settles down within 300 ms. The proposed voltage controller shows excellent performance in terms of peak overshoot and an overshoot of 6.5 V can be observed in Figure 3.9(c).

3.6 Experimental results and discussion

The effectiveness of the proposed control algorithm is validated through practical experiments conducted in the laboratory, and its performance is compared with the PI-based controller. The description of nominal parameters for the experimental test setup is given in Table-3.2, and the experimental setup is shown in Figures 3.10 and 3.11. The voltage is fed to the converter by an autotransformer, and for the DC load, a resistive load connected across the DC link capacitor is used. The different gains associated with both of the controllers are shown in Table-3.3. The experimental observations related to proposed controllers are given in subsequent subsections. The full picture of the experimental setup can be found in Appendix A (Figure A.1).

3.6.1 Current controller performance

The dynamic performance of the current controller is evaluated by a step change in the reference quantities. During the evaluation of the current controller performance, the voltage controller is disabled. For the first case, the reference i_d^* has a step change from 1 A to 2 A, while keeping i_q^*

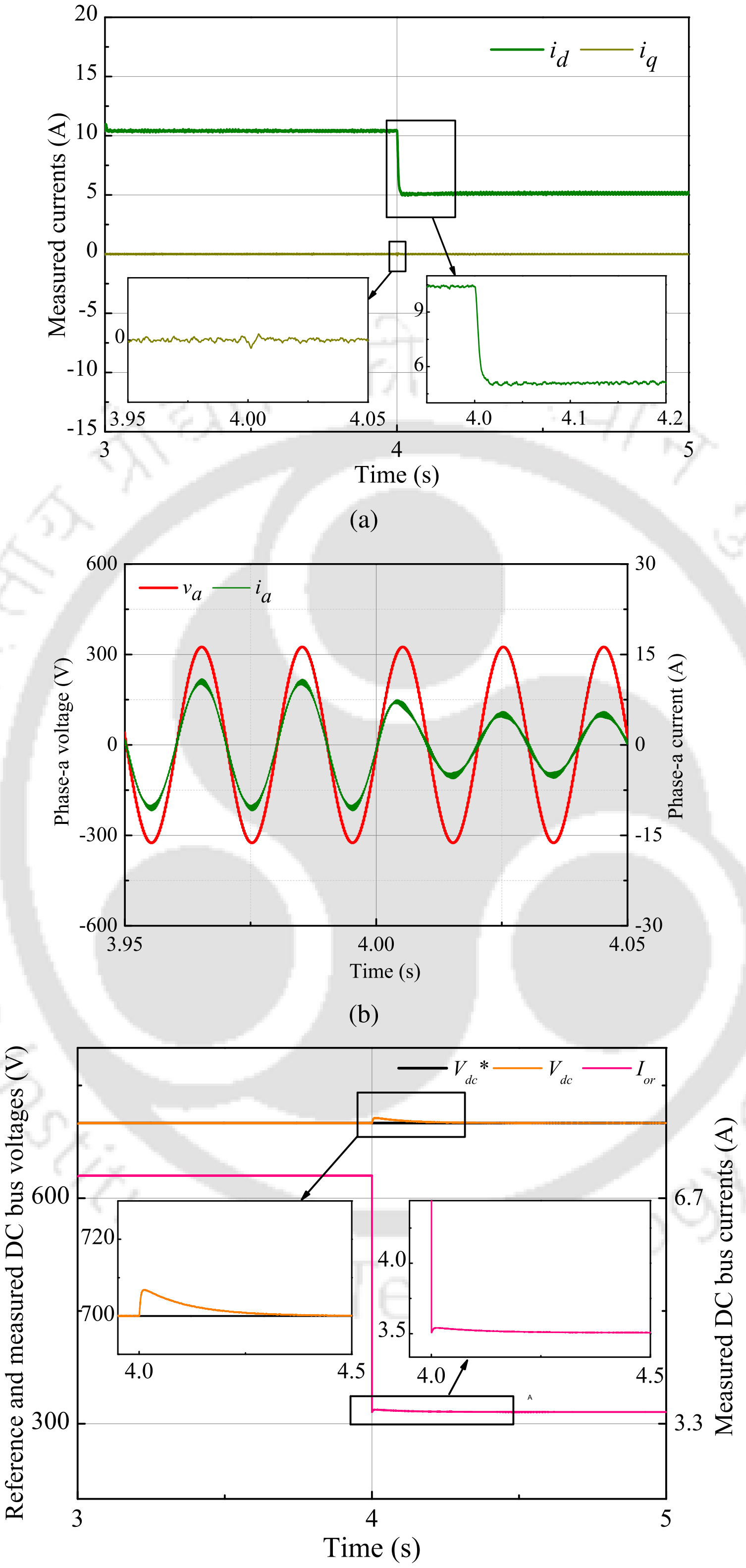

(a)

(b)

(c)

Figure 3.9: Simulation result regarding the performance of the proposed voltage controller under the step change of 100 Ω in load resistance; (a) Plots dq- axis currents. (b) Plots of phase-a voltage and current. (c) Plot of DC bus voltage.

Table 3.2: Nominal parameters for experimental system

Parameters	Values
L-L voltage in rms	17 V
Nominal frequency ω_g	50 Hz
Voltage Reference (DC) V_{dc}	50 V
Filter inductance L_f	15 mH
Parasitic resistance r_f	0.5 Ω
ADC sampling rate	5 kHz
Converter switching frequency	5 kHz

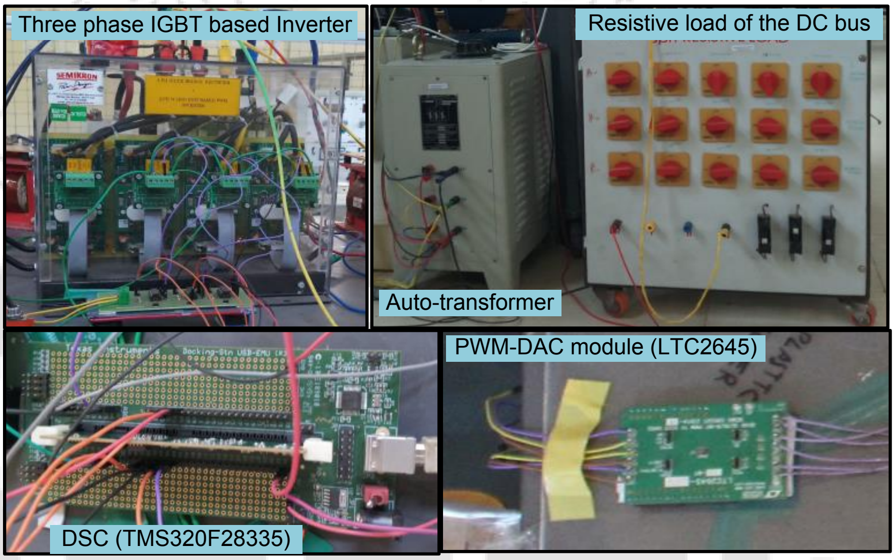

Figure 3.10: Laboratory test setup for hardware experimentation

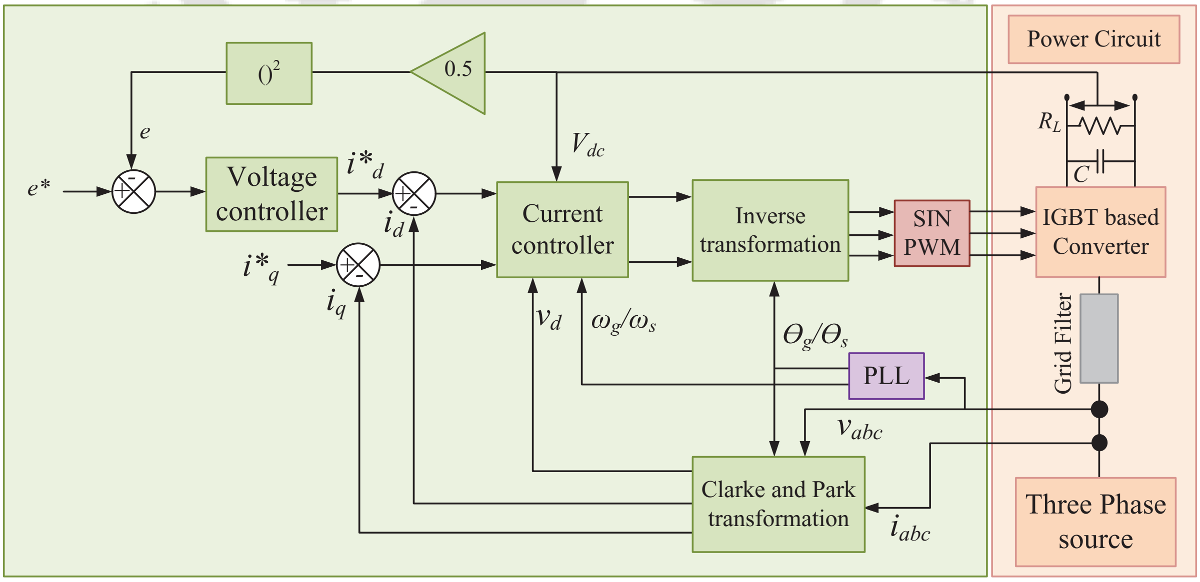

Figure 3.11: Schematic of the experimental test setup

Table 3.3: Controller parameters for experimental system

Adaptive control parameters	Values
Current control loop (K_{ii} and Λ_{ii})	0.11 and 0.2
Voltage control loop K_3 and γ	0.01 and 0.02
ESO parameters α_1 and α_2	0.5 and 30
PI regulator	Values
Current control loop k_p and k_i	11 and 0.4
Voltage control loop k_{p1} and k_{i1}	0.11 and 0.05

constant. For the second case, the q-axis component of the current i_q^* is changed from -1 A to 0 A keeping i_d^* constant. $i_q^* = 0$ demonstrates the ability of the control algorithm to switch to unity power factor (UPF) mode. The oscilloscope snapshots are presented to show the transient performance of the proposed control algorithm (Figure 3.12- Figure 3.16). The value of i_d and i_q are taken from the PWM DAC module (LTC2645). The DC bus voltage, the phase-a voltage and current are observed using the voltage and current probes.

3.6.1.1 Proposed current controller performance under the step change in d-axis reference current

The First test is done by keeping the i_q^* constant, and changing the reference value for the d-axis current i_d^* from 1 A to 2 A, as shown in Figure 3.12 and Figure 3.13. It is observed from the performance curve depicted by Figures 3.12(a) and 3.13(a), that both the controllers achieve the control task within one cycle and without any overshoot, but small oscillation is observed in the q-axis current with the PI controller (Figure 3.12(a)). Since i_d is directly related to the DC bus voltage, a change in i_d results into the change in the DC voltage (Figures 3.12(a) and 3.13(a)).

3.6.1.2 Proposed current controller performance under the step change in q-axis reference current

The second test is done by keeping the i_d^* constant, and changing the reference value for the q-axis current i_q^* from -1 A to 0 A, as shown in Figure 3.14 and Figure 3.15. Both the controller track the reference within one cycle without any significant overshoot. The presence of some oscillation in i_q and V_{dc} is observed with the PI controller (Figure 3.14(a)) whereas the proposed controller shows an excellent tracking performance without any oscillation (Figure 3.15(a)).

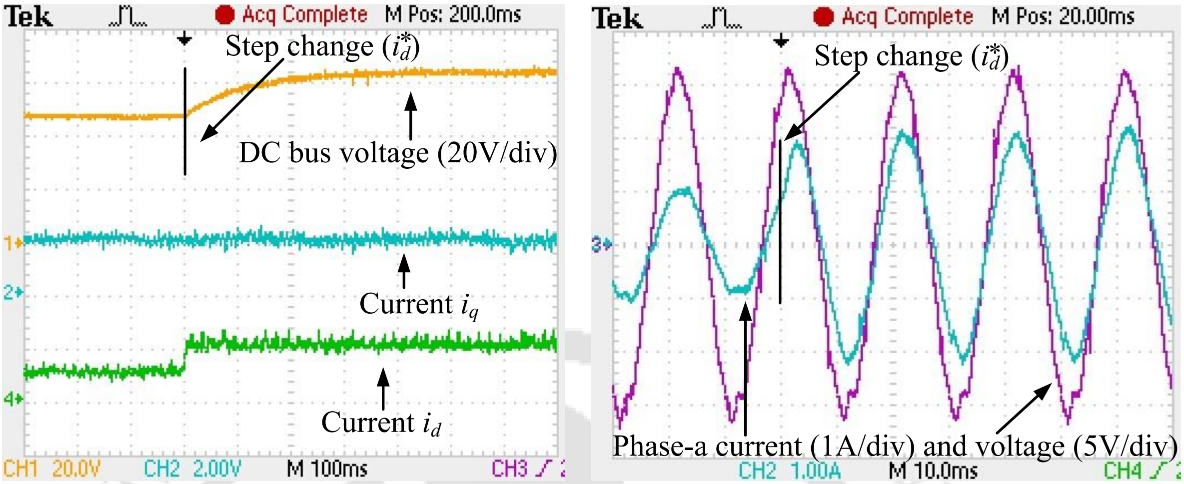

(a) (b)

Figure 3.12: Experimental result regarding the performance of PI current controller under the step change in i_d^* from 1 A to 2 A in UPF; (a) DC bus voltage and *dq*- axis currents. (b) Phase-a voltage and current.

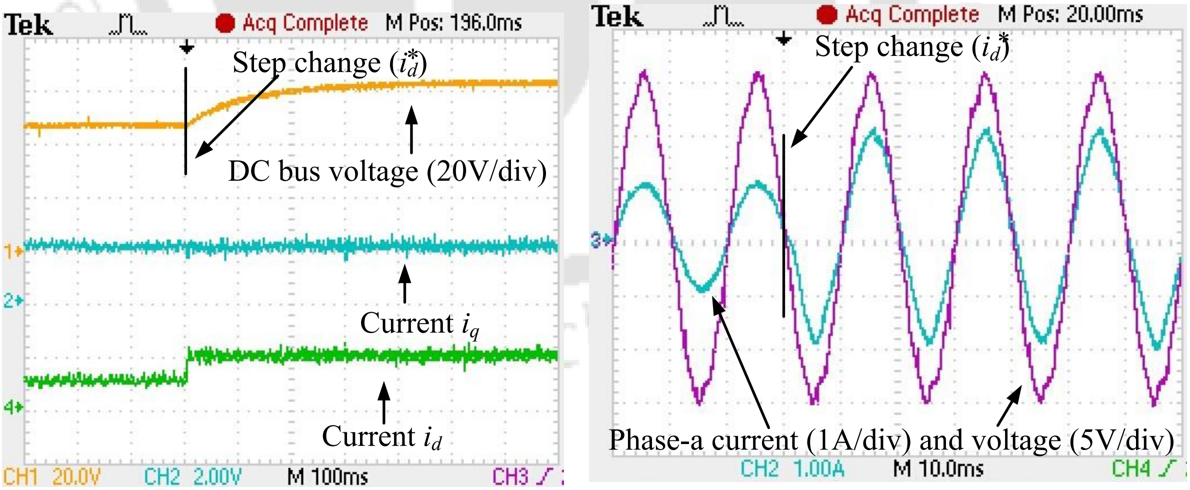

(a) (b)

Figure 3.13: Experimental result regarding the performance of the proposed adaptive current controller under the step change in i_d^* from 1 A to 2 A in UPF; (a) DC bus voltage and *dq*- axis currents. (b) Phase-a voltage and current.

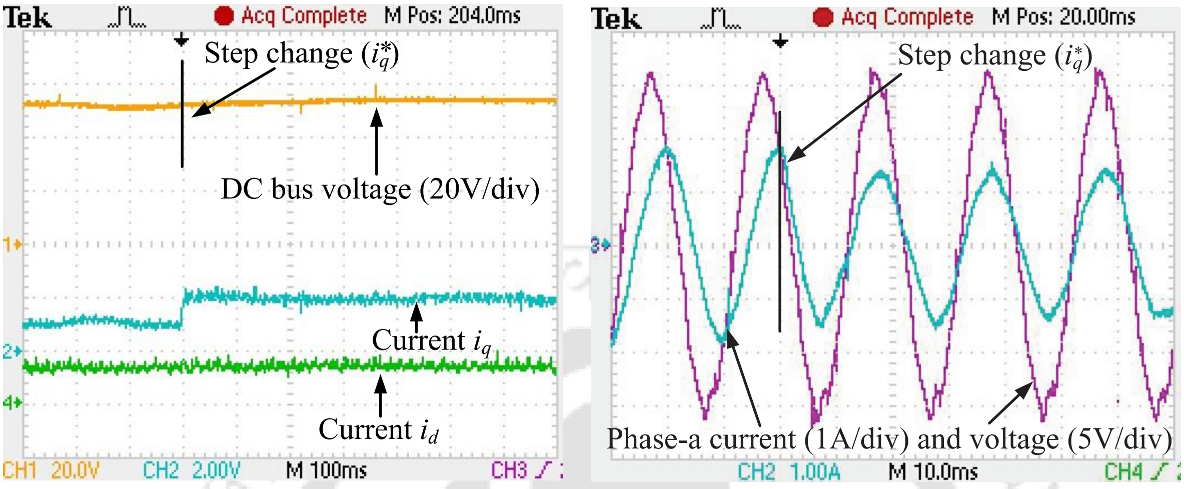

(a) (b)

Figure 3.14: Experimental result regarding the performance of PI current controller under the step change in i_q^* from -1 A to 0 A; (a) DC bus voltage and *dq*- axis currents. (b) Phase-a voltage and current.

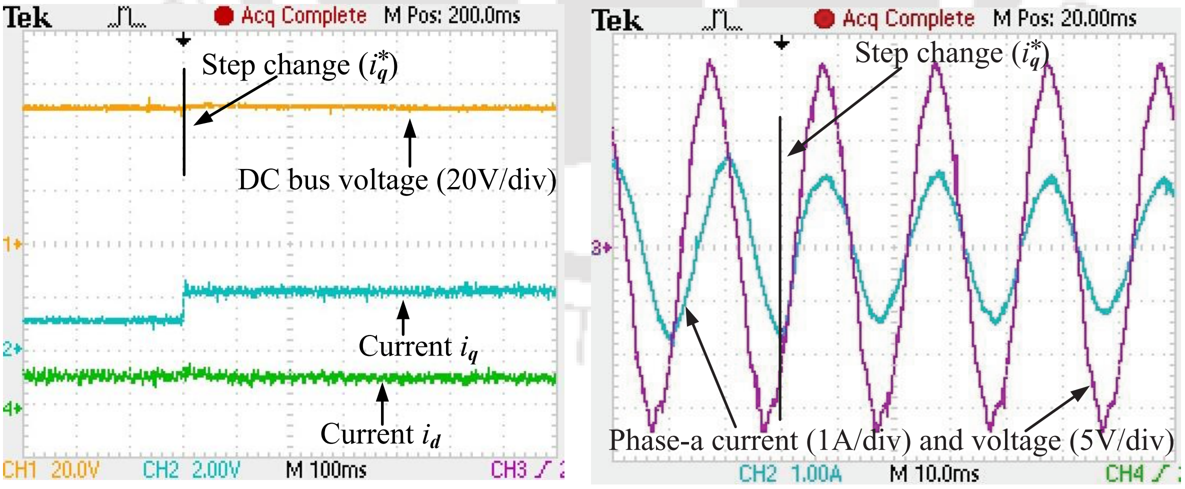

(a) (b)

Figure 3.15: Experimental result regarding the performance of the proposed adaptive current controller under the step change in i_q^* from -1 A to 0 A; (a) DC bus voltage and *dq*- axis currents. (b) Phase-a voltage and current.

3.6.1.3 Proposed current controller performance under parametric variations

For evaluating the controller performance under parametric variations, one 2 mH inductor has been added in series with the existing 15 mH inductor in each phase. During the closed-loop operation of the current controller, the 2 mH inductors have been suddenly bypassed by providing a conducting path across it. This results in a step change in filter parameters. It is observed from Figure 3.16(a) that the effect of the step change in the parameter variation does not introduce any variation in the currents i_d, i_q and DC bus voltage. The yellow trace of Figure 3.16(b) represents the current flowing through the conducting path across the 2 mH inductor of phase-a. It can be seen from Figure 3.16(b) that after shorting the inductor, the total current of phase-a represented by the blue trace flows through the parallel path (yellow trace) and the 15 mH series inductor. Thus the inductor of 2 mH has been bypassed. From Figure 3.16(a), it can be observed that the designed current controller is insensitive to the variation of the L_f- filter parameter.

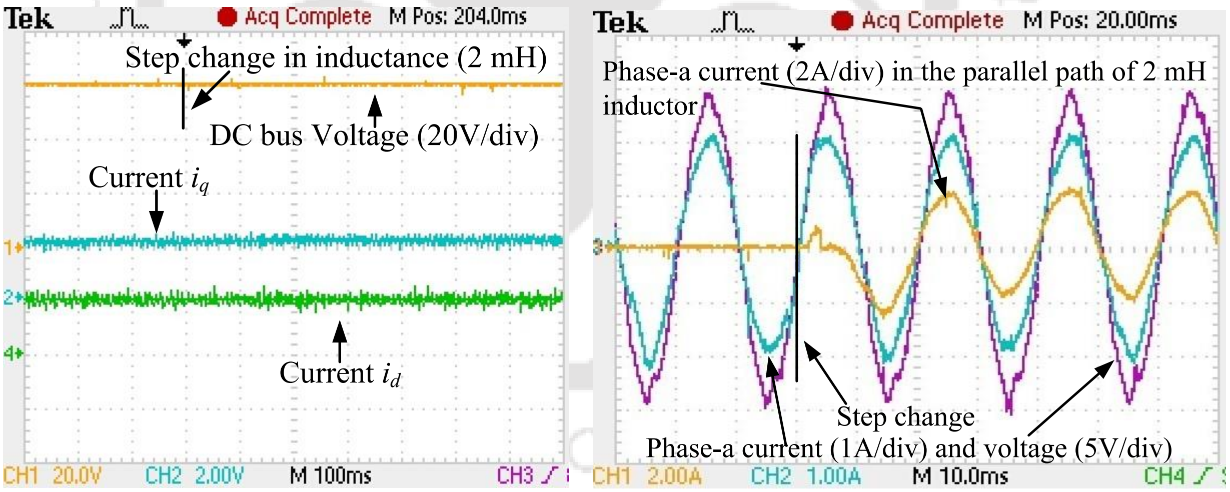

(a) (b)

Figure 3.16: Experimental result regarding the performance of the proposed adaptive current controller under the step change in inductance of 2 mH; (a) DC bus voltage and *dq*- axis currents. (b) Phase-a voltage and current.

3.6.2 Voltage controller performance under the step change in DC load

The performance of the proposed voltage controller is compared with the PI-based controller, and shown in Figures 3.17-3.19. During this test, both voltage and current controllers are in operation. The parameters related to the ESO and the proposed voltage controller are given in Table 3.3. A step change in the resistive load (116 Ω to 220 Ω) is applied across the DC bus, to observe the transient performances for both the controllers and the performance curves are shown in Figures 3.17(a) and 3.19(a). The settling time for the proposed controller is 300 ms approximately (Figure 3.19(a)), whereas the settling time for the PI regulator is 4 s (Figure 3.17(a)). Hence, the time scale (Figure 3.17(a)) is chosen as 500 ms/div in the case of PI voltage regulator to capture the transient performance, whereas the time scale is chosen (Figure 3.19(a)) for the proposed algorithm is 100 ms/div. For both of the controllers, the peak overshoot is approximately 5 V (Figures 3.17(a) and 3.19(a)). It has been checked experimentally, that improving the dynamic performance of the system by further increasing the bandwidth of the PI-based voltage controller results in instability. Hence, it is difficult to improve the system's dynamic performance with the use of the PI controller. Moreover, it is observed from the phase-a current waveforms (Figures 3.18 and 3.20), that the PI regulator introduces more disturbances in the supply current than the proposed algorithm.

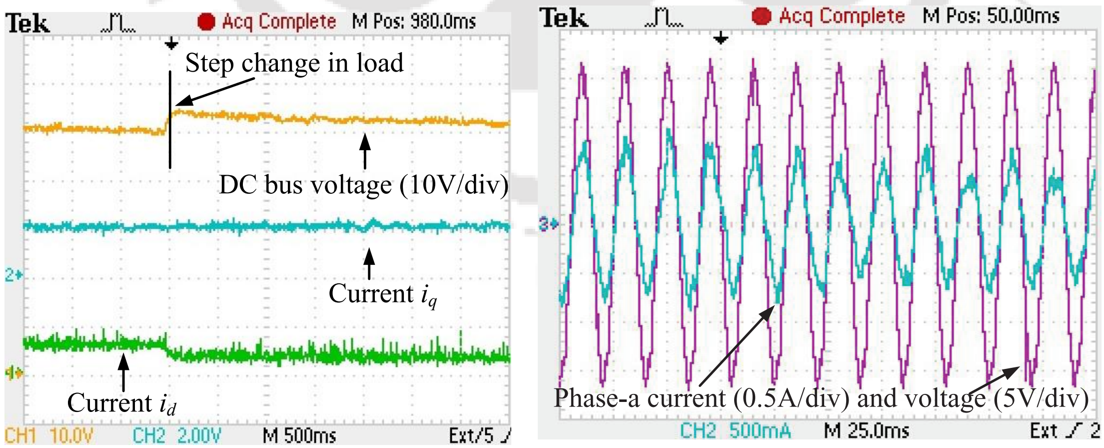

(a) (b)

Figure 3.17: Experimental result regarding the performance of the PI voltage controller under the step change in DC load (R_{dc} - 116 Ω to 220 Ω) in UPF; (a) DC bus voltage and *dq*- axis currents. (b) Phase-a voltage and current.

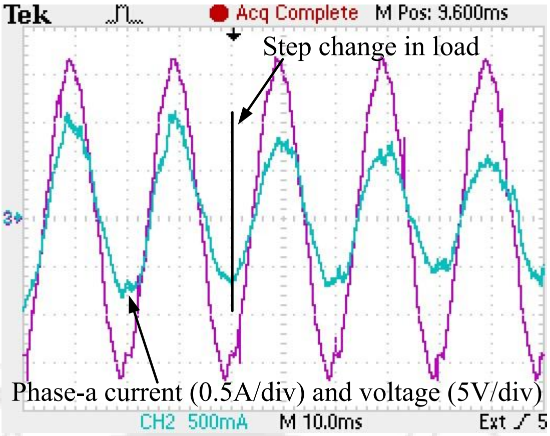

Figure 3.18: Enlarged view of the phase-a voltage and current under the load step for the PI controller

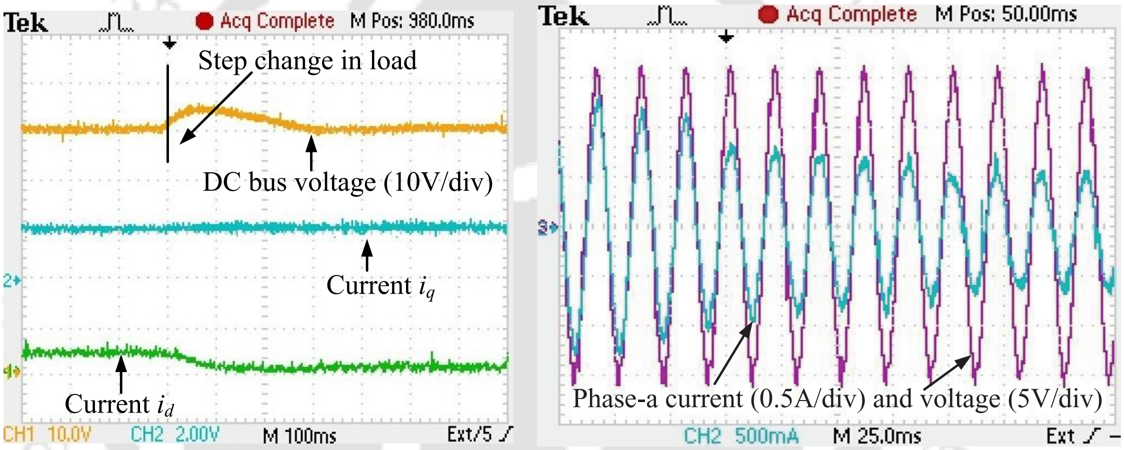

(a) (b)

Figure 3.19: Experimental result regarding the performance of the proposed voltage controller under the step change in DC load (R_{dc} - 116 Ω to 220 Ω) in UPF; (a) DC bus voltage and dq- axis currents. (b) Phase-a voltage and current.

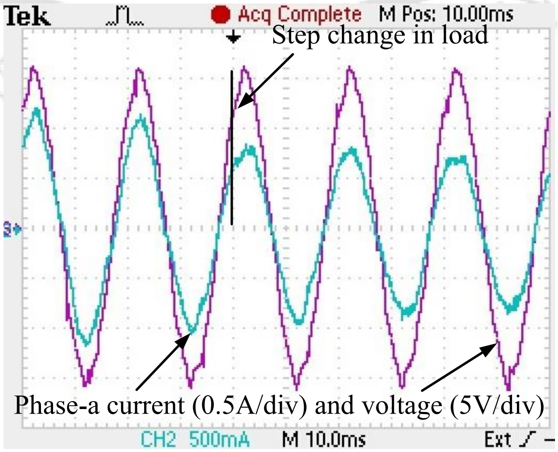

Figure 3.20: Enlarged view of the phase-a voltage and current under the load step for the for the proposed voltage controller

3.7 Summary

The adaptive control technique is a promising approach to solve the control problem for these three-phase power converters. The proposed current control algorithm works perfectly under any step changes. Information about the system parameters is not required for the implementation of the proposed current controller. Therefore, it can be said that the current controller is independent of the system parameters variation. For the voltage control, the proposed algorithm performs way better than the PI voltage controller in terms of fast convergence and high accuracy for any step change in the DC load. The proposed control algorithm generates a constant switching frequency to control the six IGBT switches. Due to safety reasons, the DC bus voltage has been kept under 70 V. The experiment has been done using the supply available in our laboratory. Due to the presence of a large number of nonlinear loads, the available supply voltage is distorted. However, this proves the robustness of the controller and the phase-lock-loop (PLL) system. The adaptive nature of the proposed voltage controller is given up due to the implementation of the extended state observer (ESO). Overall it can be concluded that the control objective is satisfied with a great deal of accuracy under the parametric uncertainty by the proposed controller.

4

Development of a smooth robust current control strategy for the three-phase GSC

Contents

4.1 Introduction

The previous Chapter (Chapter 3) was on the design and implementation of adaptive controllers for grid side converter (GSC). These adaptive controllers are effective but require significant effort for design. Hence, this Chapter proposes a sliding mode controller (SMC) for the control of GSC. The design procedure involved in an SMC is much simple, and these techniques are robust to the external disturbances, and parametric uncertainties. Furthermore, performance criteria like high accuracy, good convergence rate and fast dynamic response can be realized by these techniques. However, these techniques suffer from output chattering, which is the inherent problem of first order-based sliding mode control technique (FOSMC). The literature survey shows some existing methods such as the use of a low pass filter (LPF) or use of a saturation function instead of sign function [56, 57] to mitigate the effect of chattering, however, there is a need of some better methods to address this problem.

In this Chapter, a smooth robust controller based on FOSMC technique is proposed to control the active and reactive grid currents. Fundamentally, these techniques have an inherent output chattering problem. In this work, an effort has been made to design a smooth robust controller in the form of a first-order sliding mode controller so that output chattering can be minimized. The proposed controller is formulated in *dq*-domain, and control pulses are generated by means of SINPWM to drive the power converter. A systematic procedure is provided to formulate the control law, and special attention is given for achieving chattering free output. This Chapter includes stability proof along with the procedure to choose the gains for the observer. The Lyapunov-based method is utilized to choose the sliding gains for the proposed controller.

4.2 Formulation of the smooth robust current controller

To derive the smooth robust current controller, the same dynamic model in *dq*-domain as discussed in the previous Chapter (Chapter 3) is used. The dynamic model in *dq*-domain is expressed as

$$\begin{aligned} \frac{di_d}{dt} &= -\frac{r_f}{L_f} i_d + \omega_g i_q + \frac{v_{dg}}{L_f} - u_d \frac{V_{dc}}{2L_f} \\ \frac{di_q}{dt} &= -\frac{r_f}{L_f} i_q - \omega_g i_d + \frac{v_{qg}}{L_f} - u_q \frac{V_{dc}}{2L_f} \end{aligned} \tag{4.1}$$

$$C\frac{d}{dt}(V_{dc}) = I_{os} - I_{or} \tag{4.2}$$

Since the proposed PLL technique (Chapter 2) is used to execute the transformation from three-phase variable to stationary DC variable hence, $v_d = \left|\vec{v}_g\right|$ and $v_q = 0$. Therefore, (4.1) can be further expressed as

$$\begin{aligned} \frac{di_d}{dt} &= -\frac{r_f}{L_f} i_d + \omega_g i_q + \frac{v_{dg}}{L_f} - u_d \frac{V_{dc}}{2L_f} \\ \frac{di_q}{dt} &= -\frac{r_f}{L_f} i_q - \omega_g i_d - u_q \frac{V_{dc}}{2L_f} \end{aligned} \tag{4.3}$$

4.2.1 Formulation

To fulfil the control objective of maintaining i_d and i_q at their desired level i.e. $i_d \rightarrow i_d^*$ and $i_q \rightarrow i_q^*$, a new variable S_{dq} is defined as

$$S_{dq} = \begin{bmatrix} S_d \\ S_q \end{bmatrix} = \begin{bmatrix} i_d^* - i_d \\ i_q^* - i_q \end{bmatrix} \tag{4.4}$$

Therefore the time derivative of S_{dq} can be written as

$$\dot{S}_{dq} = \begin{bmatrix} \dot{S}_d \\ \dot{S}_q \end{bmatrix} = \begin{bmatrix} \frac{di_d^*}{dt} - \frac{di_d}{dt} \\ \frac{di_q^*}{dt} - \frac{di_q}{dt} \end{bmatrix} \tag{4.5}$$

From (4.3), plugging the value of $\frac{di_d}{dt}$ and $\frac{di_q}{dt}$ in (4.5), $\dot{S}_{dq}$ can be expressed as

$$\begin{aligned} \dot{S}_d &= \frac{di_d^*}{dt} - \left(-\frac{r_f}{L_f} i_d + \omega_g i_q + \frac{v_d}{L_f} - u_d \frac{V_{dc}}{2L_f}\right) \\ \dot{S}_q &= \frac{di_q^*}{dt} - \left(-\frac{r_f}{L_f} i_q - \omega_g i_d - u_q \frac{V_{dc}}{2L_f}\right). \end{aligned} \tag{4.6}$$

Putting $\dot{S}_{dq} = 0$ in (4.6), the expression for the equivalent control law can be derived as

$$\begin{aligned} \bar{u}_d &= \left\{-\frac{di_d^*}{dt} + \left(-\frac{\hat{r}_f}{L_f} i_d + \hat{\omega}_g i_q + \frac{v_d}{L_f}\right)\right\} \frac{2L_f}{V_{dc}} \\ \bar{u}_q &= \left\{-\frac{di_q^*}{dt} + \left(-\frac{\hat{r}_f}{L_f} i_q - \hat{\omega}_g i_d\right)\right\} \frac{2L_f}{V_{dc}} \end{aligned} \tag{4.7}$$

The control law is defined as

$$\begin{aligned} u_d &= \bar{u}_d - \frac{2L_f}{V_{dc}} \left(K_d - \dot{\phi}_d\right) \text{ sat}\left(\frac{S_d}{\phi_d}\right) \\ u_q &= \bar{u}_q - \frac{2L_f}{V_{dc}} \left(K_q - \dot{\phi}_q\right) \text{ sat}\left(\frac{S_q}{\phi_q}\right) \end{aligned} \tag{4.8}$$

where $K_d = F_d + \eta_d$ and $K_q = F_q + \eta_q$; $\eta_d, \eta_q > 0$ and $F_d \geq \left|\hat{f}_d - f_d\right|$, $F_q \geq \left|\hat{f}_q - f_q\right|$.

The saturation function (Figure 4.1) is defined as

$$\text{sat}\left(\frac{S}{\phi}\right) = \begin{cases} \frac{S}{\phi} & \text{if } |S| \leq \phi \\ \text{sgn}(s) & \text{if } |S| > \phi \end{cases} \tag{4.9}$$

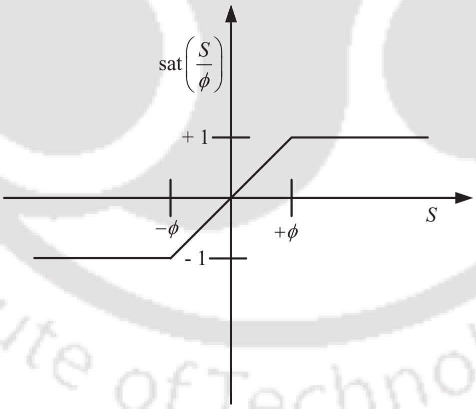

Figure 4.1: Saturation Function

Substituting (4.7) into (4.8) and then (4.8) into (4.6), the expression for $\dot{S}_d$ and $\dot{S}_q$ can be further expressed as

$$\begin{aligned} \dot{S}_d &= \left(\hat{f}_d - f_d\right) - \left(K_d - \dot{\phi}_d\right) \text{ sat}\left(\frac{S_d}{\phi_d}\right) \\ \dot{S}_q &= \left(\hat{f}_q - f_q\right) - \left(K_q - \dot{\phi}_q\right) \text{ sat}\left(\frac{S_q}{\phi_q}\right) \end{aligned} \tag{4.10}$$

where f represents the true dynamics and $\hat{f}$ is the estimated dynamics. The terms f_d, f_q and $\hat{f}_d$, $\hat{f}_q$ are defined as

$$\begin{aligned} f_d &= -\frac{r_f}{L_f} i_d + \omega_g i_q + \frac{1}{L_f} v_d \\ f_q &= -\frac{r_f}{L_f} i_q - \omega_g i_d. \end{aligned} \tag{4.11}$$

$$\begin{aligned} \hat{f}_d &= -\frac{\hat{r}_f}{\hat{L}_f} i_d + \hat{\omega}_g i_q + \frac{1}{\hat{L}_f} v_d \\ \hat{f}_q &= -\frac{\hat{r}_f}{\hat{L}_f} i_q - \hat{\omega}_g i_d \qquad . \end{aligned} \tag{4.12}$$

4.2.2 Stability analysis

A Lyapunov function is defined subjected to the dynamics given in (4.3) as

$$V = 0.5S_d^2 + 0.5S_q^2 \tag{4.13}$$

The time derivative of the Lyapunov function can be expressed as

$$\dot{V} = S_d \dot{S}_d + S_q \dot{S}_q. \tag{4.14}$$

Lyapunov stability theory states that a positive definite function (V) must have a negative definite first derivative ($\dot{V}$) for achieving stability.

Replacing $\dot{S}_d$ and $\dot{S}_q$ from (4.10) into (4.13), the time derivative $\dot{V}$ can further be expressed as

$$\dot{V} = S_d \left\{ \left(\hat{f}_d - f_d \right) - \left(K_d - \dot{\phi}_d \right) \text{ sat} \left(\frac{S_d}{\phi_d} \right) \right\} + S_q \left\{ \left(\hat{f}_q - f_q \right) - \left(K_q - \dot{\phi}_q \right) \text{ sat} \left(\frac{S_q}{\phi_q} \right) \right\} \tag{4.15}$$

Since, outside the boundary layer (Figure 4.1) the value of $\text{sat}\left(\frac{S}{\phi}\right) = \text{sgn}(S)$ hence, (4.15) can be further expressed as

$$\dot{V} = S_d \left(\hat{f}_d - f_d \right) - \left(K_d - \dot{\phi}_d \right) |S_d| + S_q \left(\hat{f}_q - f_q \right) - \left(K_q - \dot{\phi}_q \right) \left| S_q \right| \tag{4.16}$$

Since the boundary layer is invariant [89], once the trajectory reaches the boundary layer within finite time, it remains within this boundary layer. Outside of this boundary layer, $\text{sgn}(S)$ is same as $\text{sat}\left(\frac{S}{\phi}\right)$. Moreover, outside of this boundary layer $S > \phi$ hence, $S - \phi$ should decrease as $t \to \infty$.

Therefore, if the time derivative of S is considered, then the time derivative of ϕ should also be considered. In other words, the condition of stability outside the boundary layer is expressed as

$$0.5\frac{d}{dt}S^2 \leq \left(\dot{\phi} - \eta\right)|S|. \tag{4.17}$$

Therefore it can be understood that if $\mathrm{sgn}(S)$ is used, then the condition on stability would be $0.5\frac{d}{dt}S^2 \leq -\eta|S|$, now due to the use of $\mathrm{sat}\left(\frac{S}{\phi}\right)$, the extra condition on stability is $\left(\dot{\phi} - \eta\right)|S|$ (4.17). Hence, for a stable system the following condition should satisfy

$$\dot{V} \leq \left(\dot{\phi}_d - \eta_d\right)|S_d| + \left(\dot{\phi}_q - \eta_q\right)\left|S_q\right| \tag{4.18}$$

If, K_d and K_q are replaced as $K_d = F_d + \eta_d$ and $K_q = F_q + \eta_q$, then (4.16) can be further expressed as

$$\dot{V} = \underbrace{S_d\left(\hat{f}_d - f_d\right) - F_d|S_d|}_{x_d} + \left(\dot{\phi}_d - \eta_d\right)|S_d| + \underbrace{S_q\left(\hat{f}_q - f_q\right) - F_q\left|S_q\right|}_{x_q} + \left(\dot{\phi}_q - \eta_q\right)\left|S_q\right| \tag{4.19}$$

It is evident from (4.19) that, if S_d and $\left(\hat{f}_d - f_d\right)$ has the same sign and if $F_d = \left|\hat{f}_d - f_d\right|$, then $x_d = 0$; similarly, if S_q and $\left(\hat{f}_q - f_q\right)$ has the same sign and if $F_q = \left|\hat{f}_q - f_q\right|$, then $x_q = 0$. Hence, it can be said that if F_d and F_q is chosen sufficiently large, then $x_d \leq 0$ and $x_q \leq 0$ and the stability condition (4.18) is satisfied. Therefore, the control law given by (4.8) stabilize the system defined by (4.3).

4.2.3 Choice of gains

The terms F_d and F_q are unknown, hence, to ensure the stability condition (4.18) F_d and F_q are defined as

$$\begin{aligned} F_d &= \left|-\frac{\hat{r}_f}{\hat{L}_f}i_d + \hat{\omega}_g i_q + \frac{v_d}{\hat{L}_f}\right| \\ F_q &= \left|-\frac{\hat{r}_f}{\hat{L}_f}i_q - \hat{\omega}_g i_d\right| \quad . \end{aligned} \tag{4.20}$$

Lets,

$$\begin{aligned} \lambda_d &= \frac{K_d - \dot{\phi}_d}{\phi_d} \\ \lambda_q &= \frac{K_q - \dot{\phi}_q}{\phi_q}. \end{aligned} \tag{4.21}$$

therefore, the expression of ϕ_d and ϕ_q can be written as

$$\begin{aligned} \phi_d &= \frac{K_d - \dot{\phi}_d}{\lambda_d} \\ \phi_q &= \frac{K_q - \dot{\phi}_q}{\lambda_q} \end{aligned} \tag{4.22}$$

where, $\lambda_d, \lambda_q > 0$ are the chosen gains.

The expression (4.22) can be rewritten as

$$\begin{aligned} \dot{\phi}_d + \lambda_d \phi_d &= K_d \\ \dot{\phi}_q + \lambda_q \phi_q &= K_q \end{aligned} \tag{4.23}$$

The expression (4.23), looks like a first order low pass filter with a time constant of the order $\frac{1}{\lambda_d}$ and $\frac{1}{\lambda_q}$. Neglecting the time constant, it can be said very loosely that, $\phi_d \approx \frac{K_d}{\lambda_d}$ and $\phi_q \approx \frac{K_q}{\lambda_q}$. Now, assuming η_d, η_q are very small, it can be said that $K_d \approx F_d$ and $K_q \approx F_q$. Therefore, the expression of ϕ_d and ϕ_q can be rewritten as

$$\begin{aligned} \phi_d &\approx \frac{K_d}{\lambda_d} \approx \frac{F_d}{\lambda_d} \\ \phi_q &\approx \frac{K_q}{\lambda_q} \approx \frac{F_q}{\lambda_q} \end{aligned} \tag{4.24}$$

The gains can be chosen in a straight forward manner as it has been already mentioned that $\eta_d, \eta_q > 0$ and $\lambda_d, \lambda_q > 0$. During the derivation of (4.24), it is assumed that the η_d and η_q are very small; hence, after some trial run the values are decided and chosen as $\eta_d, \eta_q = 0.02$. For λ_d and λ_q, any positive number would not serve the purpose. It is observed that the high value of λ_d and λ_q produce large overshoot, consequently delaying the settling time, in addition to that, output oscillation is observed for the high values. After some trial run the values are decided and chosen as $\lambda_d, \lambda_q = 1000$. During the trial runs, attention has been given to find out the controller gains that meet the control objective while fulfilling the different performance criteria like fast convergence, low overshoot, and high accuracy. The schematic diagram of the structure of the controller is given in Figure 4.2.

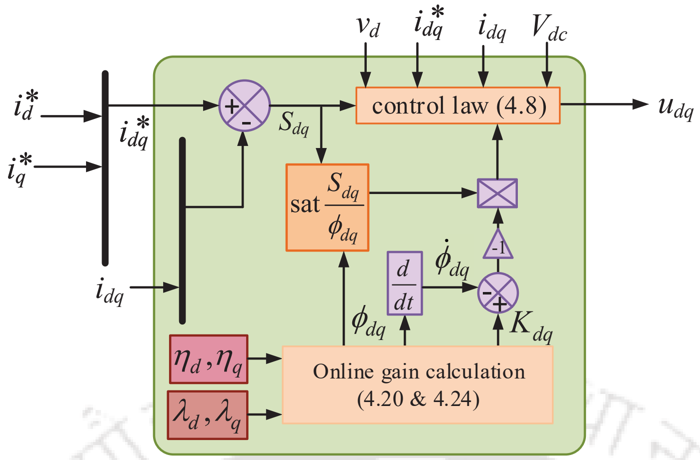

Figure 4.2: Schematic diagram of the controller.

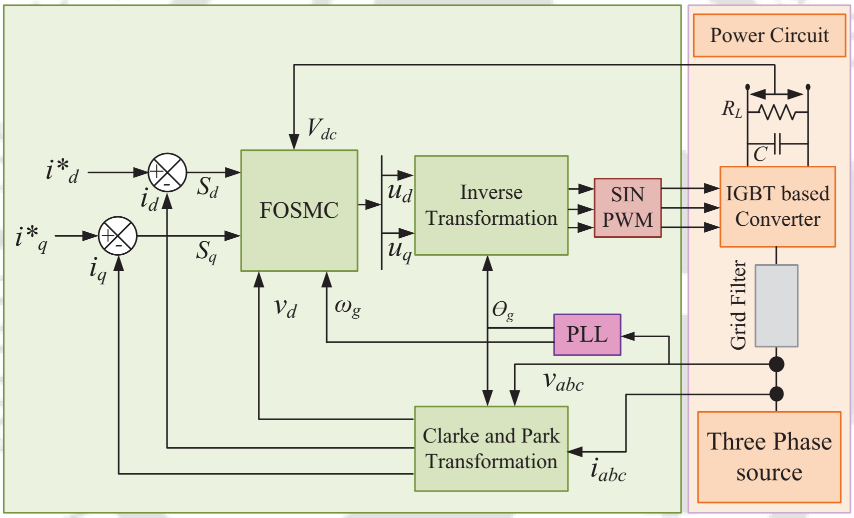

Figure 4.3: Schematic diagram of the total system.

4.3 Simulation results and discussion

The simulation study is done by setting the three-phase grid voltage at 230 V phase-neutral, 50 Hz, the nominal values of the grid inductance L_f is taken as 15 mH, and the parasitic resistance is taken as 0.5 Ω. The DC load resistance is chosen as 200 Ω, and the DC bus capacitance is chosen as 2350 μF. Step changes are employed to the d-axis and q-axis currents to evaluate the dynamic performance of the controller, and the performances curves are shown below (Figures 4.4-4.5). The schematic diagram of the total system is presented in Figure 4.3. In addition to these tests, the performance of the designed controller is also evaluated under the step-change in the grid filter parameters.

4.3.1 First case: step change in *d*-axis reference current

For this test, the *q*-axis current (i_q^*) is fixed at 0 A and a step change of 5 A (from 6 A to 11 A) is employed to the *d*-axis reference current (i_d^*) at 3 s. It can be observed from Figure 4.4(a) that the measured current tracks the reference current within 5 ms. Since $i_q^* = 0$, the phase-a voltage v_a and phase-a current i_a are in same phase (Figure 4.4(b)). Since i_d^* is changed, a change is also observed at 3 s for the DC bus voltage (V_{dc}) (Figure 4.4(c)).

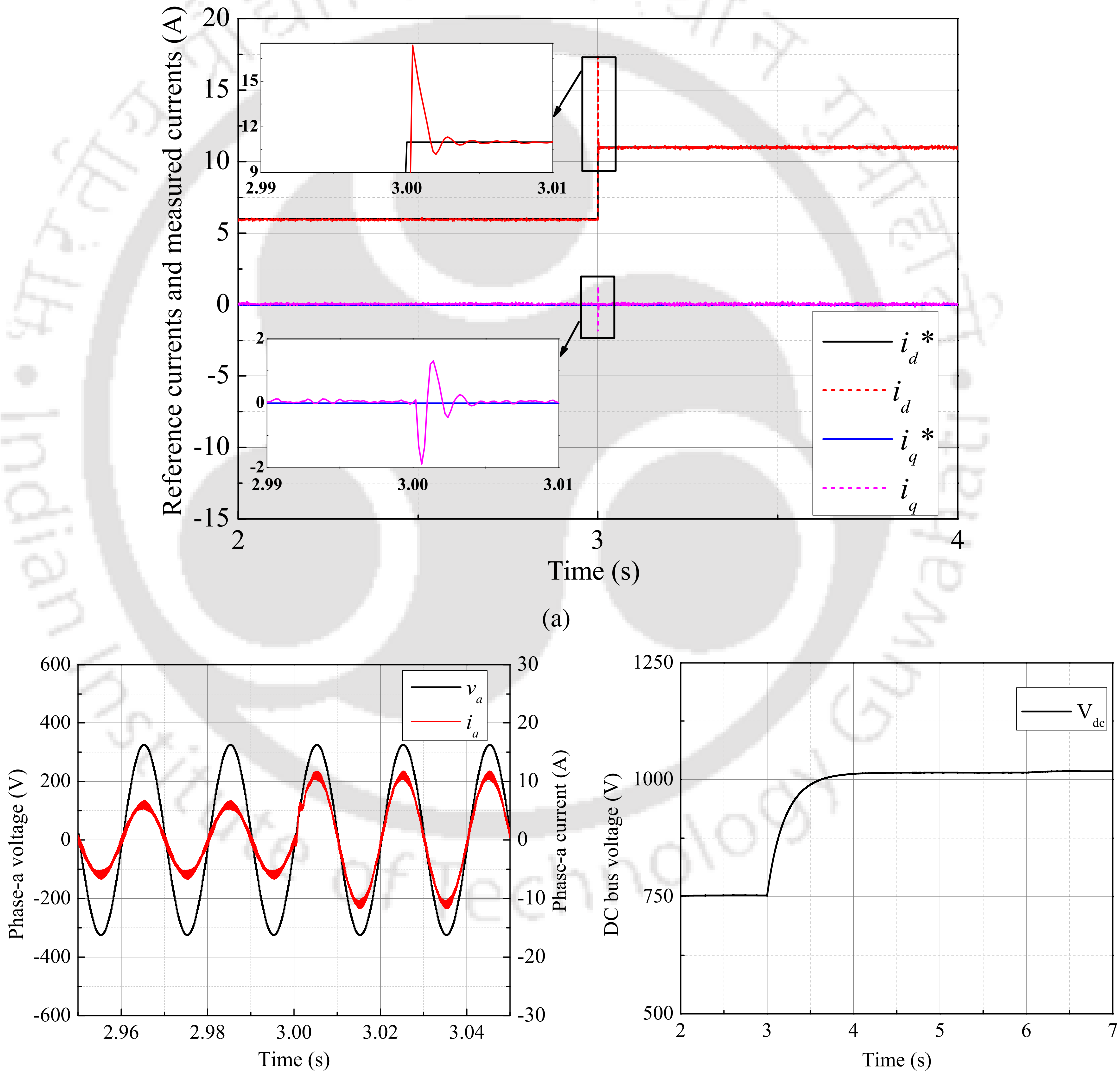

(a)

(b)

(c)

Figure 4.4: Simulation result regarding the performance of the proposed FOSMC current controller under the step change in i_d^* from 6 A to 11 A; (a) Plots of *dq*- axis currents. (b) Plots of phase-a voltage and current. (c) Plot of DC bus voltage.

4.3.2 Second case: step change in q-axis reference current

For this test, the d-axis current (i_d^*) is fixed at 11 A and a step change of 5 A (from 0 A to -5 A) is employed to the q-axis reference current (i_q^*) at 6 s. It can be observed from Figure 4.5(a) that the measured current tracks the reference current within 5 ms. Since i_q^*= -5 A, the phase-a voltage v_a and phase-a current i_a has phase difference (Figure 4.5(b)). Since i_d^* is kept at constant value, the DC bus voltage (Figure 4.5(c)) is unchanged during the transition in i_q^*.

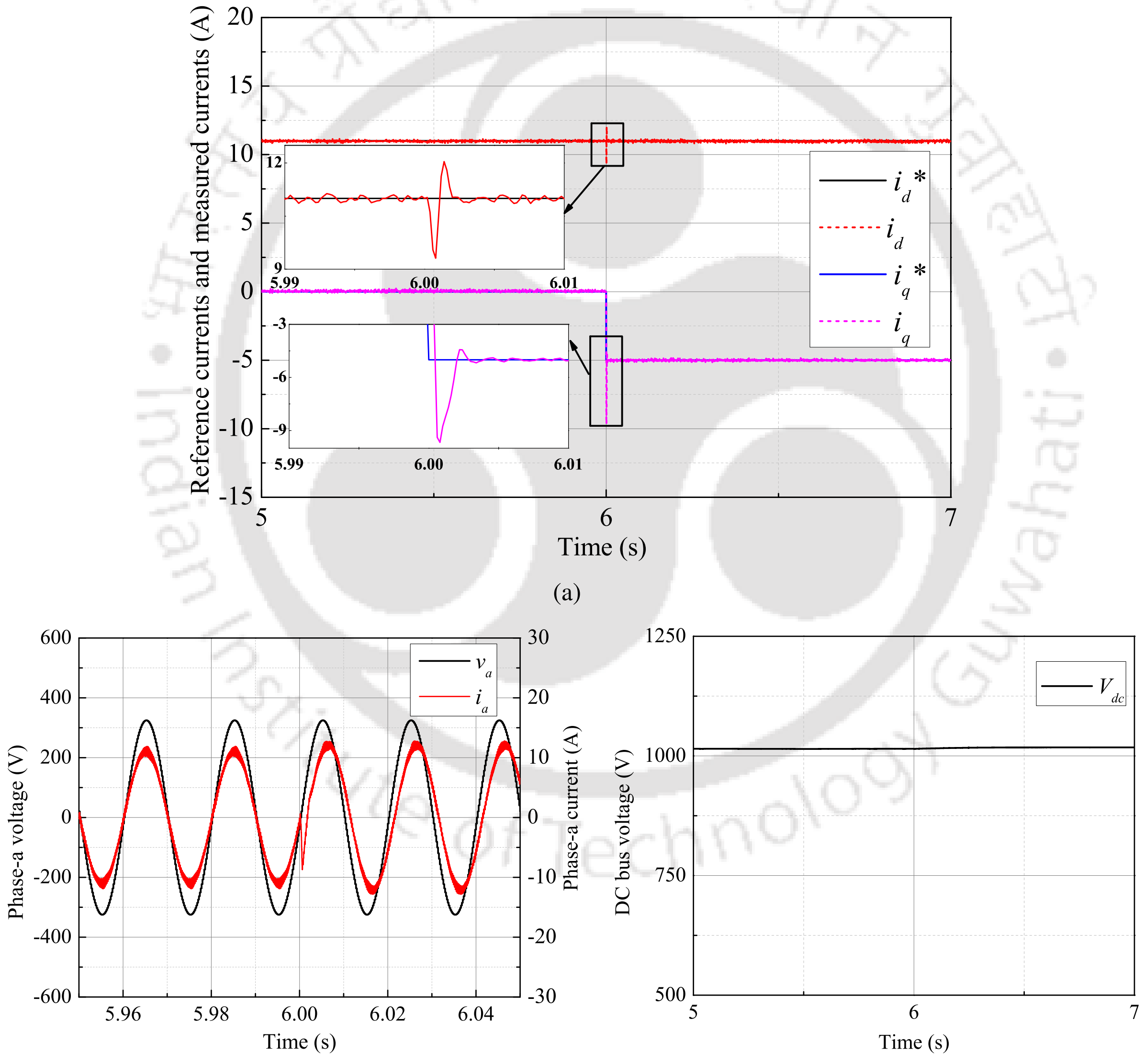

(a)

(b)

(c)

Figure 4.5: Simulation result regarding the performance of the proposed FOSMC current controller under the step change in i_q^* from 0 A to -5 A; (a) Plots of dq- axis currents. (b) Plots of phase-a voltage and current. (c) Plot of DC bus voltage.

4.3.3 Current controller performance under the step change in grid filter parameters

For this test, the *d*-axis current (i_d^*) is fixed at 11 A and a step change is employed to the filter inductance (20 mH to 10 mH) and parasitic resistance (1 Ω to 0.5 Ω) associated it at 4 s (Figure 4.6(a)). It can be observed from Figure 4.6 that the measured current tracks the reference current perfectly without any problem.

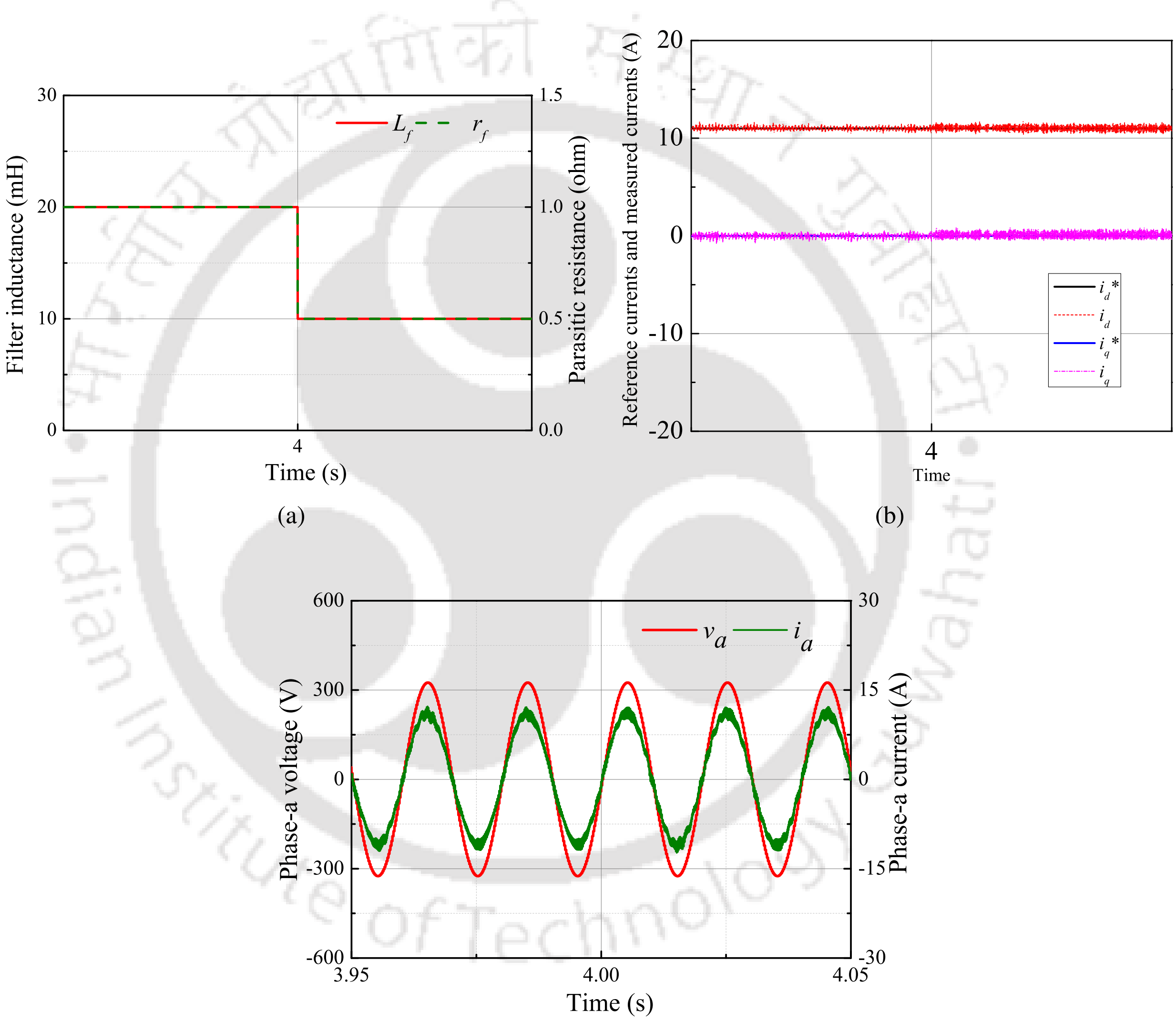

(a)

(b)

(c)

Figure 4.6: Simulation result regarding the performance of the proposed FOSMC current controller under the step change in grid filter parameters; (a) Plots of filter parameters. (b) Plots of *dq*- axis currents. (c) Plots of phase-a voltage and current.

4.4 Experimental results and discussion

The experimental test setup consists of a Semikron make three-phase, four-leg insulated gate bipolar transistor (IGBT) based pulse width modulated (PWM) converter connected with the distribution grid of 50 Hz by means of an auto-transformer. Three 15 mH inductors are used as the passive filters, the nominal value of the parasitic resistance of these inductors are found as 0.5 Ω. The controller algorithm is implemented on a 150 MHz, TMS320F28335 digital signal controller (DSC) kit. The three-phase voltage, current and the DC bus voltage are sensed through Hall-effect sensors. These analogue signals are then sampled at 5 kHz on the DSC kit. The control algorithm runs at 5 kHz, and the converter switching frequency is set at 5 kHz. The dynamic performance of the designed controller is evaluated for two test cases, and the performance curves are given below (Figures 4.7-4.8). The experimental tests are performed by setting the grid voltage as 17 V L-L and by choosing the DC load resistance as 116 Ω.

4.4.1 First case: step change in d-axis reference current

For this test, the q-axis reference current (i_q^*) is set at 0 A and step change is employed in d-axis reference current (i_d^*). i_d^* is changed from 1 A to 2 A, and performance curves are plotted and represented in Figure 4.7. It is observed from Figure 4.7(a) that the i_d tracks the i_d^* within 10 ms without any overshoot. Since i_d is changed from 1 A to 2 A, the DC bus voltage is also changed from 50 V to 60 V approximately. Since $i_q = 0$ A and i_d changes from 1 A to 2 A, the peak value of phase-a current (i_a) also changes from 1 A to 2 A. The time scale is chosen as 100 ms/div for plotting the DC bus voltage (V_{dc}), and dq-axis currents (i_d and i_q). The time scale is chosen as 10 ms/div to plot the phase-a voltage (v_a) and current (i_a). For the plotting of V_{dc}, 20 V/div is chosen, and to plot v_a and i_a, 5 V/div and 1 A/div is chosen respectively.

4.4.2 Second case: step change in q-axis reference current

The d-axis reference current (i_d^*) is set at 1 A and suddenly reference q-axis current (i_q^*) is changed from -1 A to 0 A. From Figure 4.8(a), it is observed that within 10 ms, i_q follows the reference current i_q^*. In addition to that, no overshoot is observed for the measured i_q (Figure 4.8(a)). Corresponding

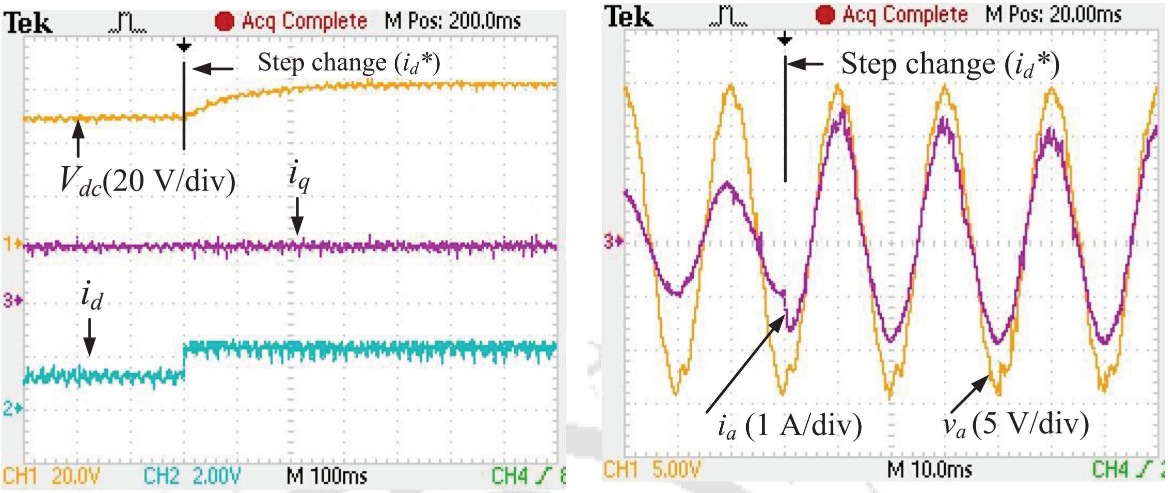

(a) (b)

Figure 4.7: Experimental result regarding the performance of the proposed FOSMC current controller under the step change in i_d^* from 1 A to 2 A; (a) Plots dq- axis currents. (b) Plots of phase-a voltage and current.

phase-a voltage (v_a) and current (i_a) are shown in Figure 4.8(b). It is observed from Figure 4.8(b) that, as soon as the i_q^* changes from -1 A to 0 A, the phase-a current (i_a) aligned itself to the phase-a voltage (v_a). Thus, a unity power factor operation of the power converter is achieved. The time scale is chosen as 100 ms/div to plot V_{dc}, i_d and i_q. The time scale is chosen as 10 ms/div to plot v_a and i_a. For the plotting of V_{dc}, 20 V/div is chosen, and to plot v_a and i_a , 5 V/div and 1 A/div is chosen respectively.

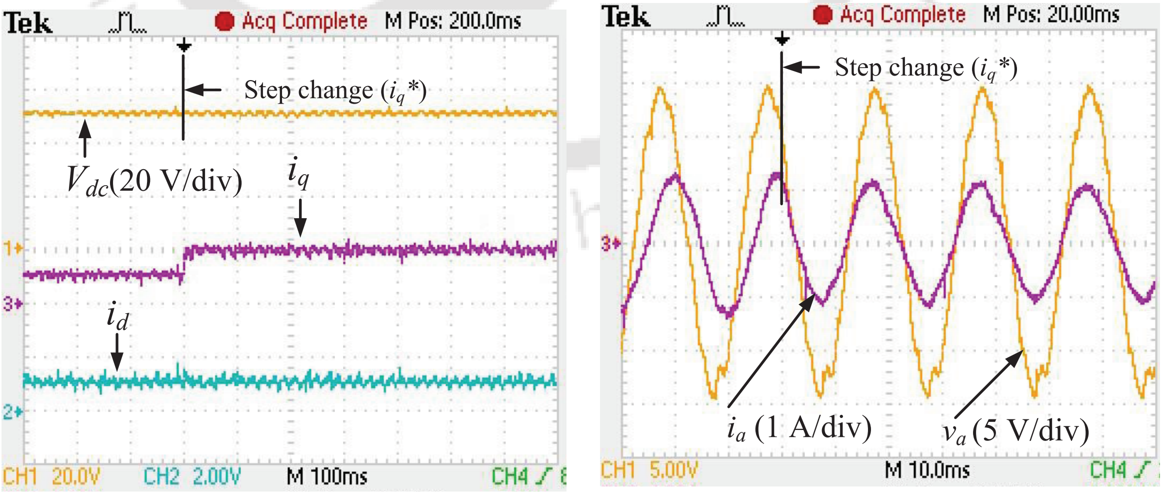

(a) (b)

Figure 4.8: Experimental result regarding the performance of the proposed FOSMC current controller under the step change in i_q^* from - 1 A to 0 A; (a) Plots dq- axis currents. (b) Plots of phase-a voltage and current.

4.5 Summary

A smooth robust current controller is proposed to control the grid currents of the GSC. Since fundamentally sliding mode control (SMC) based methods have the problem of chattering; hence, this work proposed a modified control law to mitigate the chattering effect. From the simulation results, it is observed that the chattering is absent in the output curves of i_d and i_q. The derivation of the controller, along with the stability analysis, are provided in a systematical way. In addition to that, the Lyapunov method is utilized to find the sliding gains for the controller. It can be observed from both the simulation and experimental results that the control algorithm could meet its control objectives while fulfilling the various performance criteria. The transient response of the proposed controller is found very promising.

5

Development of a robust observer in the form of a first-order sliding mode observer (FOSMO) for the rotor speed and position estimation of DFIG

Contents

5.1 Introduction

This Chapter includes sensorless/encoderless voltage and frequency control of a standalone doubly-fed induction generator (DFIG) based wind energy conversion system (WESC). The work presented in this Chapter proposes a new estimator/observer and evaluates its performances by controlling the terminal voltage of a standalone DFIG system through voltage loop control. The proposed speed estimator is designed based on the sliding mode observer (SMO) technique, which makes the estimation algorithm robust under parametric variations and external disturbances. The designed observer compute the rotor position directly by integrating the estimated speed. The proposed observer requires the measurement of stator voltage and current for estimating the speed. Stator current and rotor flux are used as the states for the designed observer. An important feature of the designed observer is that the design procedure does not require any mechanical parameters of the DFIG system, which makes the observer design independent of mechanical parameters. Lyapunov stability criteria are used to derive the sliding gains for the observer, which makes the observer stable. Simulation and experimental results are presented to show the efficacy of the designed observer in terms of high accuracy, and fast convergence rate under different steady-state and dynamic conditions. The estimated rotor speed and position are utilized in real-time to control the magnitude of the stator voltage of a standalone DFIG system, which validates the performance of the observer.

5.2 Dynamic model of the DFIG

The dynamic model of the DFIG is expressed in stationary reference frame ($\alpha\beta$) considering stator currents and rotor fluxes as the states [6]. The derivation of the dynamic model is provided in Appendix B.

$$\left.\begin{aligned}
\frac{di_{\alpha s}}{dt} &= ai_{\alpha s} + c\psi_{\alpha r} + d\omega_r\psi_{\beta r} + bv_{\alpha s} - hv_{\alpha r} \qquad &\text{(a)}\\
\frac{di_{\beta s}}{dt} &= ai_{\beta s} - d\omega_r\psi_{\alpha r} + c\psi_{\beta r} + bv_{\beta s} - hv_{\beta r} \qquad &\text{(b)}\\
\frac{d\psi_{\alpha r}}{dt} &= gi_{\alpha s} - f\psi_{\alpha r} - \omega_r\psi_{\beta r} + v_{\alpha r} \qquad &\text{(c)}\\
\frac{d\psi_{\beta r}}{dt} &= gi_{\beta s} + \omega_r\psi_{\alpha r} - f\psi_{\beta r} + v_{\beta r} \qquad &\text{(d)}
\end{aligned}\right\} \tag{5.1}$$

where, $v_{\alpha s}$ and $v_{\beta s}$ are the stator voltages, $i_{\alpha s}$ and $i_{\beta s}$ are the stator currents, $\psi_{\alpha r}$ and $\psi_{\beta r}$ are the rotor fluxes and the rotor voltages are expressed as $v_{\alpha r}$ and $v_{\beta r}$.

The parameters related to the dynamic model (5.1) are defined as $a = -\left(\frac{R_s}{\sigma L_s} + \frac{L_m^2}{\sigma L_s \tau_r L_r'}\right)$, $b = \frac{1}{\sigma L_s}$, $c = \frac{1}{e\tau_r}$, $d = \frac{1}{e}$, $e = \frac{\sigma L_s L_r'}{L_m}$, $f = \frac{1}{\tau_r}$, $g = \frac{L_m}{\tau_r}$, $h = \frac{L_m}{\sigma L_s L_r'}$, $\tau_r = \frac{L_r}{R_r'}$, $\sigma = 1 - \frac{L_m^2}{L_s L_r'}$. The stator and rotor resistances are expressed as R_s and R_r', stator and rotor inductances are expressed as L_s and L_r' and the mutual inductance is expressed as L_m. The leakage factor is considered as σ. The detailed dynamical model of the DFIG is shown in Appendix B-(B.12).

The rotor voltages are calculated directly using the expression given (5.2) below

$$\vec{v}_r = e^{j\theta_r}\vec{v}_r^{\,sl} = \vec{m}_r^{\,sl} n \frac{V_{dc}}{2} \tag{5.2}$$

where θ_r is the rotor position, $\vec{v}_r = \begin{bmatrix} v_{\alpha r} & v_{\beta r} \end{bmatrix}^T$ is the rotor voltage vector in stator frequency, $\vec{v}_r^{\,sl} = \begin{bmatrix} v_{\alpha r}^{sl} & v_{\beta r}^{sl} \end{bmatrix}^T$ is the rotor voltage vector in slip frequency, n is the stator to rotor turns ratio, V_{dc} is the DC bus voltage across the RSC, and $\vec{m}_r^{\,sl} = \begin{bmatrix} m_{\alpha r}^{sl} & m_{\beta r}^{sl} \end{bmatrix}^T$ is the modulating signal vector in slip frequency. The three-phase stator voltages and currents are measured and transformed into two-phase stationary $\alpha\beta$ reference frame. These transformed voltages and currents are then used to develop the observer model which is discussed in the next section.

5.3 Observer design procedure

In this section the detailed derivation of the robust speed observer in stationary reference frame ($\alpha\beta$) is carried out using the Lyapunov stability criteria.

5.3.1 Observer model

Considering the dynamic model defined in (5.1) an observer model is proposed below (5.3).

$$\left.\begin{aligned}
\frac{d\hat{i}_{\alpha s}}{dt} &= a\hat{i}_{\alpha s} + c\hat{\psi}_{\alpha r} + d\hat{\omega}_r\hat{\psi}_{\beta r} + bv_{\alpha s} - hv_{\alpha r} + \Lambda_1 u_\alpha && \text{(a)}\\
\frac{d\hat{i}_{\beta s}}{dt} &= a\hat{i}_{\beta s} - d\hat{\omega}_r\psi_{\alpha r} + c\hat{\psi}_{\beta r} + bv_{\beta s} - hv_{\beta r} + \Lambda_2 u_\beta && \text{(b)}\\
\frac{d\hat{\psi}_{\alpha r}}{dt} &= g\hat{i}_{\alpha s} - f\hat{\psi}_{\alpha r} - \hat{\omega}_r\hat{\psi}_{\beta r} + v_{\alpha r} - \Lambda_3 u_\alpha && \text{(c)}\\
\frac{d\hat{\psi}_{\beta r}}{dt} &= g\hat{i}_{\beta s} + \hat{\omega}_r\hat{\psi}_{\alpha r} - f\hat{\psi}_{\beta r} + v_{\beta r} - \Lambda_4 u_\beta && \text{(d)}\\
\frac{d\hat{\omega}_r}{dt} &= \lambda\left[d\left(\tilde{i}_{\beta s}\hat{\psi}_{\alpha r} - \tilde{i}_{\alpha s}\hat{\psi}_{\beta r}\right) - \left(\tilde{\psi}_{\beta r}\hat{\psi}_{\alpha r} - \tilde{\psi}_{\alpha r}\hat{\psi}_{\beta r}\right)\right] && \text{(e)}
\end{aligned}\right\} \tag{5.3}$$

where $\hat{i}_{\alpha s}$, $\hat{i}_{\beta s}$, $\hat{\psi}_{\alpha r}$, $\hat{\psi}_{\beta r}$ and $\hat{\omega}_r$ are the estimated quantities, Λ_1, Λ_2, Λ_3, Λ_4 are the gains for the current and flux observers and $\lambda > 0$ is the gain for the speed estimator and $u_\alpha = \text{sgn}(\tilde{i}_{\alpha s})$, $u_\beta = \text{sgn}(\tilde{i}_{\beta s})$, $\tilde{i}_{\alpha s} = \hat{i}_{\alpha s} - i_{\alpha s}$, $\tilde{i}_{\beta s} = \hat{i}_{\beta s} - i_{\beta s}$, $\tilde{\psi}_{\alpha r} = \hat{\psi}_{\alpha r} - \psi_{\alpha r}$ and $\tilde{\psi}_{\beta r} = \hat{\psi}_{\beta r} - \psi_{\beta r}$. The switching function ($\text{sgn}(*)$) can be defined as

$$\text{sgn}\,(*) = \begin{cases} 1, & \text{if } * > 0 \\ -1, & \text{if } * < 0 \end{cases} \tag{5.4}$$

The error dynamics of the stator current and rotor flux can be written as

$$\left.\begin{aligned}
\frac{d\tilde{i}_{\alpha s}}{dt} &= a\tilde{i}_{\alpha s} + c\tilde{\psi}_{\alpha r} + d\hat{\omega}_r\tilde{\psi}_{\beta r} + d\tilde{\omega}_r\hat{\psi}_{\beta r} + \Lambda_1 u_\alpha && \text{(a)}\\
\frac{d\tilde{i}_{\beta s}}{dt} &= a\tilde{i}_{\beta s} - d\hat{\omega}_r\tilde{\psi}_{\alpha r} - d\tilde{\omega}_r\hat{\psi}_{\alpha r} + c\tilde{\psi}_{\beta r} + \Lambda_2 u_\beta && \text{(b)}\\
\frac{d\tilde{\psi}_{\alpha r}}{dt} &= g\tilde{i}_{\alpha s} - f\tilde{\psi}_{\alpha r} - \hat{\omega}_r\tilde{\psi}_{\beta r} - \tilde{\omega}_r\hat{\psi}_{\beta r} - \Lambda_3 u_\alpha && \text{(c)}\\
\frac{d\tilde{\psi}_{\beta r}}{dt} &= g\tilde{i}_{\beta s} + \hat{\omega}_r\tilde{\psi}_{\alpha r} + \tilde{\omega}_r\hat{\psi}_{\alpha r} - f\tilde{\psi}_{\beta r} - \Lambda_4 u_\beta && \text{(d)}
\end{aligned}\right\} \tag{5.5}$$

where $\tilde{\omega}_r = \hat{\omega}_r - \omega_r$. It is to be noted that, for deriving the error equations (5.5) all the DFIG parameters are assumed to be known.

5.3.2 Formulation of the observer gains

A Lyapunov function is chosen subjected to the error dynamics defined in (5.5).

$$V = \frac{1}{2}\tilde{i}_{\alpha s}^{2} + \frac{1}{2}\tilde{i}_{\beta s}^{2} + \frac{1}{2}\tilde{\psi}_{\alpha r}^{2} + \frac{1}{2}\tilde{\psi}_{\beta r}^{2} + \frac{1}{2\lambda}\tilde{\omega}_{r}^{2} \tag{5.6}$$

The time derivative of the Lyapunov function (V) is expressed as

$$\dot{V} = \tilde{i}_{\alpha s}\dot{\tilde{i}}_{\alpha s} + \tilde{i}_{\beta s}\dot{\tilde{i}}_{\beta s} + \tilde{\psi}_{\alpha r}\dot{\tilde{\psi}}_{\alpha r} + \tilde{\psi}_{\beta r}\dot{\tilde{\psi}}_{\beta r} + \frac{\tilde{\omega}_{r}}{\lambda}\frac{d\hat{\omega}_{r}}{dt} \tag{5.7}$$

Since the mechanical dynamics is very slow compared to the electrical dynamics of a DFIG, ω_r is considered as constant in (5.7).

Plugging (5.5) into (5.7) the $\dot{V}$ can be rewritten as

$$\begin{aligned}\dot{V} = {} & \tilde{i}_{\alpha s}\left(a\tilde{i}_{\alpha s} + c\tilde{\psi}_{\alpha r} + d\hat{\omega}_{r}\tilde{\psi}_{\beta r} + d\tilde{\omega}_{r}\hat{\psi}_{\beta r} + \Lambda_{1}u_{\alpha}\right) + \tilde{i}_{\beta s}\left(a\tilde{i}_{\beta s} - d\hat{\omega}_{r}\tilde{\psi}_{\alpha r} - d\tilde{\omega}_{r}\hat{\psi}_{\alpha r} + c\tilde{\psi}_{\beta r} + \Lambda_{2}u_{\beta}\right)\\ & + \tilde{\psi}_{\alpha r}\left(g\tilde{i}_{\alpha s} - f\tilde{\psi}_{\alpha r} - \hat{\omega}_{r}\tilde{\psi}_{\beta r} - \tilde{\omega}_{r}\hat{\psi}_{\beta r} - \Lambda_{3}u_{\alpha}\right) + \tilde{\psi}_{\beta r}\left(g\tilde{i}_{\beta s} + \hat{\omega}_{r}\tilde{\psi}_{\alpha r} + \tilde{\omega}_{r}\hat{\psi}_{\alpha r} - f\tilde{\psi}_{\beta r} - \Lambda_{4}u_{\beta}\right)\\ & + \frac{\tilde{\omega}_{r}}{\lambda}\frac{d\hat{\omega}_{r}}{dt}\end{aligned} \tag{5.8}$$

Replacing, $\frac{d\hat{\omega}_r}{dt}$ into (5.8) from (5.3(e)) and segregating the terms containing $\tilde{\omega}_r$ in (5.8), the (5.8) can be further expressed as

$$\begin{aligned}\dot{V} = {} & \tilde{i}_{\alpha s}\left(a\tilde{i}_{\alpha s} + c\tilde{\psi}_{\alpha r} + d\hat{\omega}_{r}\tilde{\psi}_{\beta r} + \Lambda_{1}u_{\alpha}\right) + \tilde{i}_{\beta s}\left(a\tilde{i}_{\beta s} - d\hat{\omega}_{r}\tilde{\psi}_{\alpha r} + c\tilde{\psi}_{\beta r} + \Lambda_{2}u_{\beta}\right)\\ & + \tilde{\psi}_{\alpha r}\left(g\tilde{i}_{\alpha s} - f\tilde{\psi}_{\alpha r} - \hat{\omega}_{r}\tilde{\psi}_{\beta r} - \Lambda_{3}u_{\alpha}\right) + \tilde{\psi}_{\beta r}\left(g\tilde{i}_{\beta s} + \hat{\omega}_{r}\tilde{\psi}_{\alpha r} - f\tilde{\psi}_{\beta r} - \Lambda_{4}u_{\beta}\right)\\ & + \underbrace{\tilde{\omega}_{r}\left[d\left(\tilde{i}_{\alpha s}\hat{\psi}_{\beta r} - \tilde{i}_{\beta s}\hat{\psi}_{\alpha r}\right) + \left(\tilde{\psi}_{\beta r}\hat{\psi}_{\alpha r} - \tilde{\psi}_{\alpha r}\hat{\psi}_{\beta r}\right)\right]}_{x_{1}}\\ & + \underbrace{\tilde{\omega}_{r}\left[d\left(\tilde{i}_{\beta s}\hat{\psi}_{\alpha r} - \tilde{i}_{\alpha s}\hat{\psi}_{\beta r}\right) - \left(\tilde{\psi}_{\beta r}\hat{\psi}_{\alpha r} - \tilde{\psi}_{\alpha r}\hat{\psi}_{\beta r}\right)\right]}_{x_{2}}\end{aligned} \tag{5.9}$$

The terms x_1 and x_2 cancel each other in (5.9). According to the Lyapunov stability criteria for stability, a positive definite Lyapunov function (V) should have a negative definite first-order derivative ($\dot{V}$). Therefore, to make $\dot{V}$ negative, $\Lambda_1, \Lambda_2, \Lambda_3$ and Λ_4 should be chosen appropriately.

Now, $\tilde{\psi}_{\alpha r}$ and $\tilde{\psi}_{\beta r}$ are unknown, as $\psi_{\alpha r}$ and $\psi_{\beta r}$ are not measurable quantities. To cope with this, let us assume that the current and the flux estimation errors are really small. Thus, it is reasonable to say that $\tilde{i}_{\alpha s} + \tilde{\psi}_{\alpha r} \approx 0$ and $\tilde{i}_{\beta s} + \tilde{\psi}_{\beta r} \approx 0$. Hence, the flux estimation errors can be written in terms of current estimation errors (5.10). Similar type of assumption can be found in [91].

$$\begin{aligned} \tilde{\psi}_{\alpha r} &= -\tilde{i}_{\alpha s} \\ \tilde{\psi}_{\beta r} &= -\tilde{i}_{\beta s} \end{aligned} \tag{5.10}$$

Replacing, $\tilde{\psi}_{\alpha r}$ and $\tilde{\psi}_{\beta r}$ as $-\tilde{i}_{\alpha s}$ and $-\tilde{i}_{\beta s}$ in (5.9), the (5.9) can be further expressed as

$$\begin{aligned} \dot{V} = \tilde{i}_{\alpha s}\left(a\tilde{i}_{\alpha s} - c\tilde{i}_{\alpha s} - d\hat{\omega}_r\tilde{i}_{\beta s} + \Lambda_1 u_\alpha\right) + \tilde{i}_{\beta s}\left(a\tilde{i}_{\beta s} + d\hat{\omega}_r\tilde{i}_{\alpha s} - c\tilde{i}_{\beta s} + \Lambda_2 u_\beta\right) \\ +\tilde{i}_{\alpha s}\left(-g\tilde{i}_{\alpha s} - f\tilde{i}_{\alpha s} - \hat{\omega}_r\tilde{\psi}_{\beta r} + \Lambda_3 u_\alpha\right) + \tilde{i}_{\beta s}\left(-g\tilde{i}_{\beta s} + \hat{\omega}_r\tilde{i}_{\alpha s} - f\tilde{i}_{\beta s} + \Lambda_4 u_\beta\right) \end{aligned} \tag{5.11}$$

It is evident from (5.11) that the terms, $a\tilde{i}_{\alpha s}$, $a\tilde{i}_{\beta s}$ are negative as a itself is negative and the terms $c\tilde{i}_{\alpha s}$, $c\tilde{i}_{\beta s}$, $g\tilde{i}_{\alpha s}$, $g\tilde{i}_{\beta s}$, $f\tilde{i}_{\alpha s}$ and $f\tilde{i}_{\beta s}$ are negative. Hence, for the calculation of the current and flux observer gains, these terms are not considered. Therefore, to make the $\dot{V}$ negative, the following conditions (5.12) are required to satisfy.

$$\left.\begin{aligned} \Lambda_1 &< -\left|-d\hat{\omega}_r\tilde{i}_{\beta s}\right| \\ \Lambda_2 &< -\left|d\hat{\omega}_r\tilde{i}_{\alpha s}\right| \\ \Lambda_3 &< -\left|-\hat{\omega}_r\tilde{i}_{\beta s}\right| \\ \Lambda_4 &< -\left|\hat{\omega}_r\tilde{i}_{\alpha s}\right| \end{aligned}\right\} \tag{5.12}$$

As the system will start from zero states, the following gains (5.13) are chosen to fulfil the inequalities given by expression (5.12).

$$\left.\begin{aligned} \Lambda_1 &= -\delta_1 - \left|-d\hat{\omega}_r\tilde{i}_{\beta s}\right| \\ \Lambda_2 &= -\delta_2 - \left|d\hat{\omega}_r\tilde{i}_{\alpha s}\right| \\ \Lambda_3 &= -\delta_3 - \left|-\hat{\omega}_r\tilde{i}_{\beta s}\right| \\ \Lambda_4 &= -\delta_4 - \left|\hat{\omega}_r\tilde{i}_{\alpha s}\right| \end{aligned}\right\} \tag{5.13}$$

where, $\delta_i > 0$ and $i = 1 \ldots 4$.

It has been already discussed that the flux estimation errors $\tilde{\psi}_{\alpha r}$ and $\tilde{\psi}_{\beta r}$ are unknown and assumed very small. Therefore, the proposed speed estimation dynamics given by (5.3(e)) can be modified as

$$\frac{d\hat{\omega}_r}{dt} = \lambda\left[d\left(\tilde{i}_{\beta s}\hat{\psi}_{\alpha r} - \tilde{i}_{\alpha s}\hat{\psi}_{\beta r}\right)\right] \tag{5.14}$$

which implies that

$$\hat{\omega}_r = \lambda \int \left[d\left(\tilde{i}_{\beta s}\hat{\psi}_{\alpha r} - \tilde{i}_{\alpha s}\hat{\psi}_{\beta r}\right)\right] dt \tag{5.15}$$

Further, to improve the dynamic behavior of the speed estimator, a proportional term is added, and the speed estimation equation (5.15) can be rewritten as

$$\hat{\omega}_r = k\left[d\left(\tilde{i}_{\beta s}\hat{\psi}_{\alpha r} - \tilde{i}_{\alpha s}\hat{\psi}_{\beta r}\right)\right] + \lambda \int \left[d\left(\tilde{i}_{\beta s}\hat{\psi}_{\alpha r} - \tilde{i}_{\alpha s}\hat{\psi}_{\beta r}\right)\right] dt \tag{5.16}$$

where $k > 0$ and $\lambda > 0$ are the proportional and integral gains for the designed speed observer respectively.

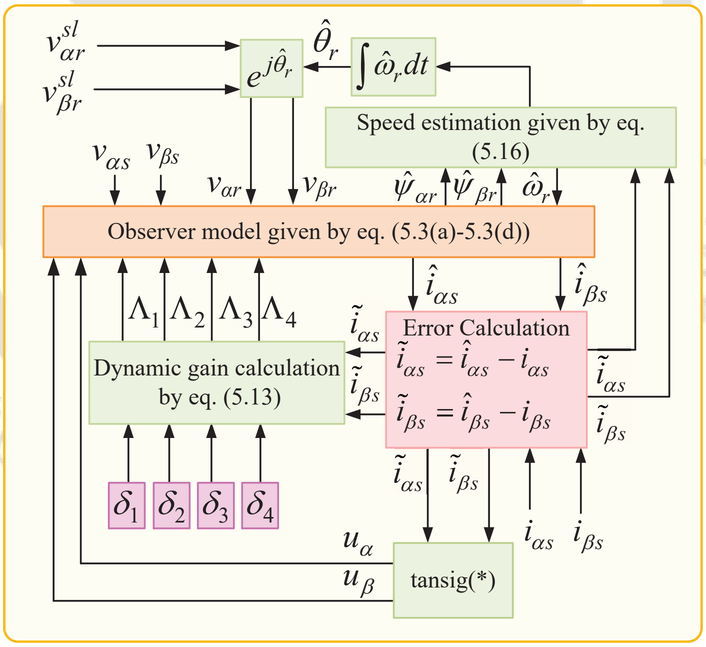

Figure 5.1: Schematic diagram of the proposed FOSMO observer.

The schematic diagram of the designed observer is presented in Figure 5.1. The different chosen gains (δ_i, k and λ) are provided in Table 5.1. In the observer equations (5.3(a)-5.3(d)), the sign function $\left(\text{sgn}\left(\tilde{i}_{\alpha s}\right)\right.$ and $\left.\text{sgn}\left(\tilde{i}_{\beta s}\right)\right)$ is replaced with a tan-sigmoid function to minimize the chattering effect, which is a well-known solution for countering chattering effect, where the tan-sigmoid function can be defined as

$$\text{tansig}(*) = \frac{2}{1 + \mathrm{e}^{-2*}} - 1 \tag{5.17}$$

Table 5.1: Observer gains.

Gains	δ_i	k	λ
Simulation	10	80	850
Hardware	10	60	600

5.4 Sensorless voltage and frequency control

The reference angular frequency (ω_s^*) of the stator voltage is the summation of the angular slip-frequency ($\hat{\omega}_{sl}$) and the estimated rotor speed ($\hat{\omega}_r$) available from the designed speed observer.

$$\omega_s^* = \hat{\omega}_r + \hat{\omega}_{sl} \implies \hat{\omega}_{sl} = \omega_s^* - \hat{\omega}_r \tag{5.18}$$

Dividing both side of (5.18) by $\left(\frac{2}{pi}\right)$, the relationship between different frequencies is expressed as

$$\hat{f}_{sl} = f_s^* - \hat{f}_r \tag{5.19}$$

where f_s^* is the reference frequency of the stator voltage, f_{sl} is the rotor current frequency or slip frequency and $\hat{f}_r$ is the rotor frequency related to the estimated rotor speed.

Integrating both side of (5.18), the slip position is expressed as

$$\int \hat{\omega}_{sl} dt = \int \omega_s^* dt - \int \hat{\omega}_r dt \Rightarrow \hat{\theta}_{sl} = \theta_s^* - \hat{\theta}_r. \tag{5.20}$$

This $\hat{\theta}_{sl}$ is used to transform the rotor currents and modulating voltages.

For a particular speed and load, the stator voltage amplitude is proportional to the rotor current amplitude and frequency (f_{sl}). Hence, the magnitude of the measured stator voltage vector is computed from the orthogonal components in the $\alpha\beta$ frame. The error between the reference magnitude and the computed magnitude is passed through a PI controller. The output signal of the PI controller is considered as the reference rotor current magnitude. Since the DFIG is operating in stand-alone mode, hence the magnetization is done through the rotor. Therefore a negative phase angle (∠-0.85 rad) is chosen as the rotor current phase reference. The polar form of the rotor current vector is further transformed into a rectangular form and compared with the measured rotor current in *dq* frame, and the errors are passed through two PI controllers. The output of the two PI controllers is the reference rotor voltages for the RSC. Figure 5.2 represents the experimental schematic diagram of the sensorless voltage control strategy. The different parameters of the controller are provided in Table 5.2.

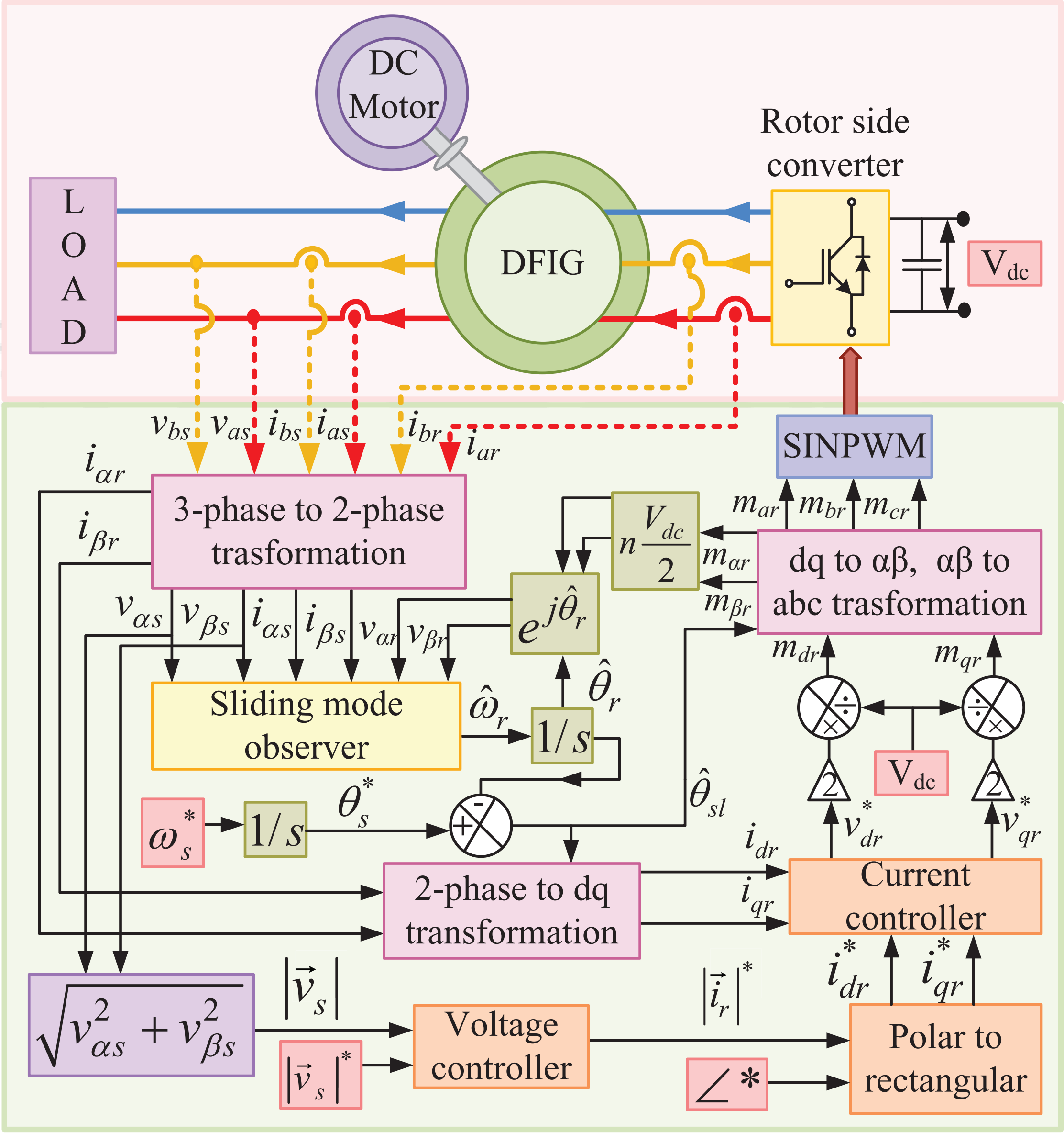

Figure 5.2: Schematic diagram of the experimental system.

Table 5.2: Controller gains.

Gains	k_p	k_i
Voltage controller	1.1	0.0001
Current controllers	15	300

5.5 Simulation results and discussion

A rigorous simulation study is done in Matlab/Simulink to understand the working of the sensorless operation of the DFIG in standalone mode. The performance of the designed observer is evaluated over the typical operating speed range (±30% around the synchronous speed) of a DFIG [6]. The observer is simulated for the speed of 220 rad/s to 410 rad/s (±30% around the synchronous speed) and found working seamlessly for different dynamic conditions imposed on it. The simulation results are provided below (Figures 5.3-5.5).

5.5.1 Dynamic performance of the proposed FOSMO observer under the step change in reference speed

The dynamic performance of the observer is evaluated for a step change in reference speed of 30 rad/s at the interval of 1 s, and the performance curve is shown in Figure 5.3. The estimated speed catches (±0.5% of the reference speed) the reference speed within 200 ms approximately. At 8 s a step change of 10 rad/s is employed, where the speed suddenly changes from 400 rad/s to 410 rad/s and the estimated speed catches the reference speed within 200 ms approximately.

5.5.2 Performance of the proposed FOSMO observer under the ramp change in reference speed

Observer performance is evaluated for a ramp type of speed change, and the performance curve is shown in Figure 5.4. The designed observer exhibits excellent performance under the ramp change of the speed, and the estimated speed follows the reference speed quiet accurately during ramp change in speed. From 2 s to 4 s the speed ramps up from 250 rad/s to 350 rad/s with a positive slope and from 6 s to 8 s the speed ramps down from 350 rad/s to 250 rad/s.

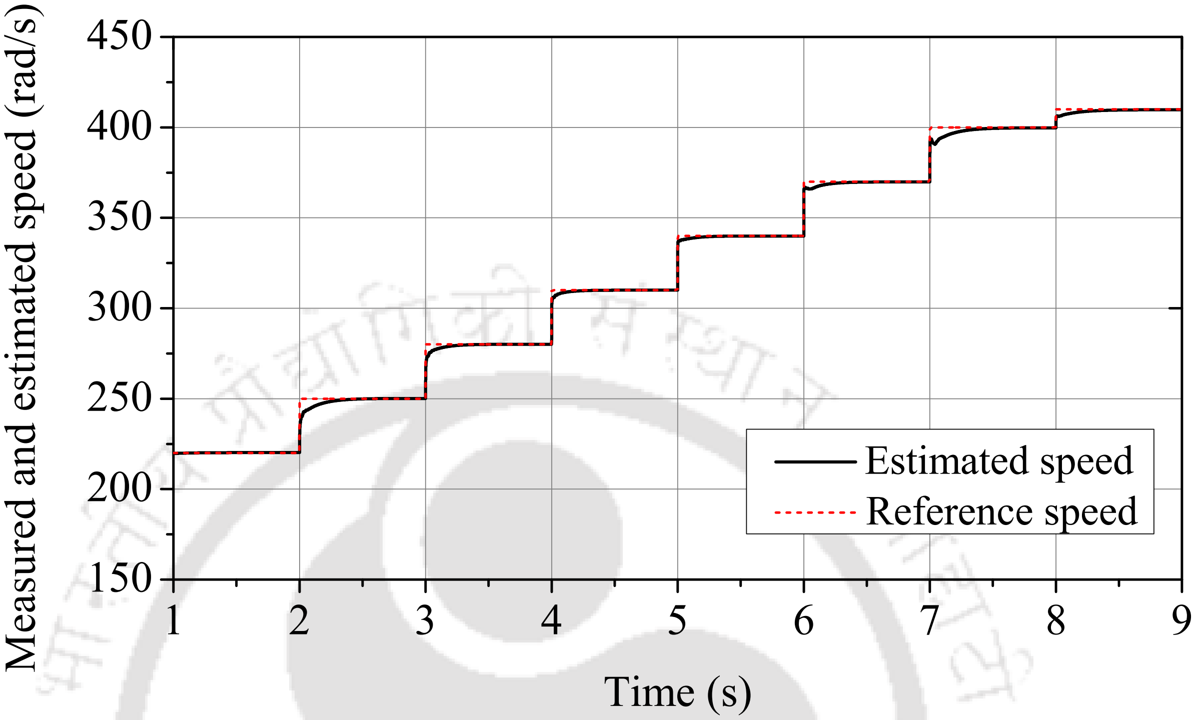

Figure 5.3: Simulation result regarding the performance of the proposed FOSMO observer under the step change in reference speed.

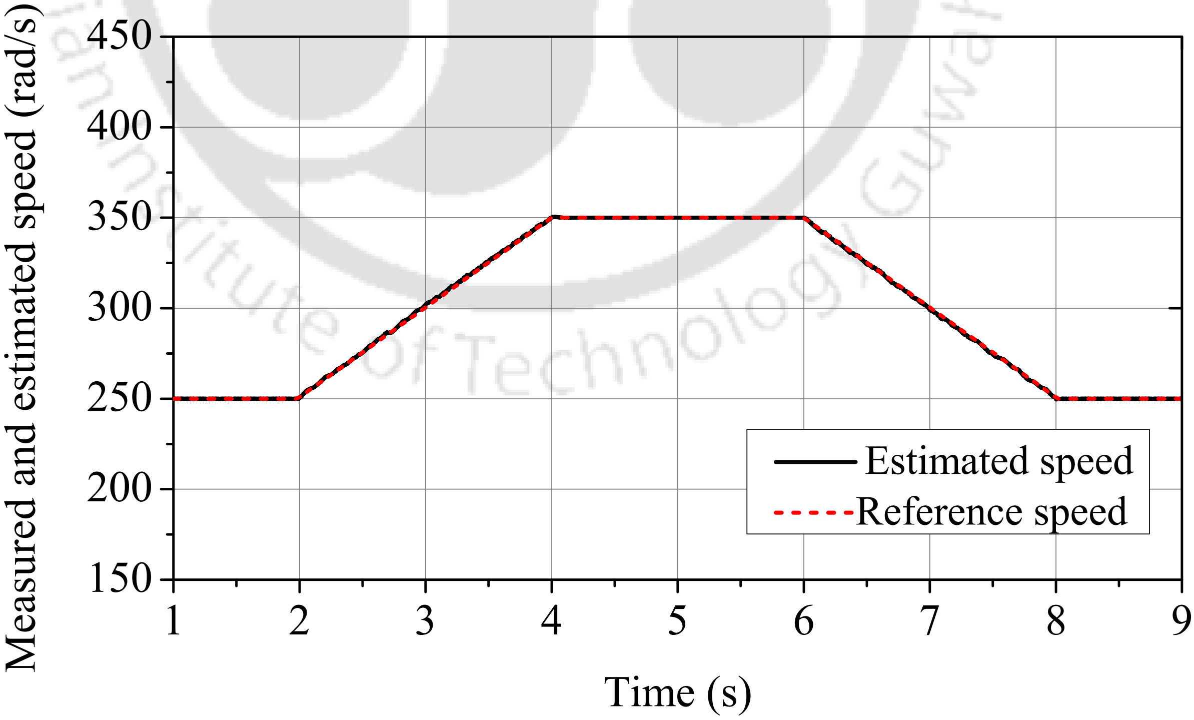

Figure 5.4: Simulation result regarding the performance of the proposed FOSMO observer during ramp-change in reference speed.

5.5.3 Performance of the proposed FOSMO observer under the step change in mutual inductance

Since the mutual inductance is the most significant parameter of the DFIG, the variation of it greatly affects the speed estimation algorithm [70]. Observer performance is evaluated under the step change in mutual inductance L_m, and the performance curves are shown in Figure 5.5. The designed observer works fine under the change of mutual inductance L_m, and the estimated speed follows the reference speed quiet accurately. At 3 s the L_m is changed from 365 mH to 182.5 mH, i.e. 50% of the nominal value, while the machine runs at 250 rad/s. The speed estimation error goes to zero within 100 ms, thus proving the efficacy of the designed observer under the parametric variations.

5.6 Experimental results and discussion

The effectiveness of the designed observer with the sensorless voltage control is validated by implementing it in the laboratory test setup. The test setup consists of a 3-hp wound rotor induction machine used as a DFIG coupled with a 3-hp DC motor. Four current sensors are used to sense the stator and rotor currents, respectively. Three voltage sensors are used to sense the stator voltages and DC link voltage, respectively. A 150 MHz, TMS320F28335 digital signal controller (DSC) kit is used to implement the sensorless voltage control scheme for the DFIG. The observer and the controller run at 5 kHz while the converter's PWM frequency is set as 2 kHz. Steady-state performance of the observer is tested for the speeds 209.5 rad/s (1000 rpm), 293.5 rad/s (1400 rpm) and 331.2 rad/s (1580 rpm) approximately. The dynamic performance of the observer is evaluated near the synchronous speed (314.159 rad/s or 1500 rpm) by applying a sudden step change in armature voltage of the DC motor, and the speed goes supersynchronous to subsynchronous region. The experimental setup of the DFIG system is represented in Figure 5.6. The picture of the full setup is given in the Appendix A (Figure A.2). Due to the low maximum speed limit of the DC motor coupled with the DFIG, the maximum speed range is restricted to +5.5% above the synchronous speed approximately.

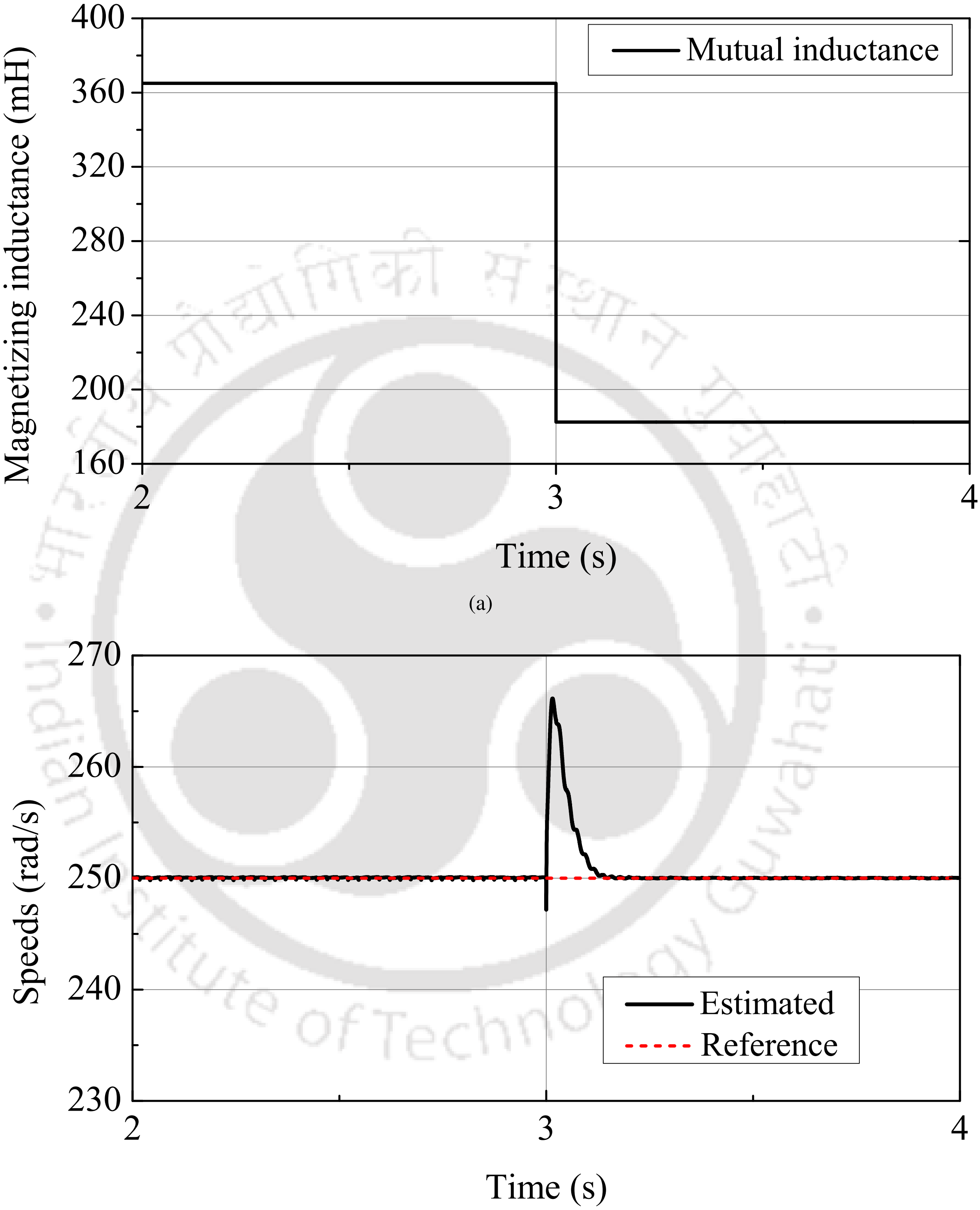

(a)

(b)

Figure 5.5: Simulation result regarding the performance of the proposed FOSMO observer during step change in mutual inductance (a) Step change in mutual inductance (50%). (b) Reference and estimated speed.

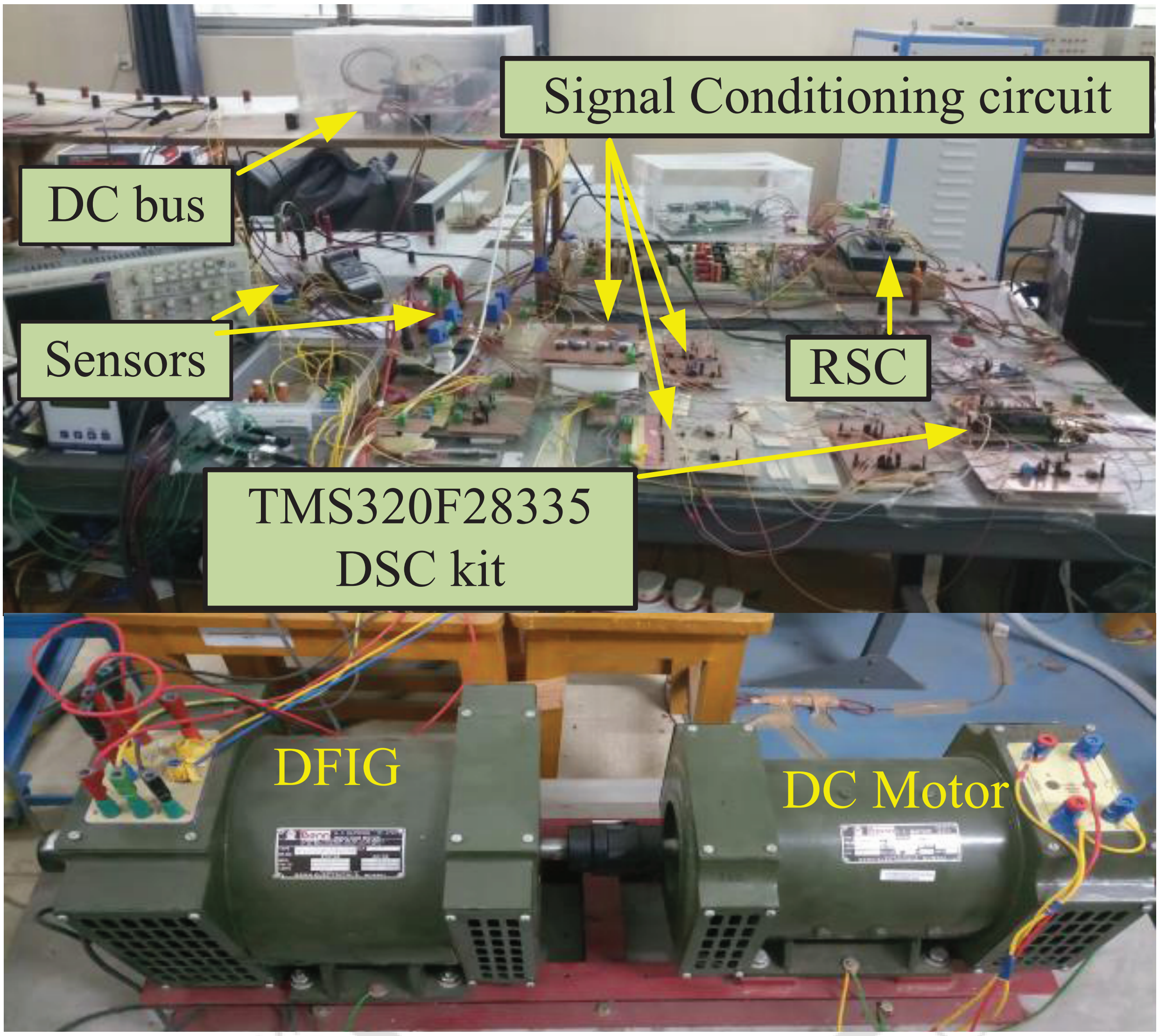

Figure 5.6: Laboratory test rig.

5.6.1 Steady-state performance evaluation of the proposed FOSMO observer

The steady-state performance of the observer in the subsynchronous mode of operation is evaluated for the speeds 209.5 rad/s (1000 rpm), and 293.5 rad/s (1400 rpm). From Figures 5.7(a) and 5.8(a), it is observed that the measured speed and the estimated speed are very close to each other and the error between the estimated speed and the measured speed is less than ±2%. The estimation error for the rotor position is shown in Figures 5.7(b) and 5.8(b). The estimated position closely matches the measured position, and the error is less than 0.1 rad (5.73°). A similar type of performance characteristics is observed for the supersynchronous (331.2 rad/s) mode of operation. The performance curves for the supersynchronous mode are shown in Figure 5.9.

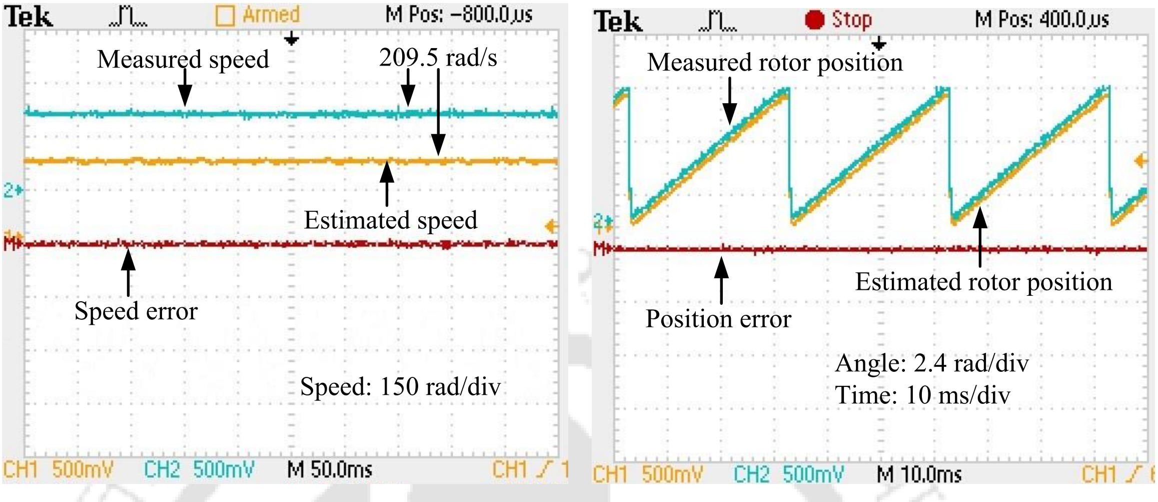

(a) (b)

Figure 5.7: Experimental result regarding the performance of the proposed FOSMO observer at speed 209.5 rad/s (1000 rpm); (a) Measured and estimated rotor speed. (b) Measured and estimated rotor angle.

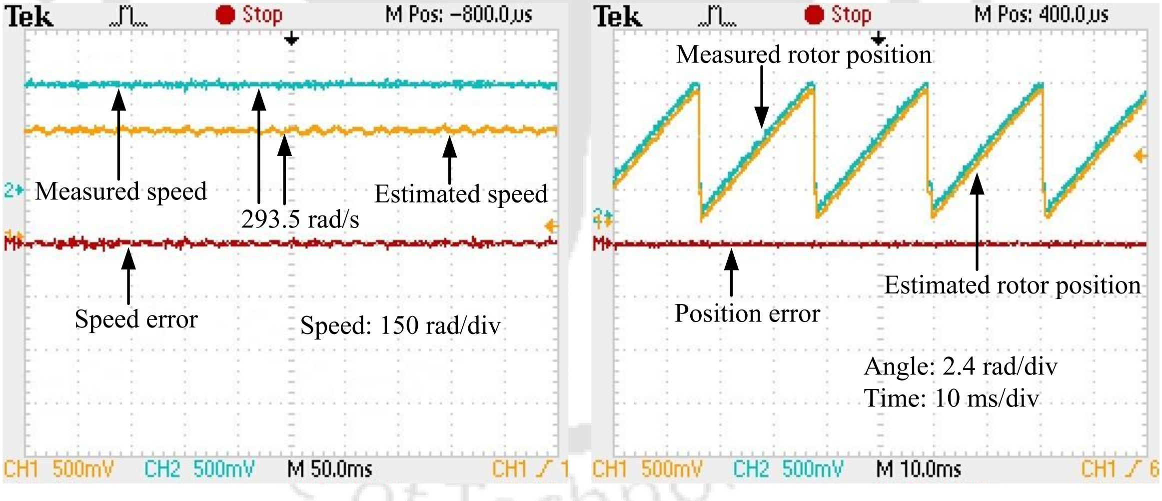

(a) (b)

Figure 5.8: Experimental result regarding the performance of the proposed FOSMO observer at speed 293.5 rad/s (1400 rpm); (a) Measured and estimated rotor speed. (b) Measured and estimated rotor angle.

5.6.2 Dynamic performance evaluation of the proposed FOSMO observer

The dynamic performance of the observer is tested around the synchronous speed, where the rotor speed is changed from supersynchronous (327 rad/s or 1560 rpm) to subsynchronous (306 rad/s or 1460 rpm) speed by applying a sudden change in armature voltage of the DC motor coupled with the DFIG. From Figure 5.10, it is observed that the estimated speed closely follows the measured speed

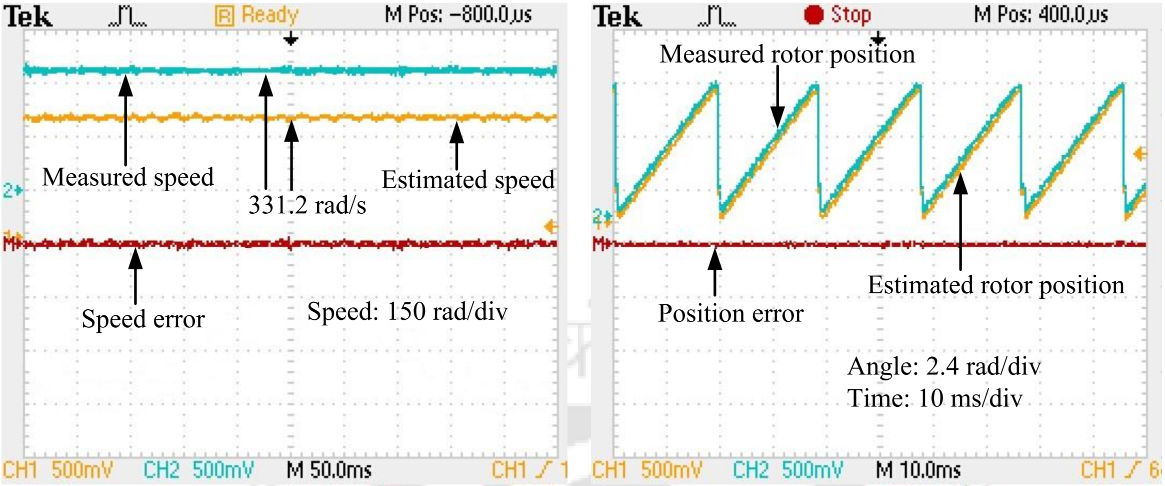

(a) (b)

Figure 5.9: Experimental result regarding the performance of the proposed FOSMO observer at speed 331.2 rad/s (1580 rpm); (a) Measured and estimated rotor speed. (b) Measured and estimated rotor angle.

during the transition from supersynchronous to subsynchronous operation and the maximum speed error is within 5 rad/s during the transition. Here, to capture the dynamics, the time scale is set as 500 ms/div. Rotor current and estimated slip position $\left(\hat{\theta}_{sl} = \theta_s^* - \hat{\theta}_r\right)$ is plotted to show the phase changing of the rotor current, and slip angle during the transition.

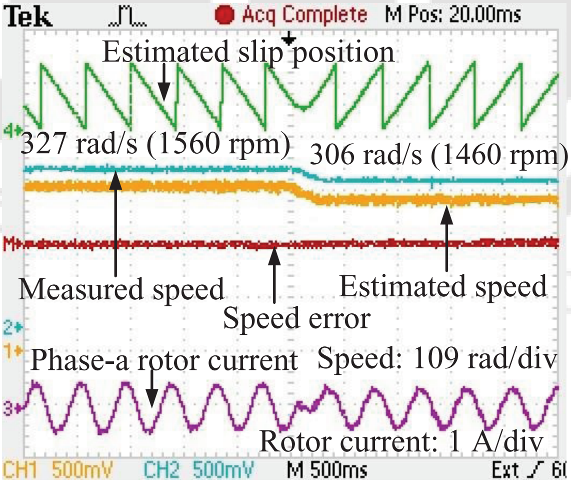

Figure 5.10: Experimental result regarding the performance of the proposed FOSMO observer during speed transition.

5.6.3 Voltage controller performance with the proposed FOSMO observer

The objective of the control strategy is to maintain a specified voltage magnitude and constant frequency under different dynamic conditions. The performance of the voltage controller is tested for two different dynamic conditions while the voltage magnitude is set as 125 V. The first test is done with fixed speed and load change. The second test is done with a fixed load and change in speed. At 291.4 rad/s (1390 rpm) the stator terminal load resistance of DFIG is changed from 313 Ω to 156 Ω. From Figure 5.11(a), it is observed that the estimated speed closely matches the measured speed and the voltage magnitude is appropriately regulated at 125 V during the change in the load connected to the DFIG. Since the load is changed from 313 Ω to 156 Ω, the stator current is also increased, as shown in Figure 5.11(b). To mitigate the increased demand, the rotor current is also increased, as shown in Figure 5.11(a).

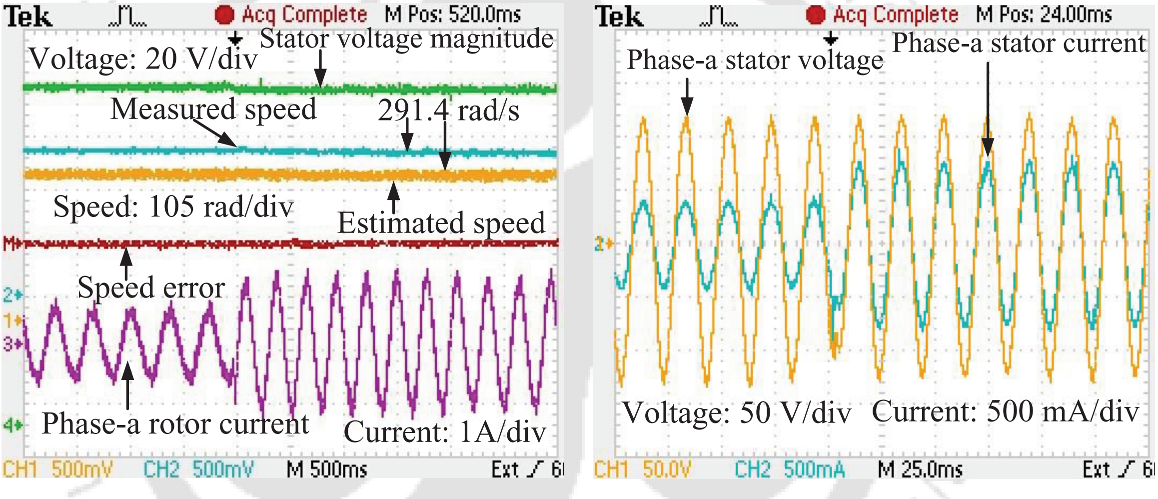

(a) (b)

Figure 5.11: Experimental result regarding the performance of the proposed sensorless control scheme during load change; (a) Voltage magnitude, measured speed, estimated speed and phase-a rotor current. (b) Phase-a voltage and current of the DFIG stator terminal.

For the second test, a sudden change in armature voltage of the DC motor is employed, and the speed is changed from 295.6 rad/s (1410 rpm) to 268.3 rad/s (1280 rpm). It is evident from Figure 5.12 that the voltage controller can regulate the voltage magnitude and the estimated speed closely follows the measured speed during the speed transition. Since the DFIG speed is changed from 295.6 rad/s to 268.3 rad/s the frequency of the rotor current (Figure 5.12(a)) is also changed from 2.95 Hz to 7.29 Hz approximately. Since the test is done at a fixed load, the stator current (Figure 5.12(b)) remains constant during the speed transition.

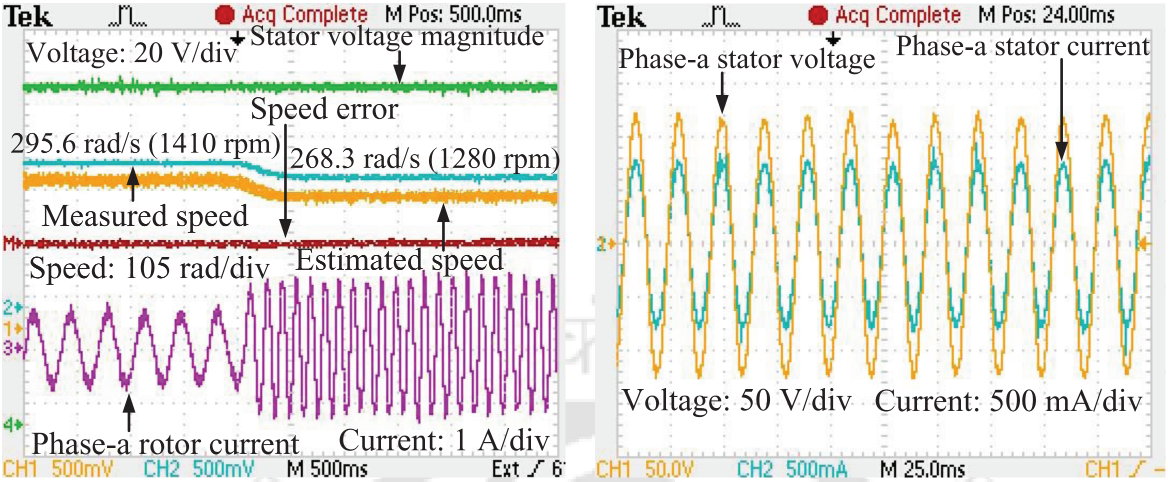

(a) (b)

Figure 5.12: Experimental result regarding the performance of the proposed sensorless control scheme during speed change; (a) Voltage magnitude, measured speed, estimated speed and phase-a rotor current. (b) Phase-a voltage and current of the DFIG stator terminal.

5.7 Summary

A new approach in the form of a sliding mode observer (SMO) is used here to estimate the rotor speed, and position/angle for the sensorless voltage and frequency control of the standalone DFIG system. The stator current and rotor flux are utilized here as the state variables to design the observer. Lyapunov stability criteria are utilized to formulate the sliding gains, which makes the estimation algorithm stable. Sign function is replaced by tan sigmoid function to minimize the chattering effect. The designed observer exhibits excellent performance under different steady-state and dynamic conditions while complying different performance criteria like fast convergence, high accuracy. The proposed estimation technique is found robust against machine parameter variations, and it does not require any mechanical parameters of the DFIG system for its design. The performance of the voltage controller and the estimation algorithm are found robust towards the load variations at the generator terminals. The estimation algorithm is scalable and can be implemented for larger DFIG system.

6

Development of a second-order sliding mode observer (SOSMO) for the rotor speed and position estimation of DFIG

Contents

6.1 Introduction

Inherently sliding model-based techniques are robust to parametric uncertainties and insensitive to bounded external disturbances. However, output chattering is the main problem for first-order SMO (FOSMO). Implementation of low pass filter (LPF) at the FOSMO output can reduce the chattering effect. In addition to that, saturation function can be used to diminish the chattering problem. In contrast to that, second-order sliding mode observer (SOSMO) gives a continuous type of output, hence filtering is not required. Owing to these attributes, a SOSMO observer is proposed here to estimate the rotor speed and position. The proposed technique is tested rigorously in different steady-state and dynamic conditions. The stability and convergence analysis is provided for the designed observer and given in the subsequent subsection.

6.2 Observer design

The SOSMO observer for the speed estimation of the DFIG system utilizes the same dynamic model (5.1) used in the previous Chapter (Chapter-5). Based on the dynamic model (5.1), an observer model is shown below (5.1):

$$\left.\begin{aligned}
\frac{d\hat{i}_{\alpha s}}{dt} &= ai_{\alpha s} + c\hat{\psi}_{\alpha r} + d\hat{\omega}_r\hat{\psi}_{\beta r} + bv_{\alpha s} - hv_{\alpha r} &\quad& \text{(a)}\\
\frac{d\hat{i}_{\beta s}}{dt} &= ai_{\beta s} - d\hat{\omega}_r\hat{\psi}_{\alpha r} + c\hat{\psi}_{\beta r} + bv_{\beta s} - hv_{\beta r} && \text{(b)}\\
\frac{d\hat{\psi}_{\alpha r}}{dt} &= gi_{\alpha s} - f\hat{\psi}_{\alpha r} - \hat{\omega}_r\hat{\psi}_{\beta r} + v_{\alpha r} && \text{(c)}\\
\frac{d\hat{\psi}_{\beta r}}{dt} &= gi_{\beta s} + \hat{\omega}_r\hat{\psi}_{\alpha r} - f\hat{\psi}_{\beta r} + v_{\beta r} && \text{(d)}
\end{aligned}\right\} \qquad (6.1)$$

where $\hat{i}_{\alpha s}$ and $\hat{i}_{\beta s}$ are the estimated rotor currents, $\hat{\psi}_{\alpha s}$ and $\hat{\psi}_{\beta s}$ are the estimated rotor fluxes, $\hat{\omega}_r$ is the input to the observer model.

The error dynamics (6.2) is obtained by subtracting (6.1) from (5.1) and can be represented as given below.

$$\left.\begin{aligned} \frac{d\tilde{i}_{\alpha s}}{dt} &= c\tilde{\psi}_{\alpha r} + d\omega_r\tilde{\psi}_{\beta r} + d\tilde{\omega}_r\hat{\psi}_{\beta r} && \text{(a)} \\ \frac{d\tilde{i}_{\beta s}}{dt} &= -d\omega_r\tilde{\psi}_{\alpha r} - d\tilde{\omega}_r\hat{\psi}_{\alpha r} + \beta\tilde{\psi}_{\beta r} && \text{(b)} \\ \frac{d\tilde{\psi}_{\alpha r}}{dt} &= -f\tilde{\psi}_{\alpha r} - \omega_r\tilde{\psi}_{\beta r} - \tilde{\omega}_r\hat{\psi}_{\beta r} && \text{(c)} \\ \frac{d\tilde{\psi}_{\beta r}}{dt} &= \omega_r\tilde{\psi}_{\alpha r} + \tilde{\omega}_r\hat{\psi}_{\alpha r} - f\tilde{\psi}_{\beta r} && \text{(d)} \end{aligned}\right\} \tag{6.2}$$

where $\tilde{i}_{\alpha s} = \hat{i}_{\alpha s} - i_{\alpha s}$ and $\tilde{i}_{\beta s} = \hat{i}_{\beta s} - i_{\beta s}$ are defined as current estimation errors and $\tilde{\psi}_{\alpha r} = \hat{\psi}_{\alpha r} - \psi_{\alpha r}$ and $\tilde{\psi}_{\beta r} = \hat{\psi}_{\beta r} - \psi_{\beta r}$ are the flux estimation errors.

The switching surface is defined as

$$s = \tilde{i}_{\beta s}\hat{\psi}_{\alpha r} - \tilde{i}_{\alpha s}\hat{\psi}_{\beta r}. \tag{6.3}$$

6.2.1 Observer structure

Choosing the observer inputs $\hat{\omega}_r$ as

$$\begin{aligned} \hat{\omega}_r &= k_1 \sqrt{|s|}\,\mathrm{sign}\,(s) + \omega_1 \\ \dot{\omega}_1 &= k_2\,\mathrm{sign}\,(s) \end{aligned} \tag{6.4}$$

where $k_1, k_2 > 0$ are the chosen gain parameters, the expression for $\dot{s}$ is expressed as

$$\dot{s} = \hat{\psi}_{\alpha r}\frac{d\tilde{i}_{\beta s}}{dt} + \tilde{i}_{\beta s}\frac{d\hat{\psi}_{\alpha r}}{dt} - \hat{\psi}_{\beta r}\frac{d\tilde{i}_{\alpha s}}{dt} - \tilde{i}_{\alpha s}\frac{d\hat{\psi}_{\beta r}}{dt}. \tag{6.5}$$

Expanding (6.5), $\dot{s}$ is further represented as

$$\begin{aligned} \dot{s} = c\left(\hat{\psi}_{\alpha r}\tilde{\psi}_{\beta r} - \tilde{\psi}_{\alpha r}\hat{\psi}_{\beta r}\right) - d\omega_r\left(\hat{\psi}_{\alpha r}\tilde{\psi}_{\alpha r} + \tilde{\psi}_{\beta r}\hat{\psi}_{\beta r}\right) - d\tilde{\omega}_r\left(\hat{\psi}_{\alpha r}^2 + \hat{\psi}_{\beta r}^2\right) - \hat{\omega}_r\left(\tilde{i}_{\alpha s}\hat{\psi}_{\alpha r} + \tilde{i}_{\beta s}\hat{\psi}_{\beta r}\right) \\ -fs + g\left(i_{\alpha r}\tilde{i}_{\beta r} - i_{\beta r}\tilde{i}_{\alpha r}\right) + v_{\alpha r}\tilde{i}_{\beta s} - v_{\beta r}\tilde{i}_{\alpha s} \end{aligned} \tag{6.6}$$

The expression (6.6) can be further expressed as

$$\dot{s} = f_1\left(\tilde{i}_{\alpha\beta s}, i_{\alpha\beta s}, \tilde{\psi}_{\alpha\beta s}, \hat{\psi}_{\alpha\beta s}, \omega_r\right) - f_2\left(\tilde{i}_{\alpha\beta s}, \tilde{\psi}_{\alpha\beta r}, \hat{\psi}_{\alpha\beta r}\right)\hat{\omega}_r \tag{6.7}$$

where

$$f_1\left(\tilde{i}_{\alpha\beta s}, i_{\alpha\beta s}, \tilde{\psi}_{\alpha\beta s}, \hat{\psi}_{\alpha\beta s}, \omega_r\right) = c\left(\hat{\psi}_{\alpha r}\tilde{\psi}_{\beta r} - \tilde{\psi}_{\alpha r}\hat{\psi}_{\beta r}\right) - d\omega_r\left(\hat{\psi}_{\alpha r}\tilde{\psi}_{\alpha r} + \tilde{\psi}_{\beta r}\hat{\psi}_{\beta r}\right) + d\omega_r\left(\hat{\psi}^2_{\alpha r} + \hat{\psi}^2_{\beta r}\right) \\ -fs + v_{\alpha r}\tilde{i}_{\beta s} + g\left(i_{\alpha s}\tilde{i}_{\beta s} - i_{\beta s}\tilde{i}_{\alpha s}\right) - v_{\beta r}\tilde{i}_{\alpha s} \tag{6.8}$$

and

$$f_2\left(\tilde{i}_{\alpha\beta s}, \tilde{\psi}_{\alpha\beta r}, \hat{\psi}_{\alpha\beta r}\right) = d\hat{\psi}^2_{\alpha r} + d\hat{\psi}^2_{\beta r} + \tilde{i}_{\alpha s}\hat{\psi}_{\alpha r} + \tilde{i}_{\beta s}\hat{\psi}_{\beta r} \tag{6.9}$$

Based on the assumption of boundedness on the system states and system input, it can be said that $f_1\left(\tilde{i}_{\alpha\beta s}, i_{\alpha\beta s}, \tilde{\psi}_{\alpha\beta s}, \hat{\psi}_{\alpha\beta s}, \omega_r\right)$ and $f_2\left(\tilde{i}_{\alpha\beta s}, \tilde{\psi}_{\alpha\beta r}, \hat{\psi}_{\alpha\beta r}\right)$ are bounded. Thus it is reasonable to say that $\left|\dot{f}_1\left(\tilde{i}_{\alpha\beta s}, i_{\alpha\beta s}, \tilde{\psi}_{\alpha\beta s}, \hat{\psi}_{\alpha\beta s}, \omega_r\right)\right| + \left|\dot{f}_2\left(\tilde{i}_{\alpha\beta s}, i_{\alpha\beta s}, \tilde{\psi}_{\alpha\beta s}, \hat{\psi}_{\alpha\beta s}, \omega_r\right)\right| \leq A$ and $0 < B_m \leq f_2\left(\tilde{i}_{\alpha\beta s}, \tilde{\psi}_{\alpha\beta r}, \hat{\psi}_{\alpha\beta r}\right) \leq B_M$, where $A,\ B_m,\ B_M$ are positive constants. Thus according to [92], the above gains ($k_1,\ k_2$) should obey the following conditions (6.10) to make $s = 0$ and $\dot{s} = 0$ in finite time.

$$\begin{aligned} k_1^2 &\geq \frac{4A}{B_m^2}\frac{B_M(k_2 + A)}{B_m(k_2 - A)} \\ k_2 &> \frac{A}{B_m} \end{aligned} \tag{6.10}$$

Now choosing k_1 and k_2 sufficiently large, the objective of speed observer is met. A detailed analysis is available in [92].

The choice of the gains is directly influenced by the above expression (6.10). Hence, before choosing the gains, it is compulsory to choose different bounds ($A,\ B_m,\ B_M$). These bounds have been achieved by a comprehensive simulation study of the system. The system has been studied for different modulation indexes, with different load conditions at the stator terminal and with different speeds. Finally, the bounds have been found as: $A = 1000$, $B_m = 1.4$ and $B_M = 5$ and the corresponding values for the gains are selected as $k_1 = 132$ and $k_2 = 2500$.

6.2.2 Convergence and stability

Once sliding mode occurs $\tilde{i}_{\alpha s}, \tilde{i}_{\beta s} = 0$, which implies that $s = 0$ and $\dot{s} = 0$. Putting $\tilde{i}_{\alpha s}, \tilde{i}_{\beta s} = 0$ and $s = \dot{s} = 0$ in (6.6) the expression for the equivalent control $\hat{\omega}_r^{eq}$ is written as

$$\hat{\omega}_r^{eq} = \omega_r + \frac{c}{d}\frac{\hat{\psi}_{\alpha r}\tilde{\psi}_{\beta r} - \tilde{\psi}_{\alpha r}\hat{\psi}_{\beta r}}{\hat{\psi}^2_{\alpha r} + \hat{\psi}^2_{\beta r}} - \omega_r\frac{\tilde{\psi}_{\alpha r}\hat{\psi}_{\alpha r} + \hat{\psi}_{\beta r}\tilde{\psi}_{\beta r}}{\hat{\psi}^2_{\alpha r} + \hat{\psi}^2_{\beta r}} \tag{6.11}$$

For the SOSMO observer in (6.4), ω_1 substitutes $\hat{\omega}_r^{eq}$ as equivalent control. $\hat{\omega}_r$ is the input to the observer model which is the output of an integrator and it is automatically continuous. From (6.11) it is evident that if $\tilde{\psi}_{\alpha\beta r} = 0$ then, $\hat{\omega}_r^{eq} = \omega_r$.

Once the sliding is achieved, the current estimation error is $\tilde{i}_{\alpha\beta s} = 0$, hence the time derivative of the current estimation error is also $\dot{\tilde{i}}_{\alpha\beta s} = 0$, which implies that the each terms of the right hand side of current error dynamics given by (6.2(a)) and (6.2(b)) are individually zero. Since under the stable operation of a DFIG, $c, d, \omega_r \neq 0$, then $\tilde{\psi}_{\alpha r}, \tilde{\psi}_{\beta r}, \tilde{\omega}_r = 0$, which implies that $\hat{\omega}_r^{eq} = \omega_r$. The schematic diagram of the observer structure is represented in Figure 6.1. The rotor voltage input to the observer $v_{\alpha r}^{sl}$ and $v_{\beta r}^{sl}$ is generated using the relationship $v_{\alpha\beta r}^{sl} = n m_{\alpha\beta r}^{sl} \frac{V_{dc}}{2}$, where $m_{\alpha\beta r}^{sl}$ is the modulation index in $\alpha\beta$ domain, V_{dc} is the dc bus voltage and n is the turns ratio. The superscript sl denotes that the quantities are in slip frequency.

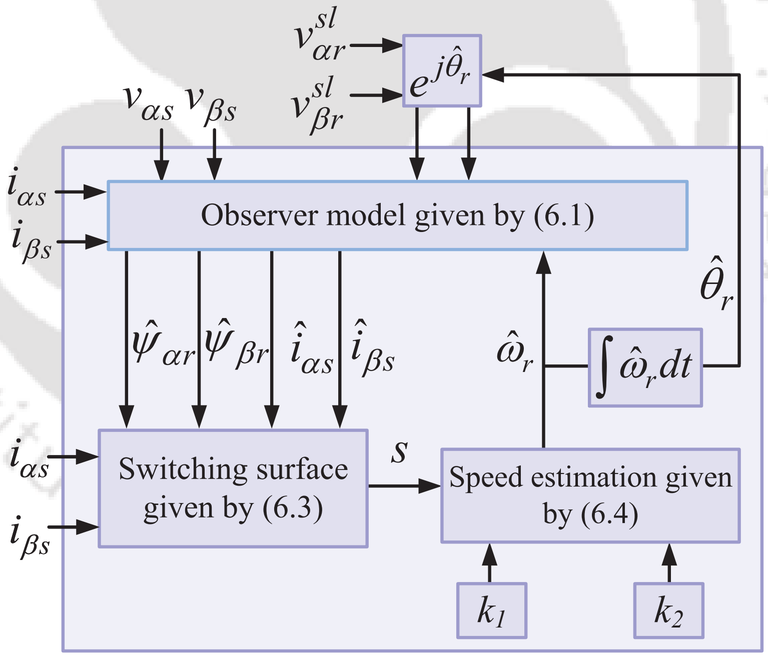

Figure 6.1: Schematic diagram of the proposed SOSMO observer

6.3 Simulation results and discussion

A rigorous simulation is done in Matlab/Simulink to understand the working of the sensorless operation of the DFIG in standalone mode. The performance of the designed observer is evaluated for the speed of 250 rad/s to 350 rad/s and found working seamlessly for different dynamic conditions imposed on it. The simulation results are provided below (Figures 6.2-6.3).

6.3.1 Performance of the proposed SOSMO observer under the step change in reference speed

The dynamic performance of the observer is evaluated for a step change of 25 rad/s in the reference speed at the interval of 1 s, and the performance curve is shown in Figure 6.2. The observer estimates the speed (±0.5% of the measured speed) approximately within 200 ms, i.e., the speed error $\tilde{\omega}_r$ goes to zero within 200 ms.

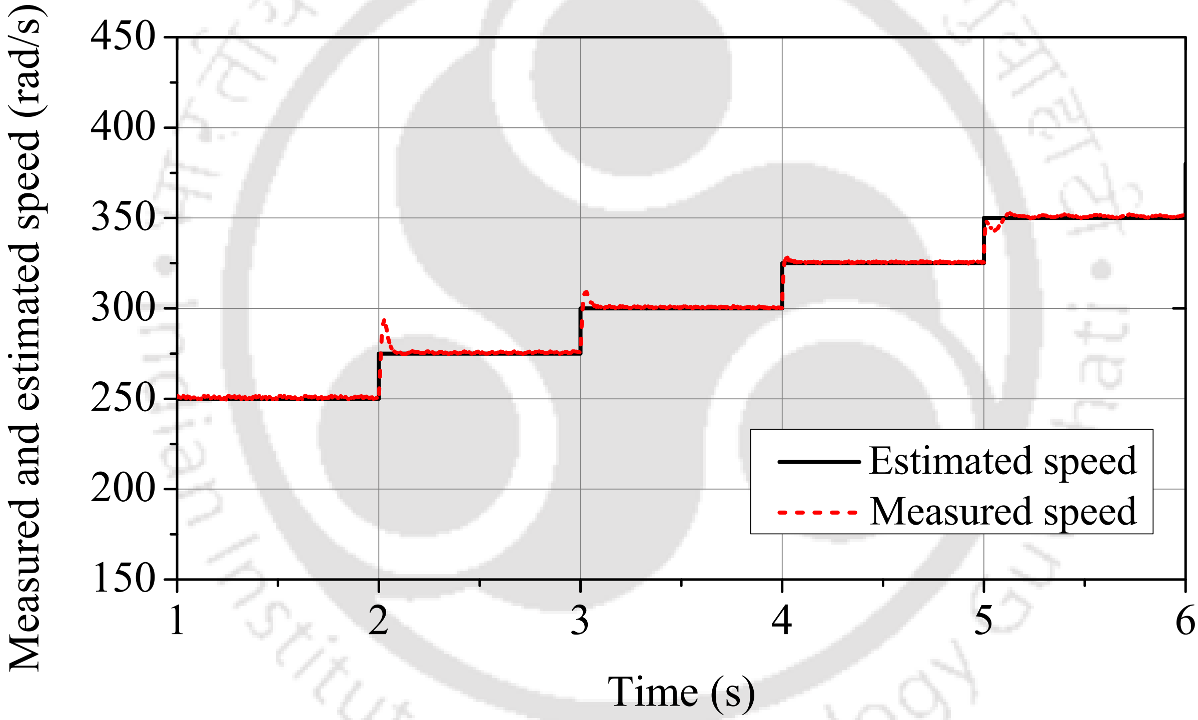

Figure 6.2: Simulation result regarding the performance of the proposed SOSMO observer under the step change in reference speed.

6.3.2 Performance of the proposed SOSMO observer under the ramp change in reference speed

Observer performance is evaluated for a ramp type of reference speed input, and the performance curve is shown in Figure 6.3. The designed observer exhibits excellent performance under the ramp change of the speed, and the estimated speed follows the measured speed quiet accurately during ramp change in speed. From 2 s to 4 s the reference speed ramps up from 250 rad/s to 350 rad/s with a positive slope, and from 6 s to 8 s the reference speed ramps down from 350 rad/s to 250 rad/s. The speed error is less than ±1% during the ramp change in speed.

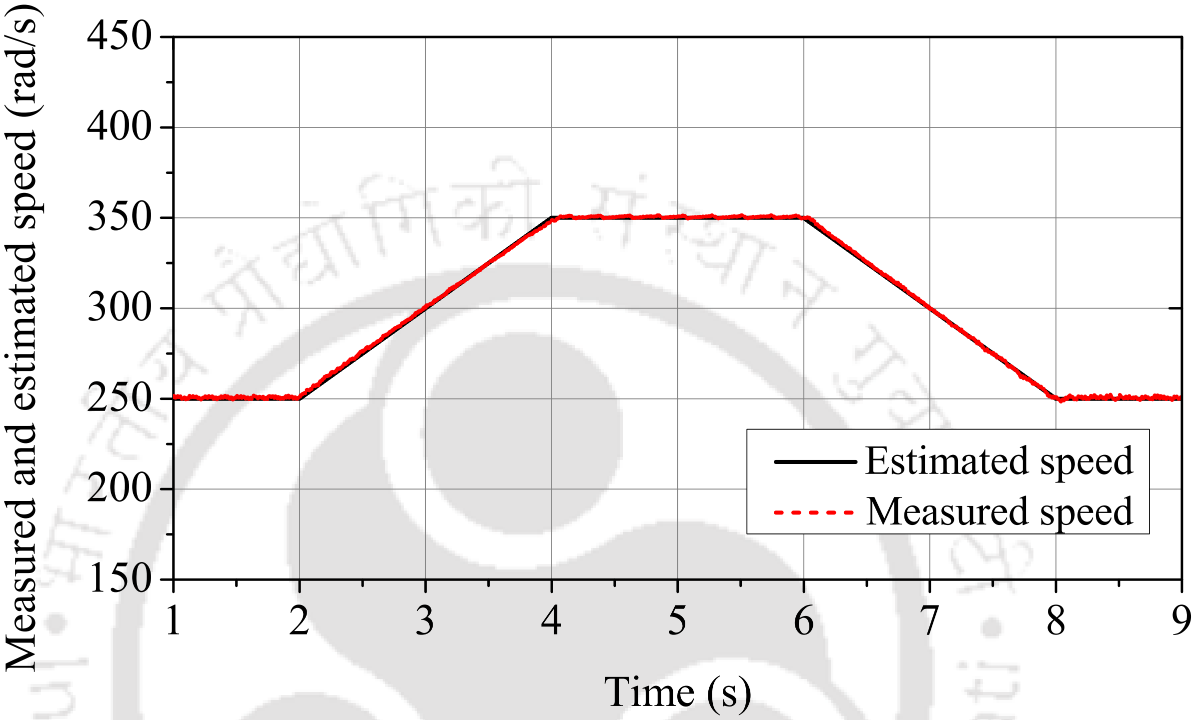

Figure 6.3: Simulation result regarding the performance of the proposed SOSMO observer during ramp change in reference speed.

6.4 Experimental results and discussion

Different tests are done to evaluate the performance of the observer. The observer is evaluated both for the steady-state and dynamic conditions in a hardware test setup in the laboratory. The experimental schematic diagram of the hardware test setup is provided in Figure 6.4, and the picture of the DFIG based laboratory test set up is shown in Figure.5.6. The DFIG runs at standalone mode, and the stator is connected with a fixed three-phase resistive load of 180Ω. The TMS320F28335-based digital signal controller (DSC) has been used for the hardware implementation of the observer. The clock speed of the DSC kit is 150 MHz. The estimation algorithm runs at 5 kHz, while the PWM frequency of the rotor side converter (RSC) is chosen as 2 kHz.

During the test, a fixed modulation index m_{dr}^* and m_{qr}^* has been used to drive the RSC, and *dq* to *abc* transformation is employed to get m_{ar}, m_{br} and m_{cr} using the calculated slip angle $\hat{\theta}_{sl} = \theta_s - \hat{\theta}_r$. The observer is evaluated in steady-state at speeds 272 rad/s (1300 rpm), and 335.5 rad/s (1600 rpm),

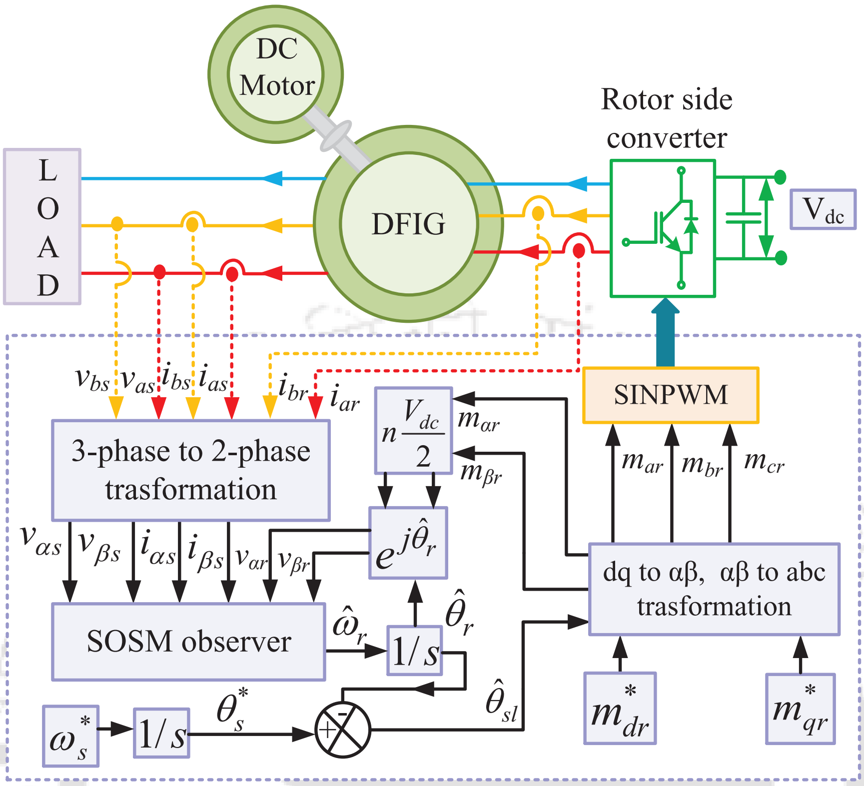

Figure 6.4: Schematic diagram of the experimental system.

approximately. The transient response of the observer is evaluated around the synchronous speed by employing a sudden change in DC motor armature voltage.

6.4.1 Response of the proposed SOSMO observer in steady-state

The steady-state performance of the observer is evaluated for two cases. In the first case, the observer is tested below the synchronous speed (272 rad/s or 1300 rpm approximately), and the performance curves regarding this test are shown in Figure 6.5. For the second case, the observer is tested above the synchronous speed at 335.5 rad/s (1600 rpm) approximately and the plots regarding the second test are shown in Figure 6.6. From Figures 6.5 and 6.6, it is evident that the speed estimator is working fine for both the cases. The estimation error for the speed and position is found acceptable, and the errors are within the working boundary.

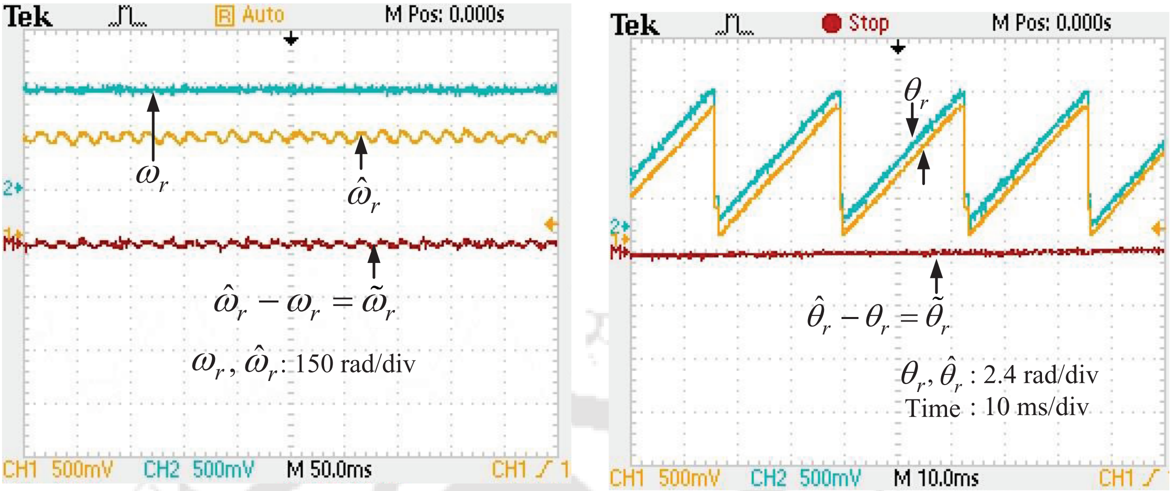

(a) (b)

Figure 6.5: Experimental result regarding the performance of the proposed SOSMO observer at speed 272 rad/s (1300 rpm); (a) Measured and estimated rotor speed. (b) Measured and estimated rotor angle.

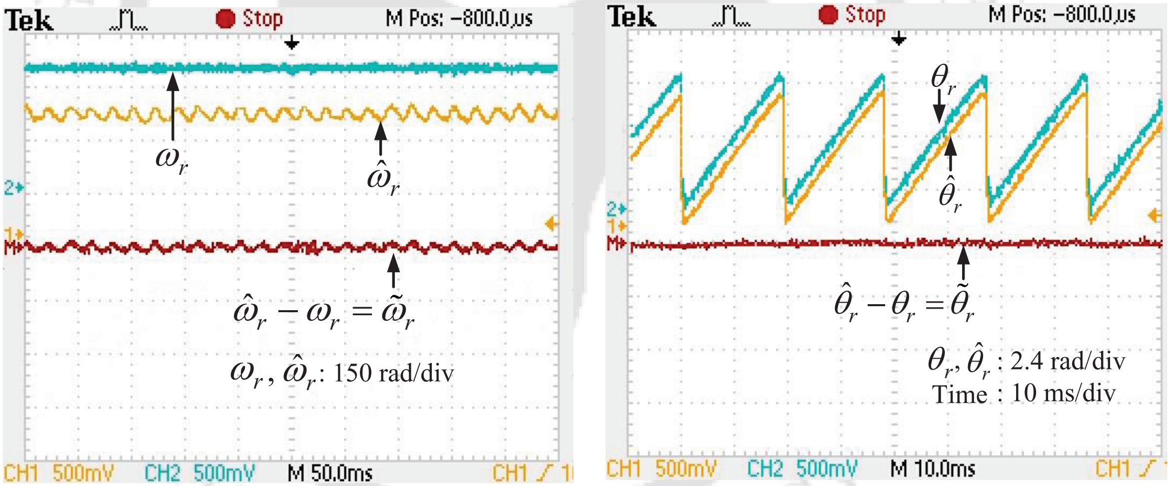

(a) (b)

Figure 6.6: Experimental result regarding the performance of the proposed SOSMO observer at speed 335.5 rad/s (1600 rpm); (a) Measured and estimated rotor speed. (b) Measured and estimated rotor angle.

6.4.2 Response of the proposed SOSMO observer during speed change

The observer is tested for the speed change near the synchronous speed, i.e., 314.159 rad/s or 1500 rpm. The test is conducted by giving a step change in armature voltage of the DC motor. The DC motor runs at 302 rad/s (1440 rpm) approximately, and after the step change in armature voltage of the DC motor, the motor runs at 330 rad/s (1575 rpm) approximately. The performance curves of the observer for the speed change are shown in Figure 6.7. It is observed from Figure 6.7, that the observer is exhibiting good dynamic performance during the speed change, and the speed error is found to be within the working boundary. Figure 6.7 show the phase reversal of the rotor current during the speed change from subsynchronous to supersynchronous. The plot also includes the corresponding change in slip angle.

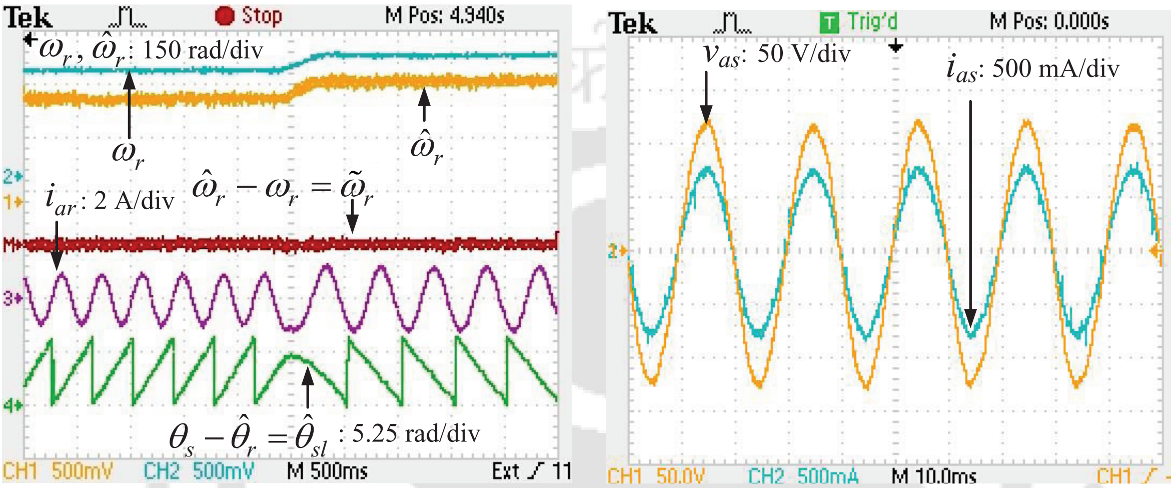

(a) (b)

Figure 6.7: Dynamic performance of the observer during the speed change from 302 rad/s (1440 rpm) to 330 rad/s (1575 rpm). (a) Plots of measured and estimated rotor speed, slip angle and rotor current. (b) Plots of phase-a voltage (v_{as}) and current (i_{as}).

6.5 Summary

A second-order sliding mode observer (SOSMO) is designed to estimate the rotor speed and position of a standalone DFIG-based wind energy conversion system. The rotor flux and the stator current are used as the state variables to design the observer. Since SOSMO observer gives a continuous type of output, filtering is not required and chattering free output is achieved. The estimation algorithm is thoroughly tested on a hardware test setup in the laboratory. The ability of the designed observer is tested under steady-state and dynamic conditions. The response of the observer is found to be satisfactory for a change in the reference speed.

7

Conclusion and future works

Contents

7.1 General remark

The main aim of this thesis work is to develop controllers and observers for the generation control of a standalone DFIG-based WECS. The control consists of two main subsystems which are grid side converter (GSC) control system, and rotor side converter (RSC) control system. Hence, efficient control of these two subsystems is the most crucial requirement for the smooth operation of a DFIG system. However, for synchronizing the GSC to the grid, the information of the phase and frequency of the grid voltage is required. The PLL system estimates the phase and frequency of the grid voltage, which is required to synchronize the GSC. Hence, a simple and robust PLL technique is developed to estimate the phase and the frequency of the grid voltage.

A typical control system must be stable under disturbances and must fulfil different performance criteria like high accuracy, fast convergence, low overshoot subject to different dynamic conditions. In addition to that, the control system must be robust against any parametric uncertainty associated with the plant. In light of this, efficient and robust control strategies are developed to control the GSC.

The RSC controller has a similar structure like the GSC controller; however, to implement RSC control accurate information of the rotor speed and angle/position is required. A rotary encoder can be used to measure the rotor speed and position. However, these encoders are expensive, and they have reliability issues; moreover, hardware complexity is inevitable for these encoders. Hence, encoderless control of RSC is highly desirable for the DFIG-based WECS. Therefore, robust observers are developed to estimate the rotor speed and angle for sensorless voltage frequency control of the standalone DFIG system. The GSC, RSC controllers and the associated subsystems like PLL, rotor speed and position estimators are implemented on a TMS320F28335 DSC kit and tested on a hardware test setup of a standalone DFIG system. In the subsequent section, the important findings of this thesis work are discussed.

7.2 Important findings

Chapter 2 proposes a simple yet robust technique to improve the synchronous reference frame (SRF)-based PLL system for estimating the phase and frequency of the grid voltage. The main conclusions from this chapter are drawn as follows:

- An effective and efficient technique is proposed, which can estimate the phase angle and frequency of the grid quiet accurately under different grid abnormalities like frequency jump, phase jump, harmonic distortion and unbalance in grid voltage.
- The technique employes two notch filters and one low pass filter (LPF) in the phase detector (PD) block of the SRF-PLL system and PID type loop filter is used instead of PI type.
- The in-loop two notch filters and the LPF are designed, and the cut-off frequencies are decided based on the small-signal analysis.
- During the implementation of the proposed PLL technique it is observed that it requires less number of arithmetic and trigonometric operations as compared to other enhanced filter based PLL techniques like multiple reference frame (MRF)-PLL, Multiple second-order generalized integrator (MSOGI) based PLL, delayed signal cancellation based (DSC) PLL etc. [10].
- A comparative analysis of the proposed PLL technique with other two similar SRF-PLL techniques (LPF-based SRF-PLL and MRF-PLL) has been done on a TMS320F28335 DSP kit, and similar comparable performance with respect to the other techniques is observed.

Chapter 3 proposes an adaptive control strategy to control the GSC. The GSC controller consists of two cascaded control loops. The inner loop is used to control the grid currents, and the outer loop is used to control the DC bus voltage. An adaptive-MIMO current control strategy is developed here to control the active and reactive component of the grid currents. Whereas to control the DC bus voltage, extended state observer (ESO) based adaptive voltage control strategy is developed. To formulate the current control law, the *dq*-axis dynamic model of the GSC is used. To transform the three-phase grid variables (*abc*) like grid voltage and grid current into stationary DC variables (*dq*), the proposed PLL technique is used. The main findings of this chapter are as follows:

- The proposed adaptive-MIMO current controller is robust towards any parametric uncertainty associated with the grid filter. In addition to that, the proposed current controller does not require any apriori information about the grid filter parameters. This makes the proposed current control strategy immune to any parameter variations.

- Lyapunov stability criteria are used to derive the proposed adaptive current control law. This makes the proposed current controller inherently stable towards disturbances.
- Lyapunov like stability analysis is provided for the proposed current controller.
- The proposed current controller exhibits excellent performance in terms of fast convergence, high accuracy and low overshoot under different dynamic conditions.
- The performance of the proposed current controller is compared with the linear PI current controller under different dynamic conditions in a hardware test setup.
- Parameters section procedure is discussed regarding the control implementation.
- The ESO-based adaptive voltage control strategy includes external load disturbance as an extended state of the system.
- The design of the proposed voltage controller is similar to the proposed current controller; however, there is a slight modification in terms of ESO. ESO is capable of estimating both the common disturbance and the system states. Due to this, the proposed voltage control strategy exhibits excellent performance under the dynamic load change across the DC bus.
- The proposed voltage controller is compared with the linear PI voltage regulator under the dynamic load change in a hardware test setup.
- The proposed voltage controller shows excellent performance in terms of fast convergence, high accuracy and low overshoot under the dynamic load change.

In Chapter 4 a smooth robust controller based on first-order sliding mode control (FOSMC) technique is proposed to control the active and reactive grid currents. To formulate this control law, the *dq* dynamic model of the GSC is used. To transform the three-phase grid variables (*abc*) like grid voltage and grid current into stationary DC variables (*dq*), the proposed PLL technique is used. The main conclusions are shown as follows:

- Fundamentally, first-order sliding mode techniques have an inherent output chattering problem. An effort has been made to design a smooth robust controller in the form of a first-order sliding mode controller (SMC) so that output chattering can be minimized.
- Lyapunov stability criteria are used to derive the smooth robust current control law. This makes the control law inherently stable towards disturbances.
- The stability analysis and the choice of the sliding gains are discussed in detail.
- It is observed from the simulation results regarding the step changes in *d* and *q*-axis reference currents that the smooth robust current controller produces higher peak overshoot than the adaptive-MIMO current controller; however, the smooth robust current controller settles a little faster.
- The hardware experimentation of the smooth robust current controller shows comparable performance under different dynamic conditions.
- The developed smooth robust current controller is robust to parametric variations.

Chapter 5 proposes a speed observer in the form of a first-order sliding mode observer (FOSMO) for the estimation of the rotor speed and position of the DFIG system. To develop the observer model, the $\alpha\beta$ dynamic model of the DFIG is used. Mechanical parameters regarding the DFIG is not required to develop the proposed speed observer. The main conclusions are listed as follows:

- The stator currents and rotor fluxes are used as the state variables to design the observer.
- Lyapunov stability criteria are used to derive the sliding gains for the designed observer; thus, fast convergence and stability is guaranteed.
- To counter the chattering effect, tan sigmoid function is implemented instead of sign function. This ensures chattering-free smooth output.

- The speed observer is rigorously tested in simulation over the whole speed range (±30% around the synchronous speed) of the DFIG system.
- The steady-state and dynamic performance of the speed observer are evaluated on a hardware test bench in the laboratory.
- The efficacy of the proposed speed observer is further validated through stator's voltage frequency control under different dynamic conditions like dynamic speed change of the rotor and dynamic load change at the stator terminal.
- The dynamic response of the observer is found very encouraging to any speed variations.
- The designed observer is found insensitive towards parametric uncertainties and external disturbances.

In Chapter 6, a second-order sliding mode observer (SOSMO) is proposed to estimate the rotor speed and position of the DFIG system. SOSMO gives a continuous type of output, hence filtering is not required. The main conclusions are listed as follows:

- Stability and convergence analysis is provided for the designed observer.
- The rotor flux and the stator current are used as the state variables to design the observer.
- The estimation algorithm is thoroughly tested on a hardware test setup in the laboratory. The ability of the designed observer is tested under steady-state conditions and as well as in dynamic conditions.
- The response of the observer is found very promising to any speed change.

7.3 Thesis contributions

The main contributions of the research work are highlighted below:

- A reliable, simple, yet robust PLL is designed to estimate the grid voltage's frequency and phase angle accurately in the presence of different grid abnormalities.

- An adaptive multi-input multi-output (MIMO) current control algorithm and a smooth, robust current control algorithm in the form of a first-order sliding mode control (FOSMC) are developed to control the active and reactive component of the grid current for the grid side converter (GSC). The proposed current controllers are able to handle the nonlinearities and parameter uncertainties associated with the GSC, and exhibit stable performance against large-signal disturbances, and work seamlessly under different operating points while fulfilling the various performance criteria like fast convergence, high accuracy and low overshoot.

- An extended state observer (ESO)-based adaptive voltage control algorithm is developed to control the DC-link voltage of the GSC. The proposed voltage controller exhibit stable performance against external load disturbances, and work seamlessly under different operating points while fulfilling the various performance criteria like fast convergence, high accuracy and low overshoot.

- Two robust speed adaptive estimation algorithms are developed to estimate the rotor speed of the DFIG. The first observer is based on the first-order sliding mode observer (FOSMO), and the second observer is based on second-order sliding mode observer (SOSMO). Furthermore, the speed estimation schemes are robust to parametric variations of the machine, and can work accurately for different operating points while satisfying the various performance criteria.

- Finally, a speed sensorless voltage control scheme is developed using the observers. The sensorless scheme is able to regulate the desired stator voltage magnitude under the load change at the DFIG stator terminal and the speed change of the rotor.

- All the control and observer algorithms are tested in real-time on a hardware test setup of a standalone DFIG system by utilizing a TMS320F28335 DSP kit.

7.4 Suggestions for future work

The present thesis work can be extended in future, and some further works are suggested below.

- The effect of the grid harmonics on the proposed current controllers for GSC can be analyzed.
- To control the stator voltage of the DFIG more sophisticated and robust controller can be used, and the performance of the controller can be checked under different faulty condition of the system.
- The impact of the harmonics on the proposed observers can be explored in future.
- The sensorless voltage frequency control of the DFIG system can be studied with the nonlinear loads attached to the DFIG stator.

A

Power circuit specifications

A.1 Rating of the DFIG:

General rating: 3 Hp, 3-phase, 4 pole, 50 Hz

Stator rating: 415 V Y-connected 4.7 A

Rotor rating: 200 V Y-connected 7.8 A

Make: BENN Electricals

A.2 Parameters of the DFIG:

The parameters of the DFIG are given in TableA.1

Table A.1

Parameters	Values
R_s	10.26 Ω
R_r	1.46 Ω
L_{ls}	10.11 mH
L_{lr}	10.11 mH
L_m	365.00 mH

A.3 Power Converters:

A.3.1 RSC:

Intelligent power module (IPM: IGBT based)

Specifications: 1200 V 25 A

Make: Mitsubishi

A.3.2 GSC/SSC:

Three-phase four leg IGBT based PWM Inverter

Make: Semikron

A.3.3 DC link capacitor:

$2X4700\mu$F, Electrolytic, 550 V

A.4 Sensors and interfacing circuits:

A.4.1 Current transducer:

LA55P

Specification: Hall effect, Closed loop 50 A, 100 kHz bandwidth

Make: LEM

A.4.2 Voltage transducer:

LV25P

Specification: Hall effect, Closed loop 500 V, 100 kHz bandwidth

Make: LEM

A.4.3 Sensor interfacing circuit:

TL084 Opamp based

Input: ±3.3 V

output:0-3.3 V range

Specification: Wide common-Mode and differential voltage ranges; High Slew Rate; Output Short-Circuit Protection

Make: Texas Instruments

A.5 Microcontroller:

DSP/DSC kit: TMS320F28335 Experimenter kit

Specification: Floating point, 32-bit, 150 MHz

Make: Texas Instruments

A.6 Grid filter:

3 X 15 mH, 5 A, Ferrite core

A.7 DC motor:

Separately excited DC motor

Armature rating: 3 hp, 220 V, 15 A, 1500 RPM

Field rating: 220 V, 1 A

Make: BENN Electricals

A.8 Experimental setup:

The experimental setup consists of two separate setups dedicated for evaluating the performances of the grid side converter (GSC) control strategies and rotor side converter (RSC) control strategies.

A. Power circuit specifications

The pictorial representations of the laboratory test rig regarding GSC and RSC are shown below.

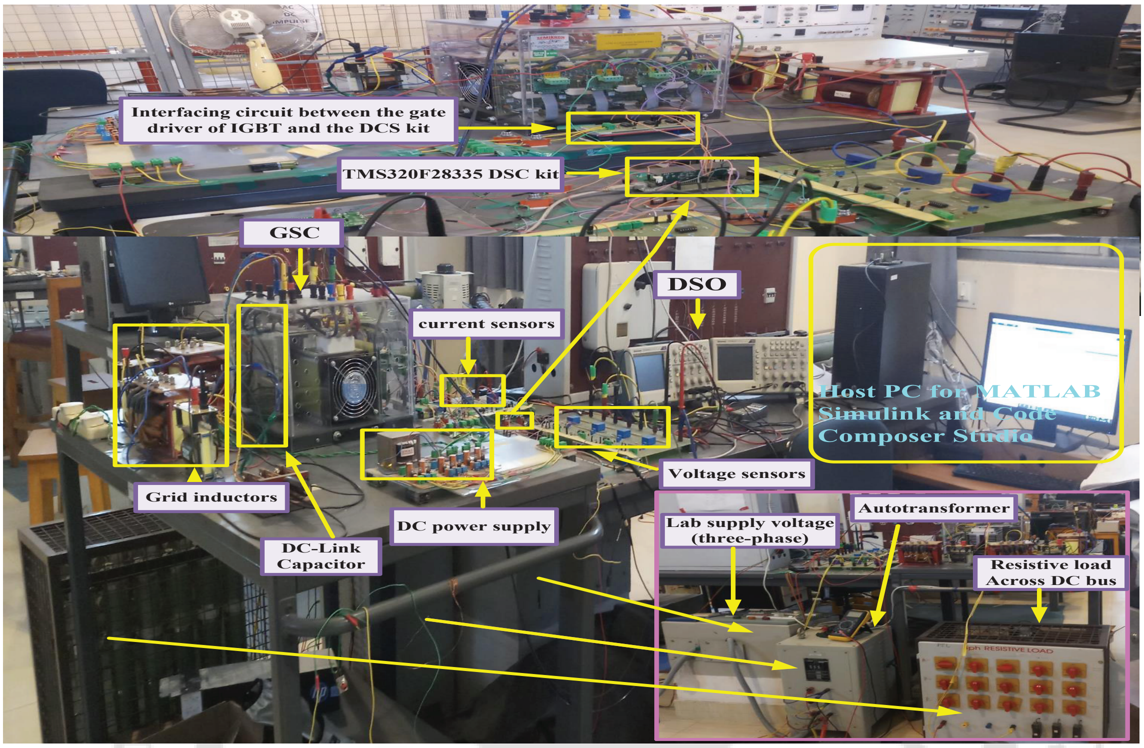

Figure A.1: Pictorial representation of the experimental setup of the GSC

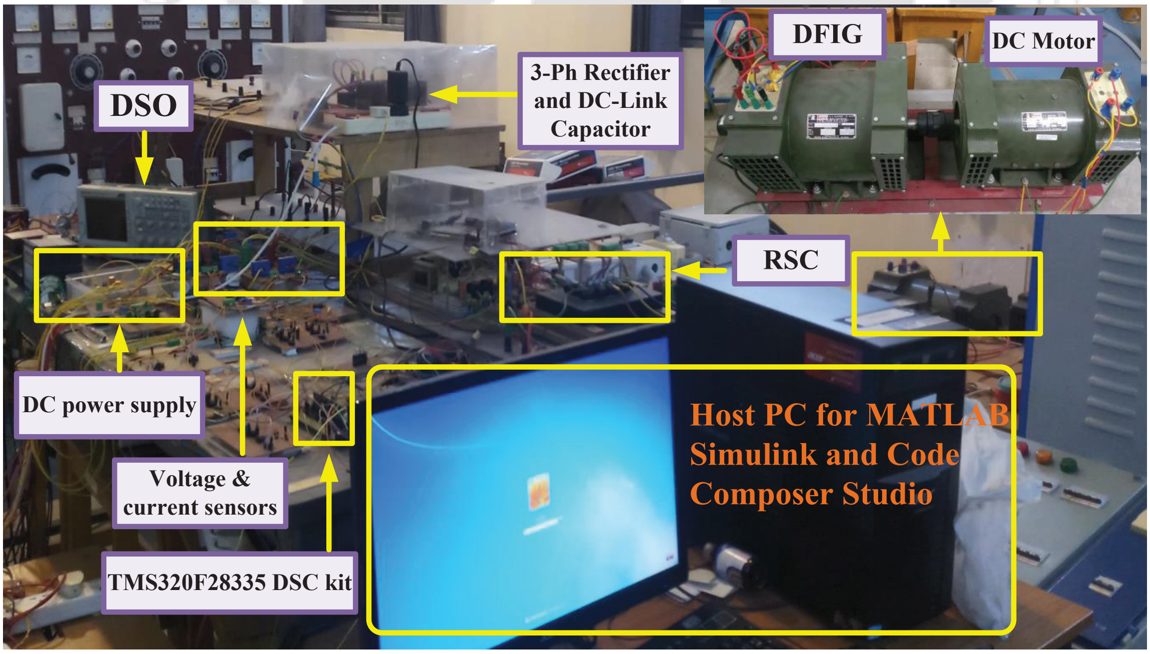

Figure A.2: Pictorial representation of the experimental setup of the GSC

B

Dynamic model of the DFIG

B.1 Reference frame transformations:

Clark and Park transformation are used to transform the three-phase machine variables to two phase stationary DC variables.

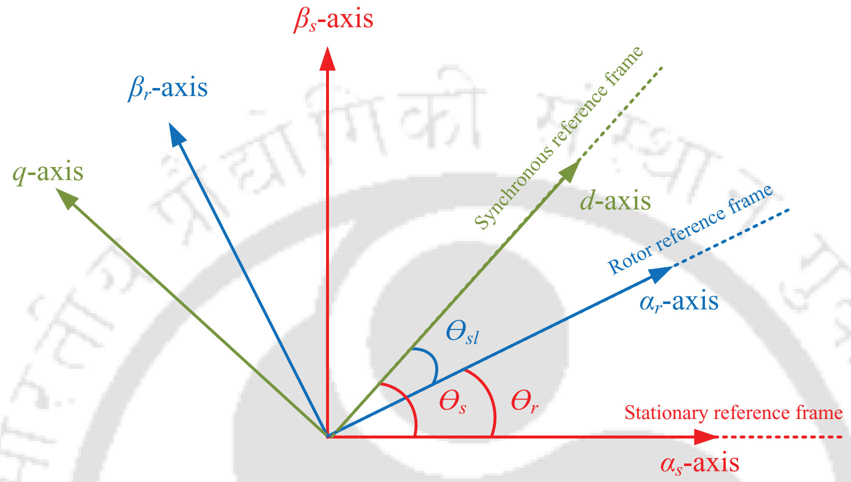

Figure B.1: Different reference frames and relative positions

B.1.1 Three-phase (abc) to two-phase ($\alpha\beta$) transformation (Clark)

$$\begin{bmatrix} x_{\alpha s,r} \\ x_{\beta s,r} \end{bmatrix} = \left[K_{\alpha\beta s,r}\right] \begin{bmatrix} x_{as,r} \\ x_{bs,r} \\ x_{cs,r} \end{bmatrix} \tag{B.1}$$

where $K_{\alpha\beta s,r}$ is represented as

$$\left[K_{\alpha\beta s,r}\right] = \frac{2}{3} \begin{bmatrix} 1 & -\frac{1}{2} & -\frac{1}{2} \\ 0 & \frac{\sqrt{3}}{2} & -\frac{\sqrt{3}}{2} \end{bmatrix}$$

B.1.2 Two-phase $\alpha\beta$ to dq transformation (Park)

$$\begin{bmatrix} x_{ds} \\ x_{qs} \end{bmatrix} = \left[K_{dqs}\right] \begin{bmatrix} x_{\alpha s} \\ x_{\beta s} \end{bmatrix}, \quad \begin{bmatrix} x_{dr} \\ x_{sr} \end{bmatrix} = \left[K_{dqr}\right] \begin{bmatrix} x_{\alpha r} \\ x_{\beta r} \end{bmatrix} \tag{B.2}$$

where K_{dqs}, K_{dqr} is represented as

$$\left[K_{dq_s}\right] = \begin{bmatrix} \cos(\theta_s) & \sin(\theta_s) \\ -\sin(\theta_s) & \cos(\theta_s) \end{bmatrix}, \quad \left[K_{dq_r}\right] = \begin{bmatrix} \cos(\theta_{sl}) & \sin(\theta_{sl}) \\ -\sin(\theta_{sl}) & \cos(\theta_{sl}) \end{bmatrix}$$

where ($\theta_{sl} = \theta_s - \theta_r$) and subscript s and r represents the stator and rotor quantities (Figure B.1).

B.2 Dynamic model of the DFIG in stationary reference frame ($\alpha\beta$)

The voltage equation of the DFIG in stationary frame of reference is represented considering the $\alpha\beta$ model (Figure B.2) as

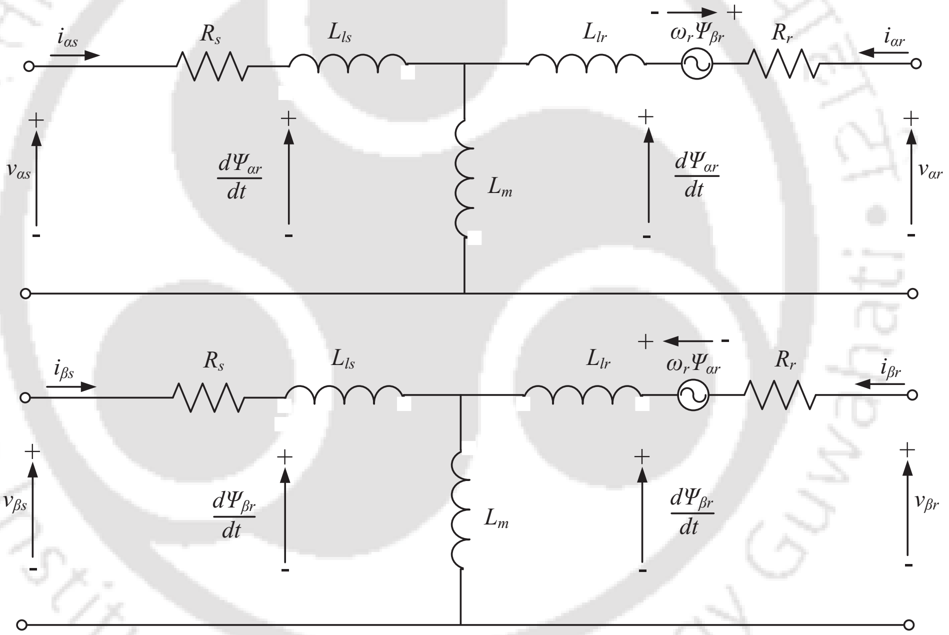

Figure B.2: $\alpha\beta$ model of the DFIG in stationary reference frame

$$\left.\begin{aligned} v_{\alpha s} &= R_s i_{\alpha s} + \frac{d\psi_{\alpha s}}{dt} && \text{(a)} \\ v_{\beta s} &= R_s i_{\beta s} + \frac{d\psi_{\beta s}}{dt} && \text{(b)} \\ v_{\alpha r} &= R_r i_{\alpha r} + \frac{d\psi_{\alpha r}}{dt} + \omega_r\psi_{\beta r} && \text{(c)} \\ v_{\beta r} &= R_s i_{\beta r} + \frac{d\psi_{\beta r}}{dt} - \omega_r\psi_{\alpha r} && \text{(d)} \end{aligned}\right\} \qquad \text{(B.3)}$$

where R_s and R_r are the stator and rotor resistances respectively, $\psi_{\alpha s}, \psi_{\beta s}$ and $\psi_{\alpha r}, \psi_{\beta r}$ are the stator and rotor fluxes respectively, ω_r is the rotor speed.

The expression for the stator and rotor flux can be written as

$$\left.\begin{aligned} \psi_{\alpha s} &= L_s i_{\alpha s} + L_m i_{\alpha r} && \text{(a)} \\ \psi_{\beta s} &= L_s i_{\beta s} + L_m i_{\beta r} && \text{(b)} \\ \psi_{\alpha r} &= L_m i_{\alpha s} + L_r i_{\alpha r} && \text{(c)} \\ \psi_{\beta r} &= L_m i_{\beta s} + L_r i_{\beta r} && \text{(d)} \end{aligned}\right\} \tag{B.4}$$

where L_s and L_r are the stator and rotor inductances, L_m is the mutual inductance, and the stator and rotor inductances can be written as

$$\begin{aligned} L_s &= L_{ls} + L_m \\ L_r &= L_{lr} + L_m \end{aligned} \tag{B.5}$$

where L_{ls} and L_{lr} are the self inductances of the stator and rotor respectively.

Further the rotor currents can be written in terms of stator currents and rotor fluxes from (B.4(c)) and (B.4(d)).

$$\left.\begin{aligned} i_{\alpha r} &= \frac{1}{L_r}\left(\psi_{\alpha r} - L_m i_{\alpha s}\right) && \text{(a)} \\ i_{\beta r} &= \frac{1}{L_r}\left(\psi_{\beta r} - L_m i_{\beta s}\right) && \text{(b)} \end{aligned}\right\} \tag{B.6}$$

From the dynamic model of the DFIG (B.3(c)) and (B.3(d)), the rotor flux dynamics can be represented as

$$\left.\begin{aligned} \frac{d}{dt}\psi_{\alpha r} &= -R_r i_{\alpha r} - \omega_r \psi_{\beta r} + v_{\alpha r} && \text{(a)} \\ \frac{d}{dt}\psi_{\beta r} &= -R_r i_{\beta r} + \omega_r \psi_{\alpha r} + v_{\alpha r} && \text{(b)} \end{aligned}\right\} \tag{B.7}$$

Replacing $i_{\alpha r}$ and $i_{\beta r}$ from (B.6) into (B.7), the rotor flux dynamics can be further expressed as

$$\left.\begin{aligned} \frac{d}{dt}\psi_{\alpha r} &= \frac{R_r L_m}{L_r} i_{\alpha s} - \frac{R_r}{L_r}\psi_{\alpha r} - \omega_r \psi_{\beta r} + v_{\alpha r} && \text{(a)} \\ \frac{d}{dt}\psi_{\beta r} &= \frac{R_r L_m}{L_r} i_{\beta s} + \omega_r \psi_{\alpha r} - \frac{R_r}{L_r}\psi_{\beta r} + v_{\beta r} && \text{(b)} \end{aligned}\right\} \tag{B.8}$$

Replacing (B.4) in the voltage equation (B.3) and then rearranging (B.3), the current dynamics can be expressed as

$$\left.\begin{aligned}
\frac{d}{dt}i_{\alpha s} &= -\frac{R_s}{\sigma L_s}i_{\alpha s} + \frac{\omega_r L_m^2}{\sigma L_s L_r}i_{\beta s} + \frac{R_r L_m}{\sigma L_s L_r}i_{\alpha r} + \frac{\omega_r L_m}{\sigma L_s}i_{\beta r} + \frac{1}{\sigma L_s}v_{\alpha s} - \frac{L_m}{\sigma L_s L_r}v_{\alpha r} && \text{(a)}\\
\frac{d}{dt}i_{\beta s} &= -\frac{\omega_r L_m^2}{\sigma L_s L_r}i_{\alpha s} - \frac{R_s}{\sigma L_s}i_{\beta s} - \frac{\omega_r L_m}{\sigma L_s}i_{\alpha r} + \frac{R_r L_m}{\sigma L_s L_r}i_{\beta r} + \frac{1}{\sigma L_s}v_{\beta s} - \frac{L_m}{\sigma L_s L_r}v_{\beta r} && \text{(b)}\\
\frac{d}{dt}i_{\alpha r} &= \frac{R_s L_m}{\sigma L_s L_r}i_{\alpha s} - \frac{\omega_r L_m}{\sigma L_r}i_{\beta s} - \frac{R_r}{\sigma L_r}i_{\alpha r} - \frac{\omega_r}{\sigma}i_{\beta r} - \frac{L_m}{\sigma L_s L_r}v_{\alpha s} + \frac{1}{\sigma L_r}v_{\alpha r} && \text{(c)}\\
\frac{d}{dt}i_{\beta r} &= \frac{\omega_r L_m}{\sigma L_r}i_{\alpha s} + \frac{R_s L_m}{\sigma L_s L_r}i_{\beta s} - \frac{\omega_r}{\sigma}i_{\alpha r} - \frac{R_r}{\sigma L_r}i_{\beta r} - \frac{L_m}{\sigma L_s L_r}v_{\beta s} + \frac{1}{\sigma L_r}v_{\beta r} && \text{(d)}
\end{aligned}\right\} \qquad \text{(B.9)}$$

where $\sigma = 1 - \frac{L_m^2}{L_s L_r}$ is the leakage factor.

Replacing (B.6(a)) and (B.6(b)) into (B.9(a)) and (B.9(b)) respectively, the stator current dynamics can be further expressed as

$$\left.\begin{aligned}
\frac{d}{dt}i_{\alpha s} &= -\left(\frac{R_s}{\sigma L_s} + \frac{R_r L_m^2}{\sigma L_s L_r^2}\right)i_{\alpha s} + \frac{R_r L_m}{\sigma L_s L_r^2}\psi_{\alpha r} + \frac{\omega_r L_m}{\sigma L_s L_r}\psi_{\beta r} + \frac{1}{\sigma L_s}v_{\alpha s} - \frac{L_m}{\sigma L_s L_r}v_{\alpha r} && \text{(a)}\\
\frac{d}{dt}i_{\beta s} &= -\left(\frac{R_s}{\sigma L_s} + \frac{R_r L_m^2}{\sigma L_s L_r^2}\right)i_{\beta s} - \frac{\omega_r L_m}{\sigma L_s L_r}\psi_{\alpha r} + \frac{R_r L_m}{\sigma L_s L_r^2}\psi_{\beta r} + \frac{1}{\sigma L_s}v_{\beta s} - \frac{L_m}{\sigma L_s L_r}v_{\beta r} && \text{(b)}
\end{aligned}\right\} \qquad \text{(B.10)}$$

where $\frac{\omega_r L_m}{\sigma L_s L_r}L_m i_{\beta s} + \frac{\omega_r L_m}{\sigma L_s L_r}L_r i_{\beta r} = \frac{\omega_r L_m}{\sigma L_s L_r}\psi_{\beta r}$ and $-\frac{\omega_r L_m}{\sigma L_s L_r}L_m i_{\alpha s} - \frac{\omega_r L_m}{\sigma L_s L_r}L_r i_{\alpha r} = -\frac{\omega_r L_m}{\sigma L_s L_r}\psi_{\alpha r}$.

Therefore, the dynamic model of the DFIG can be expressed as given below (B.11) in stationary $\alpha\beta$-frame of reference considering stator currents (B.10) and rotor fluxes (B.8) as the states.

$$\left.\begin{aligned}
\frac{d}{dt}i_{\alpha s} &= -\left(\frac{R_s}{\sigma L_s} + \frac{R_r L_m^2}{\sigma L_s L_r^2}\right)i_{\alpha s} + \frac{R_r L_m}{\sigma L_s L_r^2}\psi_{\alpha r} + \frac{\omega_r L_m}{\sigma L_s L_r}\psi_{\beta r} + \frac{1}{\sigma L_s}v_{\alpha s} - \frac{L_m}{\sigma L_s L_r}v_{\alpha r} && \text{(a)}\\
\frac{d}{dt}i_{\beta s} &= -\left(\frac{R_s}{\sigma L_s} + \frac{R_r L_m^2}{\sigma L_s L_r^2}\right)i_{\beta s} - \frac{\omega_r L_m}{\sigma L_s L_r}\psi_{\alpha r} + \frac{R_r L_m}{\sigma L_s L_r^2}\psi_{\beta r} + \frac{1}{\sigma L_s}v_{\beta s} - \frac{L_m}{\sigma L_s L_r}v_{\beta r} && \text{(b)}\\
\frac{d}{dt}\psi_{\alpha r} &= \frac{R_r L_m}{L_r}i_{\alpha s} - \frac{R_r}{L_r}\psi_{\alpha r} - \omega_r\psi_{\beta r} + v_{\alpha r} && \text{(c)}\\
\frac{d}{dt}\psi_{\beta r} &= \frac{R_r L_m}{L_r}i_{\beta s} + \omega_r\psi_{\alpha r} - \frac{R_r}{L_r}\psi_{\beta r} + v_{\beta r} && \text{(d)}
\end{aligned}\right\} \qquad \text{(B.11)}$$

Further, the dynamics (B.11) is represented as

$$\left.\begin{aligned}
\frac{di_{\alpha s}}{dt} &= ai_{\alpha s} + c\psi_{\alpha r} + d\omega_r\psi_{\beta r} + bv_{\alpha s} - hv_{\alpha r} && \text{(a)}\\
\frac{di_{\beta s}}{dt} &= ai_{\beta s} - d\omega_r\psi_{\alpha r} + c\psi_{\beta r} + bv_{\beta s} - hv_{\beta r} && \text{(b)}\\
\frac{d\psi_{\alpha r}}{dt} &= gi_{\alpha s} - f\psi_{\alpha r} - \omega_r\psi_{\beta r} + v_{\alpha r} && \text{(c)}\\
\frac{d\psi_{\beta r}}{dt} &= gi_{\beta s} + \omega_r\psi_{\alpha r} - f\psi_{\beta r} + v_{\beta r} && \text{(d)}
\end{aligned}\right\} \tag{B.12}$$

where, $a = -\left(\frac{R_s}{\sigma L_s} + \frac{L_m^2}{\sigma L_s \tau_r L_r}\right)$, $b = \frac{1}{\sigma L_s}$, $c = \frac{1}{e\tau_r}$, $d = \frac{1}{e}$, $e = \frac{\sigma L_s L_r}{L_m}$, $f = \frac{1}{\tau_r}$, $g = \frac{L_m}{\tau_r}$, $h = \frac{L_m}{\sigma L_s L_r}$, $\tau_r = \frac{L_r}{R_r}$.

B.3 Dynamic model of the DFIG in synchronous reference frame (dq)

The dynamic model of the DFIG in syncronous reference frame is represented as

$$\left.\begin{aligned}
v_{ds} &= R_s i_{ds} + \frac{d\psi_{ds}}{dt} - \omega_s\psi_{qs} && \text{(a)}\\
v_{qs} &= R_s i_{qs} + \frac{d\psi_{qs}}{dt} + \omega_s\psi_{ds} && \text{(b)}\\
v_{dr} &= R_r i_{dr} + \frac{d\psi_{dr}}{dt} + \omega_r\psi_{\beta r} - \omega_{sl}\psi_{qr} && \text{(c)}\\
v_{qr} &= R_s i_{qr} + \frac{d\psi_{qr}}{dt} - \omega_r\psi_{\alpha r} + \omega_s\psi_{dr} && \text{(d)}
\end{aligned}\right\} \tag{B.13}$$

where ($\omega_{sl} = \omega_s - \omega_r$) is the slip frequency and ω_s is the stator frequency and the stator and rotor flux expression in dq domain are represented as

$$\left.\begin{aligned}
\psi_{ds} &= L_s i_{ds} + L_m i_{dr} && \text{(a)}\\
\psi_{qs} &= L_s i_{qs} + L_m i_{qr} && \text{(b)}\\
\psi_{dr} &= L_s i_{ds} + L_m i_{dr} && \text{(c)}\\
\psi_{qr} &= L_s i_{qs} + L_m i_{qr} && \text{(d)}
\end{aligned}\right\} \tag{B.14}$$

Bibliography

[1] eia, "Renewable energy explained," Available at https://www.eia.gov/energyexplained/renewable-sources/ (2020/08/15).

[2] iea, "Renewables 2020: Analysis and forecast to 2025," Available at https://www.iea.org/reports/renewables-2020/solar-pv#abstract (2021/01/15).

[3] J. Lee, F. Zhao, A. Dutton, B. Backwell, R. Fiestas, L. Qiao, N. Balachandran, S. Lim, W. Liang, E. Clarke *et al.*, "Global wind report 2019," *Brussels: Global Wind Energy Council (GWEC)*, 2020.

[4] MNRE, "Annual report 2019-20," Available at https://mnre.gov.in/img/documents/uploads/file_f-1597797108502.pdf (2020/04/12).

[5] M. Soliman, "Model predictive control of dfig-based wind power generation systems," Ph.D. dissertation, University of Calgary, 2013.

[6] G. Abad, J. Lopez, M. Rodriguez, L. Marroyo, and G. Iwanski, *Doubly fed induction machine: modeling and control for wind energy generation*. John Wiley & Sons, 2011, vol. 85.

[7] R. Pena, J. Clare, and G. Asher, "Doubly fed induction generator using back-to-back pwm converters and its application to variable-speed wind-energy generation," *IEE Proceedings-Electric power applications*, vol. 143, no. 3, pp. 231–241, 1996.

[8] V. Kaura and V. Blasko, "Operation of a phase locked loop system under distorted utility conditions," *IEEE Transactions on Industry applications*, vol. 33, no. 1, pp. 58–63, 1997.

[9] M. Karimi-Ghartemani, S. A. Khajehoddin, P. K. Jain, and A. Bakhshai, "Derivation and design of in-loop filters in phase-locked loop systems," *IEEE Transactions on Instrumentation and Measurement*, vol. 61, no. 4, pp. 930–940, 2011.

[10] S. Golestan, J. M. Guerrero, and J. C. Vasquez, "Three-phase plls: A review of recent advances," *IEEE Transactions on Power Electronics*, vol. 32, no. 3, pp. 1894–1907, 2016.

[11] A. Chatterjee, K. B. Mohanty, K. Thakre, and V. S. Kommukuri, "Grid voltage sensorless control of single phase grid tied inverter for renewable energy systems applications," *Electric Power Components and Systems*, vol. 46, no. 16-17, pp. 1795–1807, 2018.

[12] L. Hadjidemetriou, E. Kyriakides, and F. Blaabjerg, "A new hybrid pll for interconnecting renewable energy systems to the grid," *IEEE Transactions on industry applications*, vol. 49, no. 6, pp. 2709–2719, 2013.

[13] P. L. Chapman and S. D. Sudhoff, "A multiple reference frame synchronous estimator/regulator," *IEEE Transactions on Energy Conversion*, vol. 15, no. 2, pp. 197–202, 2000.

[14] F. González-Espín, E. Figueres, and G. Garcerá, “An adaptive synchronous-reference-frame phase-locked loop for power quality improvement in a polluted utility grid,” *IEEE Transactions on Industrial Electronics*, vol. 59, no. 6, pp. 2718–2731, 2011.

[15] Y. Han, L. Xu, M. M. Khan, G. Yao, L.-D. Zhou, and C. Chen, “A novel synchronization scheme for grid-connected converters by using adaptive linear optimal filter based pll (alof–pll),” *Simulation Modelling Practice and Theory*, vol. 17, no. 7, pp. 1299–1345, 2009.

[16] F. D. Freijedo, A. G. Yepes, Ó. López, P. Fernandez-Comesana, and J. Doval-Gandoy, “An optimized implementation of phase locked loops for grid applications,” *IEEE Transactions on Instrumentation and Measurement*, vol. 60, no. 9, pp. 3110–3119, 2011.

[17] P. Rodríguez, J. Pou, J. Bergas, J. I. Candela, R. P. Burgos, and D. Boroyevich, “Decoupled double synchronous reference frame pll for power converters control,” *IEEE Transactions on Power Electronics*, vol. 22, no. 2, pp. 584–592, 2007.

[18] S. Eren and A. Bakhshai, “Modifying the three-phase synchronous reference frame phase-locked loop to remove unbalance and harmonic errors,” 2008.

[19] S. Golestan, M. Monfared, and F. D. Freijedo, “Design-oriented study of advanced synchronous reference frame phase-locked loops,” *IEEE Transactions on Power Electronics*, vol. 28, no. 2, pp. 765–778, 2012.

[20] P. Xiao, K. A. Corzine, and G. K. Venayagamoorthy, “Multiple reference frame-based control of three-phase pwm boost rectifiers under unbalanced and distorted input conditions,” *IEEE transactions on power electronics*, vol. 23, no. 4, pp. 2006–2017, 2008.

[21] C. A. Busada, S. G. Jorge, A. E. Leon, and J. A. Solsona, “Current controller based on reduced order generalized integrators for distributed generation systems,” *IEEE Transactions on Industrial Electronics*, vol. 59, no. 7, pp. 2898–2909, 2011.

[22] W. Li, X. Ruan, C. Bao, D. Pan, and X. Wang, “Grid synchronization systems of three-phase grid-connected power converters: A complex-vector-filter perspective,” *IEEE Transactions on Industrial Electronics*, vol. 61, no. 4, pp. 1855–1870, 2013.

[23] X. Guo, W. Wu, and Z. Chen, “Multiple-complex coefficient-filter-based phase-locked loop and synchronization technique for three-phase grid-interfaced converters in distributed utility networks,” *IEEE Transactions on Industrial Electronics*, vol. 58, no. 4, pp. 1194–1204, 2010.

[24] Y. F. Wang and Y. W. Li, “Grid synchronization pll based on cascaded delayed signal cancellation,” *IEEE Transactions on Power Electronics*, vol. 26, no. 7, pp. 1987–1997, 2010.

[25] S. Golestan, M. Ramezani, J. M. Guerrero, and M. Monfared, “dq-frame cascaded delayed signal cancellation-based pll: analysis, design, and comparison with moving average filter-based pll,” *IEEE Transactions on Power Electronics*, vol. 30, no. 3, pp. 1618–1632, 2014.

[26] M. Ciobotaru, R. Teodorescu, and F. Blaabjerg, “A new single-phase pll structure based on second order generalized integrator,” in *2006 37th IEEE Power Electronics Specialists Conference*. IEEE, 2006, pp. 1–6.

[27] M. Ciobotaru, R. Teodorescu, and V. G. Agelidis, “Offset rejection for pll based synchronization in grid-connected converters,” in *2008 Twenty-Third Annual IEEE Applied Power Electronics Conference and Exposition*. IEEE, 2008, pp. 1611–1617.

[28] M. K. Ghartemani, S. A. Khajehoddin, P. K. Jain, and A. Bakhshai, “Problems of startup and phase jumps in pll systems,” *IEEE Transactions on Power Electronics*, vol. 27, no. 4, pp. 1830–1838, 2011.

[29] S. Golestan, J. M. Guerrero, and J. C. Vasquez, “Steady-state linear kalman filter-based plls for power applications: A second look,” *IEEE Transactions on Industrial Electronics*, vol. 65, no. 12, pp. 9795–9800, 2018.

[30] A. Bellini, S. Bifaretti, and F. Giannini, “A robust synchronization method for centralized microgrids,” in *2013 IEEE Energy Conversion Congress and Exposition*. IEEE, 2013, pp. 4587–4594.

[31] S. Bifaretti, P. Zanchetta, and E. Lavopa, “Comparison of two three-phase pll systems for more electric aircraft converters,” *IEEE Transactions on Power Electronics*, vol. 29, no. 12, pp. 6810–6820, 2014.

[32] R. Pena, J. Clare, and G. Asher, “A doubly fed induction generator using back-to-back pwm converters supplying an isolated load from a variable speed wind turbine,” *IEE Proceedings-Electric Power Applications*, vol. 143, no. 5, pp. 380–387, 1996.

[33] R. Wu, S. B. Dewan, and G. R. Slemon, “A pwm ac-to-dc converter with fixed switching frequency,” *IEEE Trans. Ind. App.*, vol. 26, no. 5, pp. 880–885, 1990.

[34] C.-T. Pan and T.-C. Chen, “Modelling and analysis of a three phase pwm ac-dc convertor without current sensor,” in *Proc. Inst. Elect. Eng. Elect. Power Appl.*, vol. 140, no. 3. IET, 1993, pp. 201–208.

[35] L. Malesani, P. Mattavelli, and S. Buso, “Robust dead-beat current control for pwm rectifiers and active filters,” in *Conference Record of 1998 IEEE Ind. Appl. Con. Thirty-Third IAS Annual Meeting (Cat. No. 98CH36242)*, vol. 2. IEEE, 1998, pp. 1377–1384.

[36] S. Vazquez, J. I. Leon, L. G. Franquelo, J. Rodriguez, H. A. Young, A. Marquez, and P. Zanchetta, “Model predictive control: A review of its applications in power electronics,” *IEEE Ind. Electron. Magazine*, vol. 8, no. 1, pp. 16–31, 2014.

[37] Z. Zhang, H. Fang, F. Gao, J. Rodríguez, and R. Kennel, “Multiple-vector model predictive power control for grid-tied wind turbine system with enhanced steady-state control performance,” *IEEE Trans. Ind. Electron.*, vol. 64, no. 8, pp. 6287–6298, 2017.

[38] N. Panten, N. Hoffmann, and F. W. Fuchs, “Finite control set model predictive current control for grid-connected voltage-source converters with lcl filters: A study based on different state feedbacks,” *IEEE Trans. Power Electron.*, vol. 31, no. 7, pp. 5189–5200, 2015.

[39] J. Linares-Flores, A. H. Méndez, C. García-Rodríguez, and H. Sira-Ramírez, “Robust nonlinear adaptive control of a boost converter via algebraic parameter identification,” *IEEE Trans. Ind. Electron.*, vol. 61, no. 8, pp. 4105–4114, 2013.

[40] M. Abdallah, O. Arafa, A. Shaltot, and G. A. Abdel-Aziz, “Mrac-based vector oriented control of a wind turbine-driven dfig,” in *2016 Eighteenth International Middle East Power Systems Conference (MEPCON)*. IEEE, 2016, pp. 597–603.

[41] L. Harnefors, A. G. Yepes, A. Vidal, and J. Doval-Gandoy, “Passivity-based controller design of grid-connected vscs for prevention of electrical resonance instability,” *IEEE Trans. Ind. Electron.*, vol. 62, no. 2, pp. 702–710, 2014.

[42] T.-S. Lee, “Input-output linearization and zero-dynamics control of three-phase ac/dc voltage-source converters,” *IEEE Trans. Power Electron.*, vol. 18, no. 1, pp. 11–22, 2003.

[43] A. Bouafia, F. Krim, and J.-P. Gaubert, “Fuzzy-logic-based switching state selection for direct power control of three-phase pwm rectifier,” *IEEE Trans. Ind. Electron.*, vol. 56, no. 6, pp. 1984–1992, 2009.

[44] S. Muyeen and A. Al-Durra, “Modeling and control strategies of fuzzy logic controlled inverter system for grid interconnected variable speed wind generator,” *IEEE Syst. J.*, vol. 7, no. 4, pp. 817–824, 2013.

[45] Y. Sun, S. Li, B. Lin, X. Fu, M. Ramezani, and I. Jaithwa, “Artificial neural network for control and grid integration of residential solar photovoltaic systems,” *IEEE Trans. Sustain. Energy*, vol. 8, no. 4, pp. 1484–1495, 2017.

[46] S. Li, M. Fairbank, C. Johnson, D. C. Wunsch, E. Alonso, and J. L. Proao, “Artificial neural networks for control of a grid-connected rectifier/inverter under disturbance, dynamic and power converter switching conditions,” *IEEE Trans. Neural Netw. Learn. Syst.*, vol. 25, no. 4, pp. 738–750, 2013.

[47] D. Vilathgamuwa, S. Wall, and R. Jackson, “Variable structure control of voltage sourced reversible rectifiers,” *Proc. Inst. Elect. Eng. Elect. Power Appl*, vol. 143, no. 1, pp. 18–24, 1996.

[48] J. F. Silva, “Sliding-mode control of boost-type unity-power-factor pwm rectifiers,” *IEEE Trans. Ind. Electron.*, vol. 46, no. 3, pp. 594–603, 1999.

[49] S.-C. Tan, Y.-M. Lai, K. T. Chi, L. Martinez-Salamero, and C.-K. Wu, “A fast-response sliding-mode controller for boost-type converters with a wide range of operating conditions,” *IEEE Trans. Ind. Electron.*, vol. 54, no. 6, pp. 3276–3286, 2007.

[50] Y. Shtessel, S. Baev, and H. Biglari, “Unity power factor control in three-phase ac/dc boost converter using sliding modes,” *IEEE Trans. Ind. Electron.*, vol. 55, no. 11, pp. 3874–3882, 2008.

[51] J. Liu, Y. Yin, W. Luo, S. Vazquez, L. G. Franquelo, and L. Wu, “Sliding mode control of a three-phase ac/dc voltage source converter under unknown load conditions: Industry applications,” *IEEE Trans. Syst., Man, Cybern., Syst.*, vol. 48, no. 10, pp. 1771–1780, 2017.

[52] J. Liu, S. Vazquez, L. Wu, A. Marquez, H. Gao, and L. G. Franquelo, “Extended state observer-based sliding-mode control for three-phase power converters,” *IEEE Trans. Ind. Electron.*, vol. 64, no. 1, pp. 22–31, 2016.

[53] X. Zhu, S. Liu, and Y. Wang, “Second-order sliding-mode control of dfig-based wind turbines,” 2014.

[54] J. Song, Y. Niu, and Y. Zou, “Finite-time sliding mode control synthesis under explicit output constraint,” *Automatica*, vol. 65, pp. 111–114, 2016.

[55] X.-G. Yan, S. K. Spurgeon, and C. Edwards, “Decentralized output feedback sliding mode control of nonlinear large-scale systems with uncertainties,” *Journal of optimization theory and applications*, vol. 119, no. 3, pp. 597–614, 2003.

[56] A. Zakipour, S. S. Kojori, and M. T. Bina, “Closed-loop control of the grid-connected z-source inverter using hyper-plane mimo sliding mode,” *IET Power Electron.*, vol. 10, no. 15, pp. 2229–2241, 2017.

[57] S. Rao, M. Buss, and V. Utkin, “Simultaneous state and parameter estimation in induction motors using first-and second-order sliding modes,” *IEEE Transactions on Industrial Electronics*, vol. 56, no. 9, pp. 3369–3376, 2009.

[58] R. Cardenas, R. Peña, S. Alepuz, and G. Asher, “Overview of control systems for the operation of dfigs in wind energy applications,” *IEEE Trans. Ind. Electron*, vol. 60, no. 7, pp. 2776–2798, 2013.

[59] D. Reigosa, F. Briz, C. Blanco, A. Di Gioia, P. García, and J. M. Guerrero, "Sensorless control of doubly-fed induction generators based on rotor high frequency signal injection," in *2012 IEEE Energy Conversion Congress and Exposition (ECCE)*. IEEE, 2012, pp. 2268–2275.

[60] D. D. Reigosa, F. Briz, C. Blanco, and J. M. Guerrero, "Sensorless control of doubly fed induction generators based on stator high-frequency signal injection," *IEEE Trans. Ind. Appl.*, vol. 50, no. 5, pp. 3382–3391, 2014.

[61] K. Tshiloz, D. Vilchis-Rodriguez, S. Djukanović, N. Sarma, and S. Djurović, "Sensorless speed estimation in wound rotor induction machines by spectral search of the stator phase power signal," *IET Electr. Power App.*, vol. 10, no. 6, pp. 581–592, 2016.

[62] L. Morel, H. Godfroid, A. Mirzaian, and J. Kauffmann, "Double-fed induction machine: converter optimisation and field oriented control without position sensor," *IEE P-Electr. Power App.*, vol. 145, no. 4, pp. 360–368, 1998.

[63] R. Cardenas, R. Pena, J. Proboste, G. Asher, and J. Clare, "Mras observer for sensorless control of standalone doubly fed induction generators," *IEEE Trans. Energy Convers.*, vol. 20, no. 4, pp. 710–718, 2005.

[64] R. Cárdenas, R. Peña, J. Clare, G. Asher, and J. Proboste, "Mras observers for sensorless control of doubly-fed induction generators," *IEEE Trans. Power Electron.*, vol. 23, no. 3, pp. 1075–1084, 2008.

[65] R. Pena, R. Cardenas, J. Proboste, G. Asher, and J. Clare, "Sensorless control of doubly-fed induction generators using a rotor-current-based mras observer," *IEEE Trans. Ind. Electron.*, vol. 55, no. 1, pp. 330–339, 2008.

[66] M. K. Malakar, P. Tripathy, and S. Krishnaswamy, "State estimation of dfig using an extended kalman filter with an augmented state model," in *2014 Eighteenth National Power Systems Conf. (NPSC)*. IEEE, 2014, pp. 1–6.

[67] M. Abdelrahem, C. Hackl, and R. Kennel, "Sensorless control of doubly-fed induction generators in variable-speed wind turbine systems," in *2015 International Conference on Clean Electrical Power (ICCEP)*. IEEE, 2015, pp. 406–413.

[68] C. Wei, Z. Zhang, J. Zeng, and W. Qiao, "Stator current-based sliding mode observer for sensorless vector contorl of doubly-fed induction geneartors," in *2015 IEEE Energy Conversion Congress and Exposition (ECCE)*. IEEE, 2015, pp. 4165–4171.

[69] M. F. Iacchetti, "Adaptive tuning of the stator inductance in a rotor-current-based mras observer for sensorless doubly fed induction-machine drives," *IEEE Trans. Ind. Electron.*, vol. 58, no. 10, pp. 4683–4692, 2011.

[70] R. Bhattarai, N. Gurung, S. Ghosh, and S. Kamalasadan, "Parametrically robust dynamic speed estimation based control for doubly fed induction generator," *IEEE Trans. Ind. Appl.*, vol. 54, no. 6, pp. 6529–6542, 2018.

[71] C. Wei, W. Qiao, and Y. Zhao, "Sliding-mode observer-based sensorless direct power control of dfigs for wind power applications," in *2015 IEEE Power & Energy Society General Meeting*. IEEE, 2015, pp. 1–5.

[72] M. Benbouzid, B. Beltran, H. Mangel, and A. Mamoune, "A high-order sliding mode observer for sensorless control of dfig-based wind turbines," in *IECON 2012-38th Annual Conf. on IEEE Industrial Electronics Society*. IEEE, 2012, pp. 4288–4292.

[73] M. W. K. Mbukani and N. Gule, “Pll-based sliding mode observer estimators for sensorless control of rotor-tied dfig systems,” *IEEE Trans. Ind. Appl*, vol. 55, no. 6, pp. 5960–5970, 2019.

[74] ——, “Comparison of high-order and second-order sliding mode observer based estimators for speed sensorless control of rotor-tied dfig systems,” *IET Power Electron.*, vol. 12, no. 12, pp. 3231–3241, 2019.

[75] S. Arnalte, J. Burgos, and J. Rodriguez-Amenedo, “Direct torque control of a doubly-fed induction generator for variable speed wind turbines,” *Electric power components and systems*, vol. 30, no. 2, pp. 199–216, 2002.

[76] B. Pimple, V. Vekhande, and B. Fernandes, “A new direct torque control of doubly-fed induction generator under unbalanced grid voltage,” in *2011 Twenty-Sixth Annual IEEE Applied Power Electronics Conference and Exposition (APEC)*. IEEE, 2011, pp. 1576–1581.

[77] D. Zhi and L. Xu, “Direct power control of dfig with constant switching frequency and improved transient performance,” *IEEE Transactions on Energy Conversion*, vol. 22, no. 1, pp. 110–118, 2007.

[78] Y. Zhang, J. Hu, and J. Zhu, “Three-vectors-based predictive direct power control of the doubly fed induction generator for wind energy applications,” *IEEE transactions on power electronics*, vol. 29, no. 7, pp. 3485–3500, 2013.

[79] B. Singh and N. S. Naidu, “Direct power control of single vsc-based dfig without rotor position sensor,” *IEEE Transactions on Industry Applications*, vol. 50, no. 6, pp. 4152–4163, 2014.

[80] R. Datta and V. Ranganathan, “Decoupled control of active and reactive power for a grid-connected doubly-fed wound rotor induction machine without position sensors,” in *Conference Record of the 1999 IEEE Industry Applications Conference. Thirty-Forth IAS Annual Meeting (Cat. No. 99CH36370)*, vol. 4. IEEE, 1999, pp. 2623–2630.

[81] A. B. Ataji, Y. Miura, T. Ise, and H. Tanaka, “Machine parameter independent control of a grid-connected variable speed doubly-fed induction generator for gas engine generation systems,” in *2013 IEEE ECCE Asia Downunder*. IEEE, 2013, pp. 1348–1354.

[82] F. Furfari and J. Brittain, “Charles legeyt fortescue and the method of symmetrical components,” *IEEE Industry Applications Magazine*, vol. 8, no. 3, pp. 7–9, 2002.

[83] A. V. Oppenheim and R. W. Schafer, “Digital signal processing(book),” *Research supported by the Massachusetts Institute of Technology, Bell Telephone Laboratories, and Guggenheim Foundation. Englewood Cliffs, N. J., Prentice-Hall, Inc., 1975. 598 p*, 1975.

[84] J. G. Ziegler, N. B. Nichols *et al.*, “Optimum settings for automatic controllers,” *trans. ASME*, vol. 64, no. 11, 1942.

[85] K. J. ström and T. Hägglund, “Revisiting the ziegler–nichols step response method for pid control,” *Journal of process control*, vol. 14, no. 6, pp. 635–650, 2004.

[86] A. A. Godbole, J. P. Kolhe, and S. E. Talole, “Performance analysis of generalized extended state observer in tackling sinusoidal disturbances,” *IEEE Trans. Control Syst. Technol.*, vol. 21, no. 6, pp. 2212–2223, 2012.

[87] Q. Zheng, Z. Chen, and Z. Gao, “A practical approach to disturbance decoupling control,” *Control Eng. Pract.*, vol. 17, no. 9, pp. 1016–1025, 2009.

[88] Z. Gao, "Active disturbance rejection control: a paradigm shift in feedback control system design," in *2006 American control conference*. IEEE, 2006, pp. 2399–2405.

[89] J.-J. E. Slotine, W. Li *et al.*, *Applied nonlinear control*. Prentice hall Englewood Cliffs, NJ, 1991, vol. 199, no. 1.

[90] R. Marino and P. Tomei, *Nonlinear control design: geometric, adaptive and robust*. Prentice Hall International (UK) Ltd., 1996.

[91] P. Vaclavek and P. Blaha, "Lyapunov-function-based flux and speed observer for ac induction motor sensorless control and parameters estimation," *IEEE Trans. Ind. Electron.*, vol. 53, no. 1, pp. 138–145, 2006.

[92] L. Fridman, A. Levant *et al.*, "Higher order sliding modes," *Sliding mode control in engineering*, vol. 11, pp. 53–102, 2002.

List of Publications

Journal Publications

1. Prosenjit Mondal,Praveen Tripathy, Ravindranath Adda, Ujjwal K Saha, “Development of an adaptive control strategy for the three-phase grid side converter with wide range of parametric and load uncertainties” *IET Power Electronics*, Vol. 13, No. 12, pp. 2399–2412, 2020.
2. Prosenjit Mondal, Praveen Tripathy, Ujjwal K Saha, Ravendranath Adda, ”A Simple Yet Robust Mechanism for the Improvement of Phase-locked-loop System and its Verification with Grid Side Converter Control” accepted for publication in *Journal of Electrical Engineering and Technology*.

Conference Publication

1. Prosenjit Mondal, Praveen Tripathy, Ujjwal K Saha. “Second Order Sliding Mode Observer Design for the Speed Estimation of DFIG” In 2020 Nineth IEEE International Conference on Power Electronics, Drives and Energy Systems (PEDES 2020), pp. 1-6. IEEE, 2020.

Under Review:

1. Prosenjit Mondal, Mridul K. Malakar, Praveen Tripathy, Srinivasan Krishnaswamy, Ujjwal K Saha, “Robust Observer Design for Sensorless Voltage and Frequency Control of a Doubly Fed Induction Generator in Standalone Mode”, Under Review (status: ”first revision submitted”) in IEEE Transaction on Energy Conversion.

Yet to be communicated:

1. Prosenjit Mondal, Praveen Tripathy, Ujjwal K Saha, ”Design and Implementation of Robust Current Control Technique for Constant Switching Frequency Driven Three-phase Grid Side Converter” possibly communicated to Electric Power System Research.